

学位論文

Study of the Generation Environment and Temporal
Development of Dust Storms in the Martian Atmosphere
Using a General Circulation Model

(大気大循環モデルを用いた
火星ダストストームの発生環境と時間発展に関する研究)

平成25年5月 博士（理学）申請

東京大学大学院理学系研究科
地球惑星科学専攻

門脇 正尚

Abstract

Airborne dust plays an important role in the Martian climate system. Since aerosol particles absorb and scatter incoming solar radiation, the spatial and temporal dust distribution strongly affects the atmospheric temperature. Dust is sourced from the ground, and is especially uplifted during dust storms. Depending on their size and duration, dust storms are divided into two types: regional and global (planet-encircling). In general circulation model (GCM) simulations, the Martian climate system critically depends on the dust cycle. In this study, we developed dust lifting schemes, and implemented them in our GCM. The total modules for dust cycle accounts for the lifting of dust particles beyond a specified threshold of the near-surface wind stress, the dust lifting by convective motion, transport of particles by local wind, and gravitational sedimentation. The scheme is interactive because the simulated dust distributions affect the radiative calculations, thus providing feedback to the atmospheric wind and temperature. The model accurately simulates the seasonal variation in dust opacity. In particular, the inter-seasonal variability of dust opacity in the northern hemisphere was reproduced reasonably. The dust opacity was consistent to the observation. The lifting location was also in agreement with the observation. During the southern summer, strong dust lifting is concentrated around sloped regions, and the near-surface wind reaches 25 m s^{-1} . Airborne dust heats the atmosphere, thereby generating atmospheric tides. These diurnal tides can be very strong (up to 11 m s^{-1}). Their activity accelerates the near-surface winds, providing positive feedback to the uplift of dust into the atmosphere. On the other hand, during the southern summer solstice ($L_S = 270^\circ$), simulated dust lifting is reduced in the northern hemisphere (at 50°N) by CO_2 ice caps forming on the ground. Dust lifting restarts after the recession of the polar cap. This result explains the temporal gap in the dust storm observed by Mars Global Surveyor Mars Orbiter Camera between Martian years MY24 and MY25. To clarify the temporal

development of global dust storms, additional dust lifting was imposed in the northern part of the Hellas basin. Strong dust lifting was simulated near the Hellas basin and the mountainous area centered at 30°N and 120°W. The effective winds for dust injections reached 35 m s⁻¹. Winds were strong where the trough of the surface pressure oscillation with a zonal wave number of 1 overlapped the slope. This result suggests that when the dust lifting strengthens in a certain region, plural dust lifting is immediately incited in other regions.

Contents

1	Introduction	1
1.1	Dust storms	1
1.1.1	Regional and global dust storms in the Martian atmosphere	1
1.1.2	Observational studies of Martian dust storms	2
1.1.3	Numerical studies of Martian dust cycle	4
1.2	Objectives of this study	5
2	Model description	10
2.1	Basic features	10
2.2	Martian physical processes	12
2.3	Dust lifting parameterization	12
2.3.1	Wind stress parameterization	13
2.3.2	Convective parameterization	15
2.3.3	Planetary boundary layer	16
2.4	Gravitational sedimentation	17
3	Sensitivity of dust lifting parametrization	20
3.1	Experimental design for sensitivity test	20
3.2	Comparison of model behavior for parameter dependence	21
3.2.1	Model sensitivity to wind stress scheme	21

3.2.2	Sensitivity for dust devil scheme	23
3.2.3	Response of dust opacity for couple of two lifting schemes	39
4	Regional dust storm	41
4.1	Dust opacity modeled by MGCM with both lifting schemes	41
4.1.1	Annual dust opacity and temperature structure	42
4.1.2	Seasonal dust lifting	45
4.2	Simulated dust lifting and near-surface wind	46
4.2.1	Effects of topography on dust lifting	46
4.2.2	Effective wind for dust lifting	49
4.3	Thermal tides in the Martian atmosphere	49
4.3.1	Amplitude of diurnal and semi-diurnal tides	49
4.3.2	Heating source of tides	52
4.4	Reduction of surface dust lifting between 480 Sol and 550 Sol	54
4.4.1	Gravitational sedimentation of dust	54
4.4.2	Ground covered with CO ₂ ice	54
5	Global dust storms	62
5.1	Experimental design for global dust storm	62
5.2	Simulated global dust storm	64
5.2.1	Temporal development of dust opacity	64
5.2.2	Dust lifting	66
5.2.3	Temperature and tides	66
5.3	Response of additional surface dust flux for global dust storm	70
5.4	Requirements for replicating global dust storms	72
6	Conclusions and future perspectives	74
	References	78

Chapter 1

Introduction

1.1 Dust storms

1.1.1 Regional and global dust storms in the Martian atmosphere

The Martian atmosphere contains numerous small, floating particles called dust, which absorb and scatter the incoming solar radiation. The time series of spatially distributed dust in the Martian atmosphere contribute to the dynamics and thermal structure of the planet. Previous observations have revealed that these dust distributions are variable seasonally. The dust opacity peaks in the southern spring and summer, when the planet is close to perihelion ($L_S = 250^\circ$). Since Mars follows a highly eccentric orbit, dust from the ground is lifted by the strong solar radiation [Smith *et al.*, 2000a]. These injections are described two climate phenomena. One is the dust storm, and the other is the convective motion called dust devil [Greeley and Iversen, 1985].

Dust storms, which frequently occur on Mars, are classified by their horizontal scale and active period. Regional dust storms persist for several weeks, and their horizontal scale extends to several thousands of kilometers [Cantor *et al.*, 2001]. In 1999, twelve regional dust storms were observed by Mars Obiter Camera between $L_S = 161.4^\circ$ and L_S

= 234.9°, and then eight regional dust storms occurred in the northern hemisphere. On the other hand, planet-encircling dust storms called as global dust storm have been observed. The great dust storm observed by Viking and Mars Global Surveyor in 1975, 1977 and 2001 [Szwast *et al.*, 2006]. The global dust storm event does not occur every Martian year. The past global dust storm began at the middle latitude in southern hemisphere early summer. The initial horizontal scale is less than 1000 km and the storm grows up global scale within a week. The temporal and spacial development of global dust storm is not understood enough. For instance, what does maintain the global dust storm. Dust particles in the atmosphere sediment to the ground by gravity. In order to keep high dust opacity, the much larger supplement of dust from the ground is necessary. A global dust storm was observed in MY25, then the dust opacity increased suddenly at the Hellase basin. A previous study suggested the importance of topography for the birth of larger dust storm [Smith *et al.*, 2000].

1.1.2 Observational studies of Martian dust storms

The behaviors of Martian dust storms and their effects on the atmospheric fields are known from observational studies. Dust is considered to be uplifted from the ground into the atmosphere by near-surface winds. Observations by Mars Global Surveyor Mars Orbiter Camera (MGS-MOC) have revealed that most of the dust storms occur in sloped regions [Cantor *et al.*, 2001] (see Figure 1.1). This result indicates that downward flows, such as katabatic winds, are effective for dust lifting. Dust is also raised by strong surface winds induced by thermal tides [Zurek *et al.*, 1979]. The amplitude and phase of tides in the Martian atmosphere (primarily in the southern hemisphere) have been determined by Mars Global Surveyor Thermal Emission Spectrometer (MGS-TES) observations [Banfield *et al.*, 2000]. The estimated amplitudes of diurnal tides exceed 8 K during regional dust storms (see Figure 1.2, top panel). In contrast, the amplitudes of semi-diurnal tides are approximately 2 K (see Figure 1.2, bottom panel). Regional dust storms are contin-

uously generated throughout the southern summer, and move eastward (see Figure 1.3). During the southern hemisphere summer in Martian years 24 and 25 (hereafter denoted as MY24 and MY25, respectively) [Wang *et al.*, 2005], MGS-MOC also revealed the temporal distributions of regional dust storms in the northern hemisphere (see Figure 1.4). Dust storms never appeared around the northern winter solstice ($L_S = 270^\circ$), for reasons that remain unclear. A global dust storm was observed in MY25. As this storm encircled the planet, a regional dust storm developed in the Terra Tyrrhena region (25°S , 270°W) located in the northern area of Hellas at $L_S = 185^\circ$. As this dust storm moved eastward, it expanded in latitude. Before it collapsed, another dust storm occurred at $L_S = 187^\circ \sim 189^\circ$ [Smith *et al.*, 2001] (see Figure 1.5). By such activity, several dust storms can interact and enhance each other, and regional dust storms can be swallowed by global dust storms. How the temporal development of global dust storms is maintained, however, remains to be clarified.

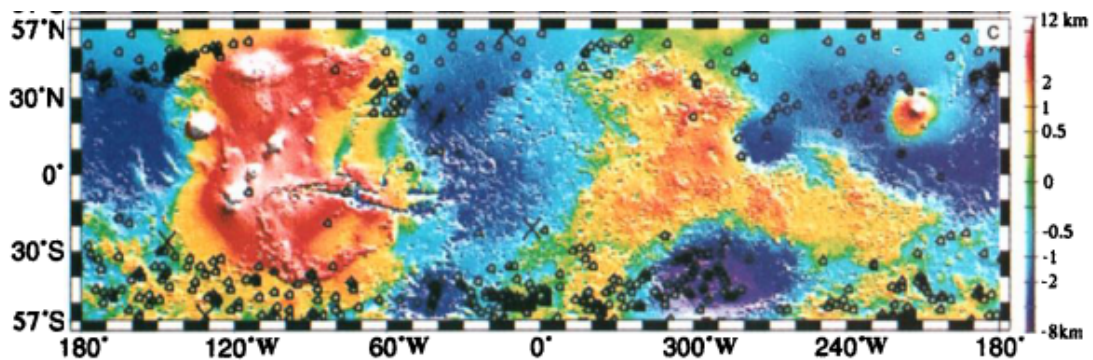


Figure 1.1: Dots indicate the spatial distribution of dust storms observed by MOC in 1999. The topography maps (color) are resolved to $1^\circ \times 1^\circ$ and span $57^\circ\text{S} \sim 57^\circ\text{N}$ (latitude) and $180^\circ\text{W} \sim 180^\circ\text{E}$ (longitude) [Cantor *et al.*, 2001].

1.1.3 Numerical studies of Martian dust cycle

Since the beginning of the 2000s, new MGCMs have been developed to understand the dust cycle in the Martian atmosphere. The uprising of dust from ground to atmosphere was first simulated by the Martian general circulation model (GCM) developed in the Laboratory of Dynamic Meteorology in France (LMD) and the Atmospheric, Oceanic and Planetary Physics laboratory at Oxford University (AOPP) [Newman *et al.*, 2002a]. To simulate seasonal dust opacity, these groups parameterized dust lifting based on realistic physical processes (the details are described in Chapter 2.3) and radiatively interactive dust. Dust can be lifted in two ways: by near-surface wind stress and by convective motion. Although their parametrization yielded realistic annual and interannual behaviors, global storms and variability remain difficult to simulate [Newman *et al.*, 2002b]. At the Geophysical Fluid Dynamics Laboratory, the seasonal dust cycle in the atmosphere was simulated by a Martian GCM with dust lifting based on the LMD/AOPP model. In this model, the atmospheric temperature properly cycled between northern winter and summer only when the background dust was supplied appropriately [Basu *et al.*, 2004, 2006]. The NASA-Ames group employed a Martian GCM to model seasonal dust lifting and sedimentation, parametrizing the dust emission. This simulation suggested two mechanisms underlying the seasonal dust opacity. First, uplifting by wind stress maintains a high optical depth during the southern spring and summer; second, convective lifting supplies background dust during the northern spring and summer [Kahre *et al.*, 2006].

Not only the dust in the atmosphere but also the relationship between dust and water cycle have been understood. LMD group developed the Martian general circulation model for the water cycle in the atmosphere with improved microphysics and radiatively active water ice clouds [Mavarro *et al.*, 2014]. They suggested the importance of cloud microphysics; nucleation on dust particles, ice particle growth, and scavenging of dust particles due to the condensation of ice for dust cycle.

1.2 Objectives of this study

As mentioned in the previous section, dust storms play a critical role in the Martian climate. Observational studies have revealed regions of dust storms, active seasons, frequencies, and influencing factors. However, the dust cycle in the Martian atmosphere remains understood incompletely; in particular, how dust storms evolve and are maintained has not been clarified. According to numerical studies, dust lifting during the southern summer, when the dust optical depth attains the annual maximum, is predominantly maintained by wind stress. However, the interaction between the atmospheric dynamics and the dust supplied by the wind stress is largely unknown. The seasonal behavior of dust lifting along the edge of the polar cap in the northern hemisphere deserves special attention because regional dust storms are frequently observed there. This thesis initially reports the temporal development of regional dust storms in the northern hemisphere. We focus on the interactions between the atmospheric dynamics and dust uplifting. The former is affected by the heating of airborne dust particles, and the latter is governed by physical processes. One goal of this study is to clarify the generation of regional dust storms. We also report the environment in which global dust storms are generated. At the beginning of the global dust storm in 2001 (MY25), regional dust storms were observed simultaneously [Smith *et al.*, 2001]. In the latter half of this study, we discuss how regional dust storms might immediately arise from the strong surface wind maintained in the lower atmosphere.

To achieve our study goals, we developed dust lifting schemes, and implemented them in our Mars general circulation model. The new model can simulate the dust entering the atmosphere from the ground, the atmospheric transportation of dust, and gravity sedimentation. The numerical model is detailed in Chapter 2. The model performance was evaluated in sensitivity experiments. Dust cycles were simulated by two mechanisms of dust lifting, namely, near-surface wind stresses and convective motion. Both schemes depend on the parameters of the dust lifting parameterization. The results of the parameter dependencies are described in Chapter 3. We find that dust storms occur on regional and

encircling scales. The mechanism of the temporal development of regional dust storms is described in Chapter 4. Important interactions among airborne dust, atmospheric tides, and surface conditions are identified in this chapter. Chapter 5 discusses the triggers of global dust storms, focusing on the synchronicity of dust storm generation. A summary of the study, conclusions, and future perspectives are presented in Chapter 6.

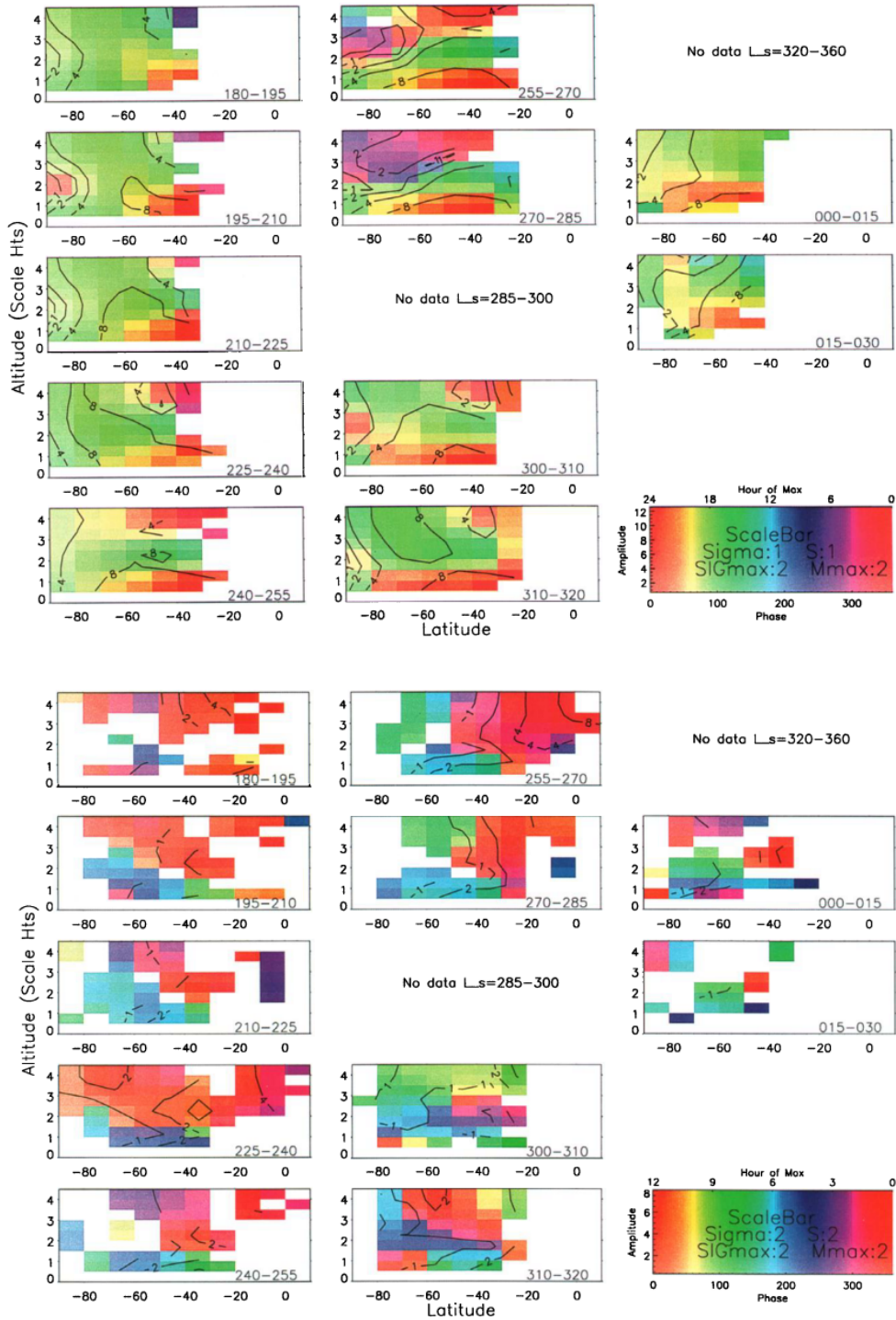


Figure 1.2: Top: The amplitude (contours) and phase (shaded) of the Sun-synchronous, diurnal tide calculated from temperatures observed by MGS-TES in MY24. Bottom: As above but calculated for the semi-diurnal tide. [Banfield et al., 2000].

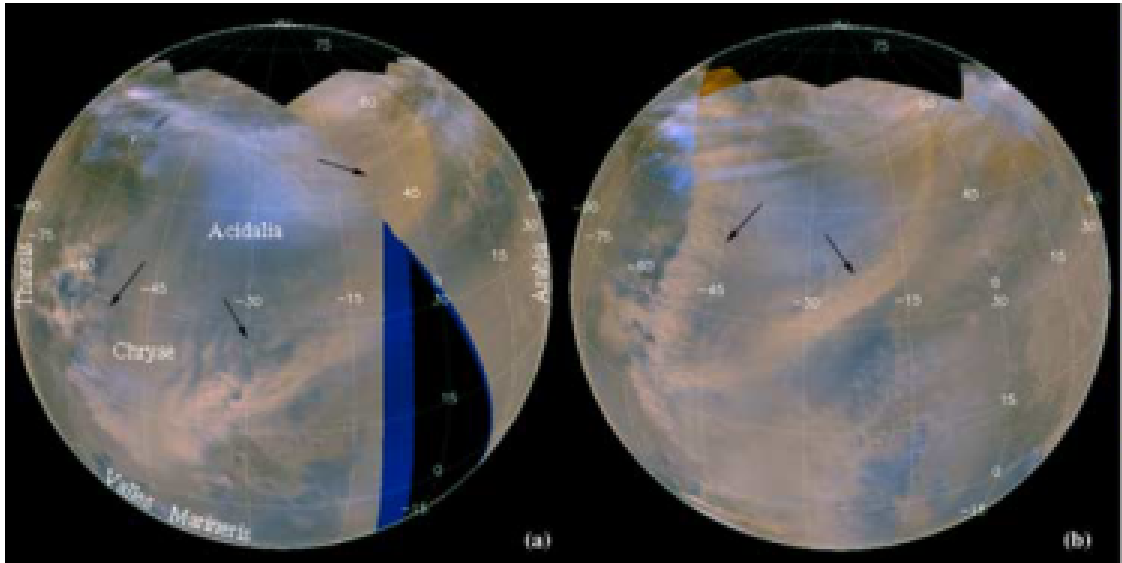


Figure 1.3: MGS-MOC images of regional storms during southern hemisphere summer in MY24. Regional dust storms move to east [Wang *et al.*, 2003].

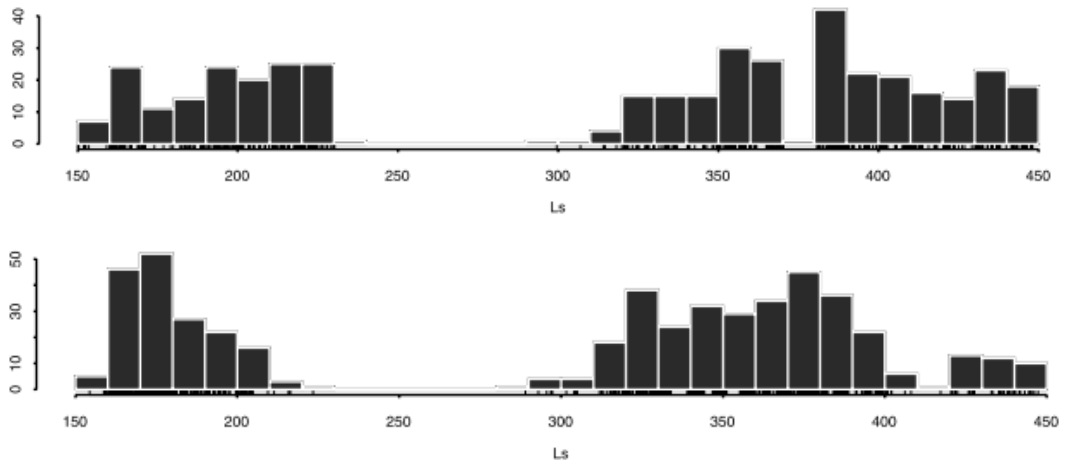


Figure 1.4: Top: Histogram for the number of storms in MY24 within each 10 L_S bin as a function of L_S . Bottom: Same as Top but in MY25 [Wang *et al.*, 2005].

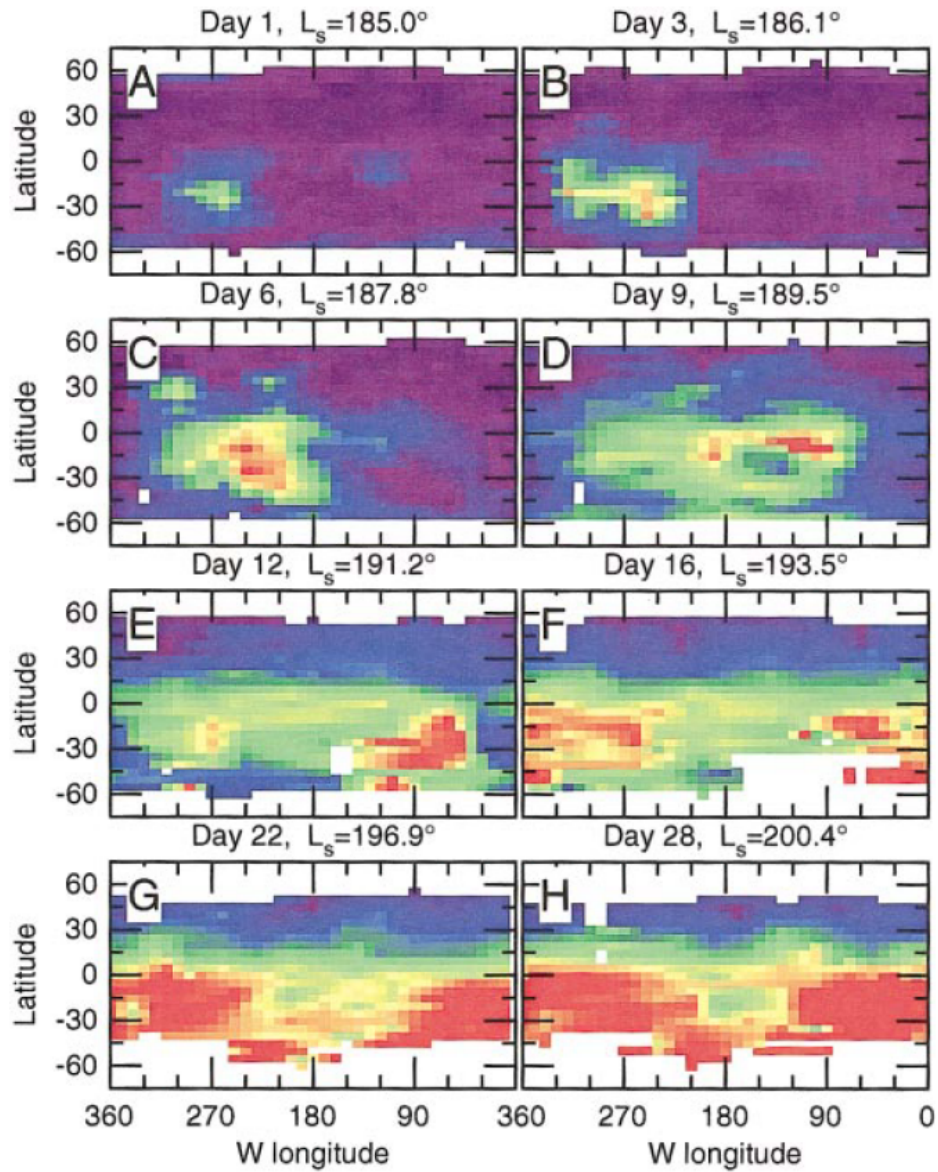


Figure 1.5: Maps of dust opacity (1075 cm^{-1}) showing the initiation and growth of the planet-encircling dust storm in MY25. Dust opacity is graded as follows: 0.2 (purple), 0.5 (blue), 1.0 (green), 1.5 (yellow), and $2.0 \leq$ (red). A dust opacity of unity or higher (green, yellow, or red in the figures) is considered very dusty and typifies dust storm conditions. (A) $L_S = 185.0^\circ$, (B) $L_S = 186.1^\circ$, (C) $L_S = 187.8^\circ$, (D) $L_S = 189.5^\circ$, (E) $L_S = 191.2^\circ$, (F) $L_S = 193.5^\circ$, (G) $L_S = 196.9^\circ$, (H) $L_S = 200.4^\circ$. Opacities are scaled to an equivalent 6.1 hPa pressure level to remove topographical effects. [Smith *et al.*, 2001].

Chapter 2

Model description

This chapter outlines the numerical model and describes the dust lifting schemes.

2.1 Basic features

The Mars GCM, named **D**ynamics, **R**Adiation, **M**Aterial Transport and their mutual **I**nteractions (DRAMATIC), is a three-dimensional spectral model of the Martian atmosphere [Kuroda *et al.*, 2005]. This model is based upon the CCSR/NIES/FRCGC MIROC4.0. The horizontal resolution is $\sim 5.6^\circ$ longitude \times 5.6° latitude. The vertical resolution, in pressure normalized sigma coordinates, is 69 layers (see Table 2.1). The highest altitude is approximately 130 km. The physical parameters of the terrestrial environment are replaced by Martian ones. The terrestrial and Martian parameters are compared in Table 2.2. Topography, surface albedo, thermal inertia, and roughness height data are included in this model. The topography and roughness height are based on observations by the Mars orbiter Laser Altimeter on MGS [Smith *et al.*, 1999; Heavens *et al.*, 2008]. The surface albedo and thermal inertia are those used in the LMD/AOPP Mars GCM [Forget *et al.*, 2001].

Table 2.1: Vertical resolution in the MGCM model. Approximate altitudes are calculated as $z = -H \ln \sigma$, where H is the Martian scale height (10.8 km). Note that the scale height becomes thinner in the upper atmosphere, so the highest altitude in the model is lower than presented in this Table.

Layer	σ levels	Altitude [km]	Layer	σ levels	Altitude [km]
1	0.9950000E+00	0.1	36	0.8300110E-02	51.7
2	0.9850000E+00	0.2	37	0.6797010E-02	53.9
3	0.9750000E+00	0.3	38	0.5568410E-02	56.1
4	0.9650000E+00	0.4	39	0.4559590E-02	58.2
5	0.9524900E+00	0.5	40	0.3732050E-02	60.4
6	0.9374900E+00	0.7	41	0.3054370E-02	62.5
7	0.9199900E+00	0.9	42	0.2500530E-02	64.7
8	0.8999900E+00	1.1	43	0.2047070E-02	66.9
9	0.8749700E+00	1.4	44	0.1676020E-02	69.0
10	0.8437100E+00	1.8	45	0.1372370E-02	71.2
11	0.8073900E+00	2.3	46	0.1123670E-02	73.3
12	0.7623000E+00	2.9	47	0.9200060E-03	75.5
13	0.7059300E+00	3.8	48	0.7531570E-03	77.7
14	0.6344000E+00	4.9	49	0.6166690E-03	79.8
15	0.5465100E+00	6.5	50	0.5049010E-03	82.0
16	0.4534600E+00	8.5	51	0.4133600E-03	84.1
17	0.3711100E+00	10.7	52	0.3384490E-03	86.3
18	0.3038400E+00	12.9	53	0.2771210E-03	88.5
19	0.2487500E+00	15.0	54	0.2268810E-03	90.6
20	0.2036600E+00	17.2	55	0.1857290E-03	92.8
21	0.1667500E+00	19.3	56	0.1520700E-03	94.9
22	0.1365400E+00	21.5	57	0.1245020E-03	97.1
23	0.1118200E+00	23.7	58	0.1019190E-03	99.3
24	0.9154100E-01	25.8	59	0.8345610E-04	101.4
25	0.7491060E-01	28.0	60	0.6832890E-04	103.6
26	0.6132770E-01	30.1	61	0.5594370E-04	105.7
27	0.5024070E-01	32.3	62	0.4489600E-04	108.1
28	0.4115130E-01	34.5	63	0.3430370E-04	111.0
29	0.3365910E-01	36.6	64	0.2541260E-04	114.3
30	0.2754290E-01	38.8	65	0.1883000E-04	117.5
31	0.2256820E-01	40.9	66	0.1394780E-04	120.7
32	0.1847820E-01	43.1	67	0.1033110E-04	124.0
33	0.1513200E-01	45.3	68	0.7516720E-05	127.4
34	0.1238520E-01	47.4	69	0.2600910E-05	138.9
35	0.1013800E-01	49.6			

Table 2.2: The physical parameters used in this model

Parameters	Mars	Earth
Radius of planet [km]	3397	6378
Atmospheric specific heat at constant pressure [$\text{J K}^{-1}\text{kg}^{-1}$]	735.9	1000
Gravity acceleration [ms^{-2}]	3.72	9.81
Atmospheric gas constant [$\text{J K}^{-1}\text{kg}^{-1}$]	188.86	287
Second per a solar day [s]	88775	86400
Sols per a year [Sol]	669	365
Eccentricity	0.0934	0.0167
Obliquity [degree]	25.19	23.45

2.2 Martian physical processes

The DRAMATIC MGCM models various Martian physical processes such as CO_2 condensation and sublimation [Forget *et al.*, 1998]. The model radiative transfer scheme accounts for the absorption and emission by the CO_2 gas and also the absorption, emission, and scattering by the floating dust. Some existing Martian GCMs evaluate the seasonal dust distributions in the atmosphere from observational data. In this study, we developed a dust lifting scheme, and implemented it into our GCM. The scheme accounts for dust lifting, transport of dust by local winds, and gravitational sedimentation. The scheme is interactive because the simulated dust distributions affect the radiative calculations, thus providing feedback to the atmospheric wind and temperature.

2.3 Dust lifting parameterization

Our model uses dust lifting processes to simulate the spatial and temporal distributions of dust in the Martian atmosphere. Dust is injected into the atmosphere by two schemes.

2.3.1 Wind stress parameterization

Wind tunnel experiments conducted at Martian pressure and temperature reveal that very high winds are required to uplift the micron and submicron-sized dust particles observed in the Martian atmosphere [Greeley *et al.*, 1992]. Instead, sand-sized particles (less than 100 μm) are injected by a motion called "saltation". As these larger dust particles descend and impact on the dust-coated surface, they launch micron and submicron-sized dust particles into the atmosphere. To evaluate the injection of dust particles into the atmosphere, we assume that dust particles enter the atmosphere if the stress generated by the near-surface wind exceeds a certain threshold [Newman *et al.*, 2002a, Kahre *et al.*, 2006]. The wind stress for the dust lifting depends on the wind velocity, and is given by

$$\tau = \rho u_d^2, \quad (2.1)$$

where τ represents the near-surface wind stress resolved by the MGCM. ρ is the air density in the lowest atmospheric layer of the model, and u_d is the frictional velocity, given by

$$u_d = \Upsilon \times \frac{ku(z_0)}{\ln(z_0/z_{00})}, \quad (2.2)$$

where $u(z_0)$ is the near-surface wind velocity at height z_0 . z_{00} is the surface roughness height, and $k = 0.4$ is von Karman's constant. z_0 is defined as 10 m everywhere. Υ , taken from Haberle *et al.* [1999], is the function of Richardson number, and indicates the stability of the air to ground. Richardson number is given by

$$Ri = \frac{gd\theta/dz_0}{(dU/dz_0)^2}, \quad (2.3)$$

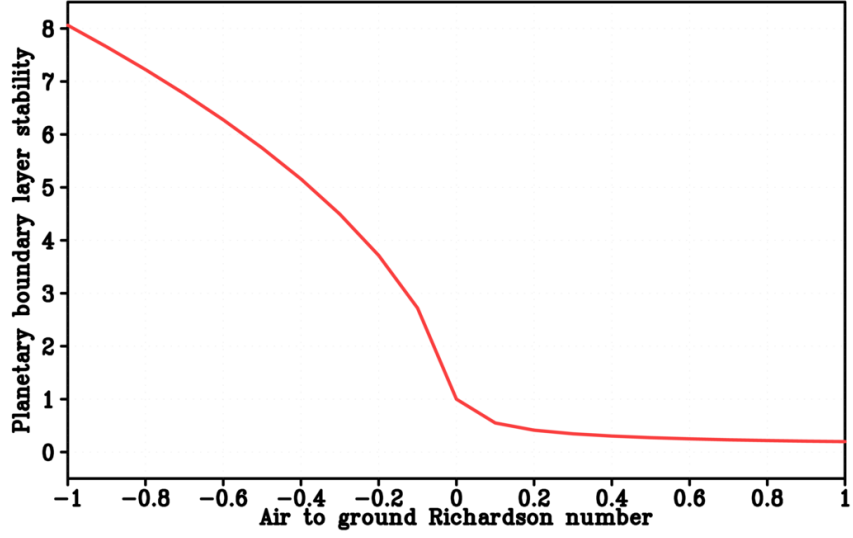


Figure 2.1: Relationship between PBL stability and air-to-ground Richardson number proposed by *Haberle et al.* [1999].

where g is gravity acceleration. θ/d_0 is potential temperature and U is the magnitude of wind at 10m from the ground. Thus, Υ is defined when $Ri \leq 0$,

$$\Upsilon = (1 - 64Ri)^{1/2} \quad (2.4)$$

and when $Ri > 0$,

$$\Upsilon = (1 + [10Ri/(1 + 5Ri)^{1/2}])^{-1}. \quad (2.5)$$

The functional forms for the dust flux have been developed on the theoretical assump-

tion and wind tunnel experiments. Generally, the formulas show a cubic dependence upon the wind stress. In this study, the form is the same as that of *Newman et al.* [2002a]:

$$F_{wsl} = \max[\alpha_{wsl} \times \frac{1}{g \sqrt{\rho}} (\sqrt{\tau^*} - \sqrt{\tau})(\sqrt{\tau^*} + \sqrt{\tau})^2, 0], \quad (2.6)$$

where τ^* is the threshold wind stress for lifting and α_{wsl} is a injection parameter (tunable parameter) which determines magnitude of the dust emission. The thresholds have never observed directly, however the wind velocity which can lift up dust particles from the surface was estimated by some laboratory experiments. According to the laboratory experiments, the range of thresholds was determined [*Greeley et al.*, 1992, 2003].

2.3.2 Convective parameterization

According to past observations, Martian atmospheric dust is supplied by small-scale convective motions called dust devils. Our GCM employs dust devil activity to simulate the observed annual background dust opacity. This scheme is based on the thermodynamics of dust devils described by *Rennó et al.* [1998] and a numerical model developed by *Newman et al.* [2002a] and [2002b], in which heat is exchanged between the surface and the atmosphere. The lifting condition is defined as

$$F_{dda} = \alpha_{dda} \times F_s \times (1 - b). \quad (2.7)$$

where F_{dda} is the activity of the dust devil, F_s is the sensible heat flux on the ground, α_{dda} is a tunable efficiency parameter, and b is defined as

$$b = \frac{(1 - \zeta^{\chi+1})}{(1 - \zeta)(\chi + 1)\zeta^\chi}. \quad (2.8)$$

ζ is given by

$$\zeta = \frac{p_{top}}{p_0}, \quad (2.9)$$

where p_0 is the surface pressure, p_{top} is the pressure at the top of the PBL, and χ is the specific gas constant divided by the specific heat capacity at constant pressure. In this parameterization, dust is lifted in regions of positive surface heat flux. Therefore, during daylight hours, dust devil lifting occurs at all surfaces not covered with CO₂ ice caps.

2.3.3 Planetary boundary layer

The structure and dynamics of the near-surface atmosphere were observed by Mars Express, which obtained numerous vertical temperature profiles [Hinson *et al.*, 2008]. Most of these profiles revealed the depth of the PBL. The convection is sourced from solar heating of the ground, and the vertical extent of the PBL is a function of the static stability.

$$S = \frac{dT}{dz} + \frac{C_p}{g}, \quad (2.10)$$

where dT/dz is the vertical temperature gradient and C_p is the specific heat capacity at constant pressure. The altitude at which the static stability abruptly changes is assumed as the top of the PBL. The total surface dust flux is simulated by two schemes:

$$F_{dust} = F_{wsl} + F_{dda}. \quad (2.11)$$

The dust lifted from the ground is uniformly supplied to the above PBL. Typically, the depth of the dust-injected layers is estimated, and two boundary conditions are imposed on the ground. The first assumes an infinite quantity of surface dust. Wherever the heat

flux is positive, dust continues to be rolled up. The second condition stipulates that no dust is lifted from the polar cap.

2.4 Gravitational sedimentation

The model also evaluates the gravitational sedimentation of floating dust particles in the atmosphere. The sedimentation velocity takes the following form *Kasten* [1968]:

$$v_{sed} = \frac{2\rho_d r_d^2 g}{9\eta} \left[1 + \frac{\lambda}{r_d} \left[C_1 + C_2 \exp\left(-\frac{C_3 r_d}{\lambda}\right) \right] \right]. \quad (2.12)$$

The dynamic viscosity η is a function of the temperature T and is given by

$$\eta = \eta_0 \times \frac{533.16}{T + 240} \left(\frac{T}{293.16} \right)^{1.5}, \quad (2.13)$$

where v_{sed} is the sedimentation velocity, ρ_d is the density of the dust particles (2.5 kg m^{-3}), and r_d is the radius of the dust particles ($1 \text{ }\mu\text{m}$). λ is the mean free path of air, $C_1 \sim C_3$ are dimensionless empirical constants, and $\eta_0 = 1.47 \times 10^{-5} \text{ kg m s}^{-1}$.

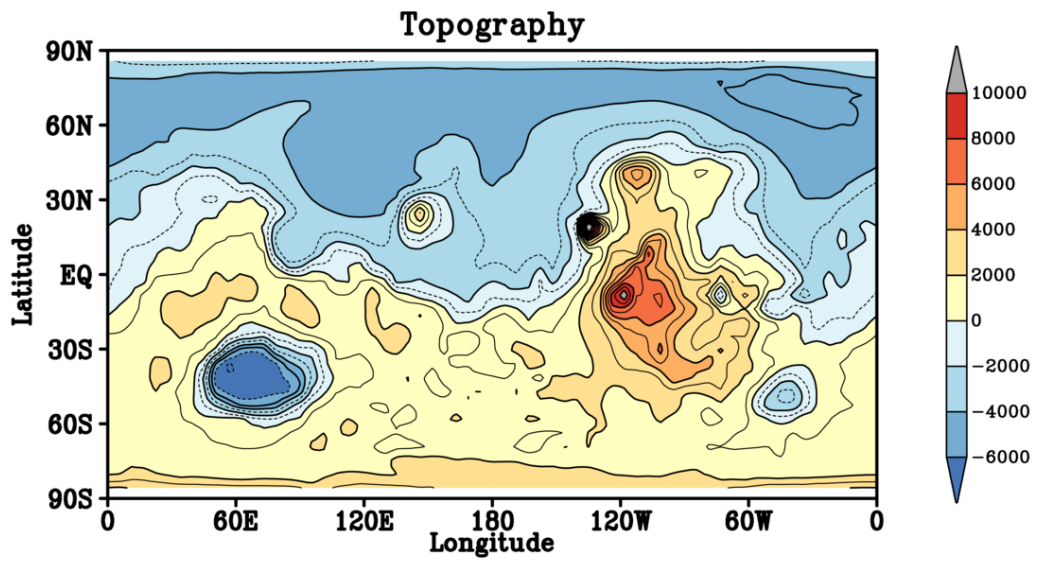


Figure 2.2: Latitude-longitude distribution of the topography [m] used in this model.

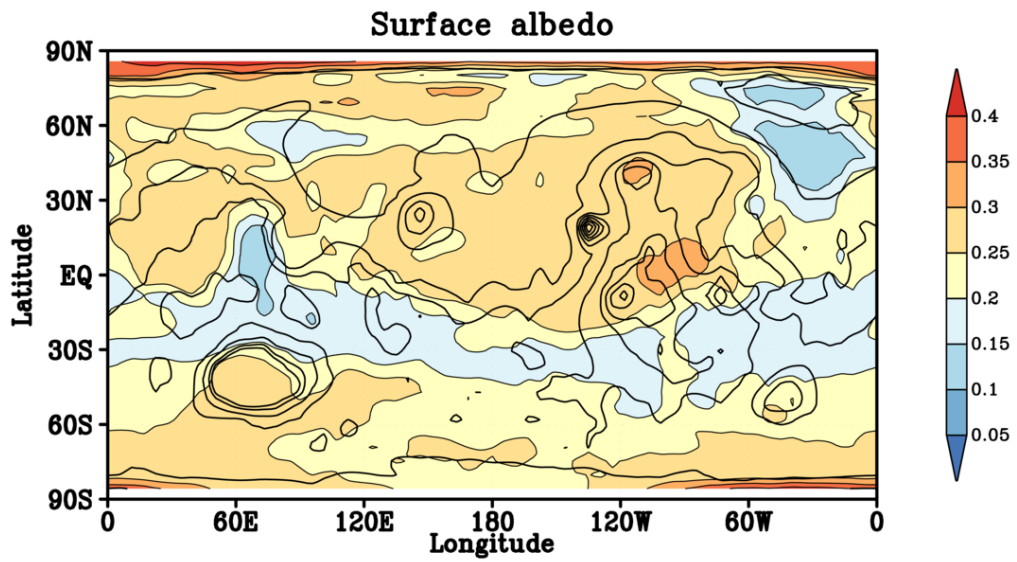


Figure 2.3: Same as Figure 2.2 but surface albedo (thin lines and shades). Thick lines indicate the topography.

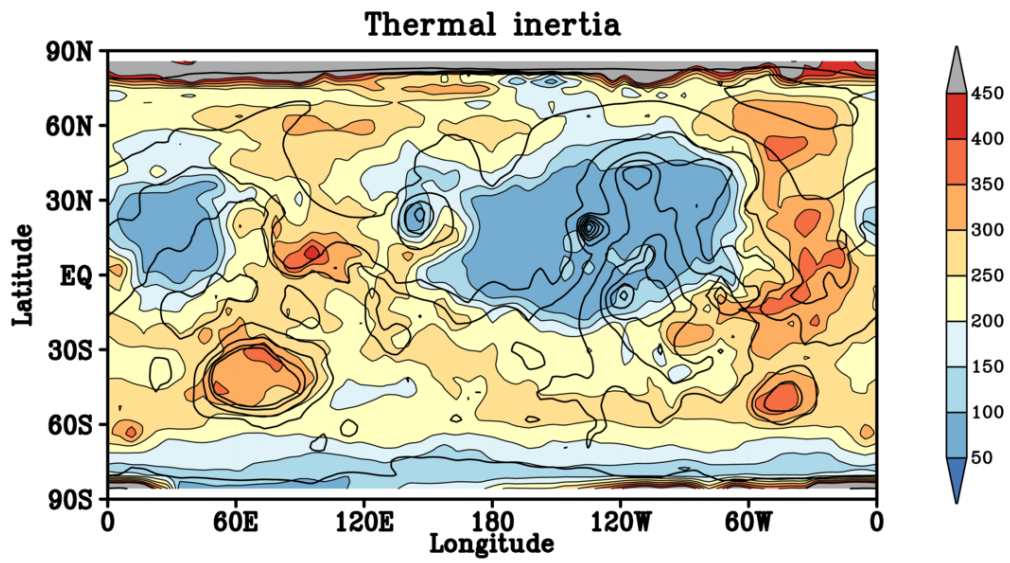


Figure 2.4: Same as Figure 2.2 but thermal inertia [$\text{J m}^{-2} \text{K}^{-1} \text{s}^{-1/2}$] (thin lines and shades).

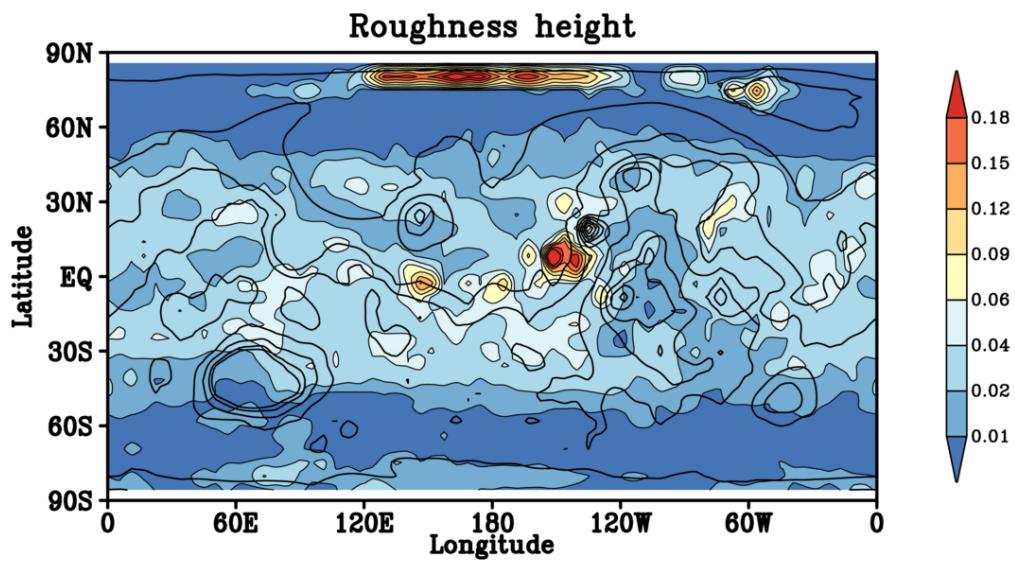


Figure 2.5: Same as Figure 2.2 but roughness height [m] (thin lines and shades).

Chapter 3

Sensitivity of dust lifting parametrization

To adjust the annual dust opacity to observational data, we conducted many sensitivity experiments and model developments. This chapter describes the relationships between the dust behavior and our lifting schemes.

3.1 Experimental design for sensitivity test

In the previous chapter, we introduced two dust lifting parametrizations, near-surface wind stress (denoted WS) and dust devil activity (denoted DD), to simulate the temporal and spatial dust distributions in the atmosphere. To fit our model to the observational dust variations, we evaluated the contributions of both schemes in sensitivity experiments (see Table 3.1). The results of these sensitivity experiments were compared with the dust optical depth observed by Mars Global Surveyor. The dust opacity data used in these comparisons excluded the year of the global dust storm. Isothermal atmosphere and no wind were set as the initial conditions. Spin-up was two Martian years. It is enough for thin Martian atmosphere to reach the equilibrium. The initial conditions and the spin-up

Table 3.1: Types of sensitivity experiments. Three lifting schemes were combined to determine the tunable parameters.

	Near-surface wind stress lifting	Dust devil activity lifting
WS	active	passive
DD	passive	active
WS+DD	active	active

were used by all sensitivity experiments.

3.2 Comparison of model behavior for parameter dependence

Initially, the near-surface wind stress and the dust devil activity schemes were independently integrated into our Mars GCM, and their contributions to the model behaviors were confirmed. After estimating the performances of both schemes, we determined reasonable values of the threshold near-surface wind stress and two injection parameters.

3.2.1 Model sensitivity to wind stress scheme

The values of the threshold and injection rate were selected to generate realistic annual dust opacity. Representative combinations of threshold near-surface wind stresses and injection rates are listed in Table 3.2. Figures 3.1, 3.2, 3.3, and 3.4 are time series of the simulated globally averaged dust opacity. TES observational data are also plotted for comparison. Overall, the simulated globally averaged dust opacity was minimized during the northern spring and summer, and maximized during the southern spring and

Table 3.2: Parameters of the near-surface wind stress scheme used in the sensitivity experiments. These tests determined the best-fit threshold of near-surface wind stress [Pa] and the injection rate. Representative experimental settings are denoted W1 to W16.

	$\alpha_{wsl} = 2.E - 6$	$\alpha_{wsl} = 5.E - 6$	$\alpha_{wsl} = 1.E - 5$	$\alpha_{wsl} = 2.E - 5$
$\tau^* = 0.015$	W1	W2	W3	W4
$\tau^* = 0.030$	W5	W6	W7	W8
$\tau^* = 0.045$	W9	W10	W11	W12
$\tau^* = 0.060$	W13	W14	W15	W16

summer. Lower values of the threshold near-surface wind stress generate time series that reasonably agree with observations during MY24 and MY26 (see Figures 3.1 and 3.2). For instance, during the northern spring and summer, the simulated dust opacity remains constant at approximately 0.1, and gently rises to approximately 0.4 from late northern summer and early southern summer near 350 Sol ($L_S = 167.3^\circ$). The simulated dust opacity deviates from observations during the southern spring and summer. The TES-derived dust opacity exhibits two peaks during the dusty season, which are not forecast by our model. If the near-surface wind stress threshold is set high, the globally averaged dust opacity generally remains constant or only slightly increases throughout one experimental year (see Figures 3.3 and 3.4).

The temporal and spatial variations in dust opacity strongly depend on the magnitude of the simulated dust lifted from the surface. The time series of dust lifting obtained in the sensitivity experiments are presented in Figures 3.5, 3.6, 3.7, and 3.8. In both hemispheres, the upward surface dust flux is more intense during the southern spring and summer (northern fall and winter) than during the southern fall and winter (northern spring and summer). This tendency is consistent with the dust opacity. At low threshold of near-surface wind stress, more dust is lifted in the northern than in the southern hemisphere. As the threshold increases, the magnitude of the surface dust flux increases in the southern hemisphere. This phenomenon is attributed to the shape of the surface dust flux function.

Table 3.3: Parameters of the dust devil activity scheme used in the sensitivity experiments. These tests determined the best-fit injection rate. This table shows a representative experimental setting.

$\alpha_{dda} = 2.E - 10$	$\alpha_{dda} = 5.E - 10$	$\alpha_{dda} = 1.E - 9$	$\alpha_{dda} = 2.E - 9$
D1	D2	D3	D4

Typical patterns of seasonally averaged upward surface dust flux are shown in Figures 3.9, 3.10, 3.11, and 3.12. Dust lifting is enhanced in sloped areas. The northern part of the Hellas basin shows especially high dust activity, with frequent stirring of dust into the atmosphere. Furthermore, during the southern spring and summer, much of the atmospheric dust is sourced from higher mountains in the northern hemisphere (approximately 120°W).

3.2.2 Sensitivity for dust devil scheme

Dust devil scheme accounts for the dust supply caused by convective motion. This parameterization depends on the surface heat flux and surface to air temperature difference. In order to drive this scheme, the injection rate is given as a tunable parameter. Many sensitivity experiments for dust devil scheme were performed and representative values are listed in Table 3.3. Figure 3.13 shows the time series of the simulated globally averaged dust opacities in comparison with TES observations. The predicted seasonal dust opacities change slowly in progress of each season and have a small peak in southern summer. The seasonal variation of the surface dust flux in each hemisphere is smaller than near surface wind stress experiments (see Figure 3.14). Martian perihelion comes in southern hemisphere summer, so the surface dust flux is stronger than in northern hemisphere summer however there is a few differences of the opacity between the northern and southern hemisphere.

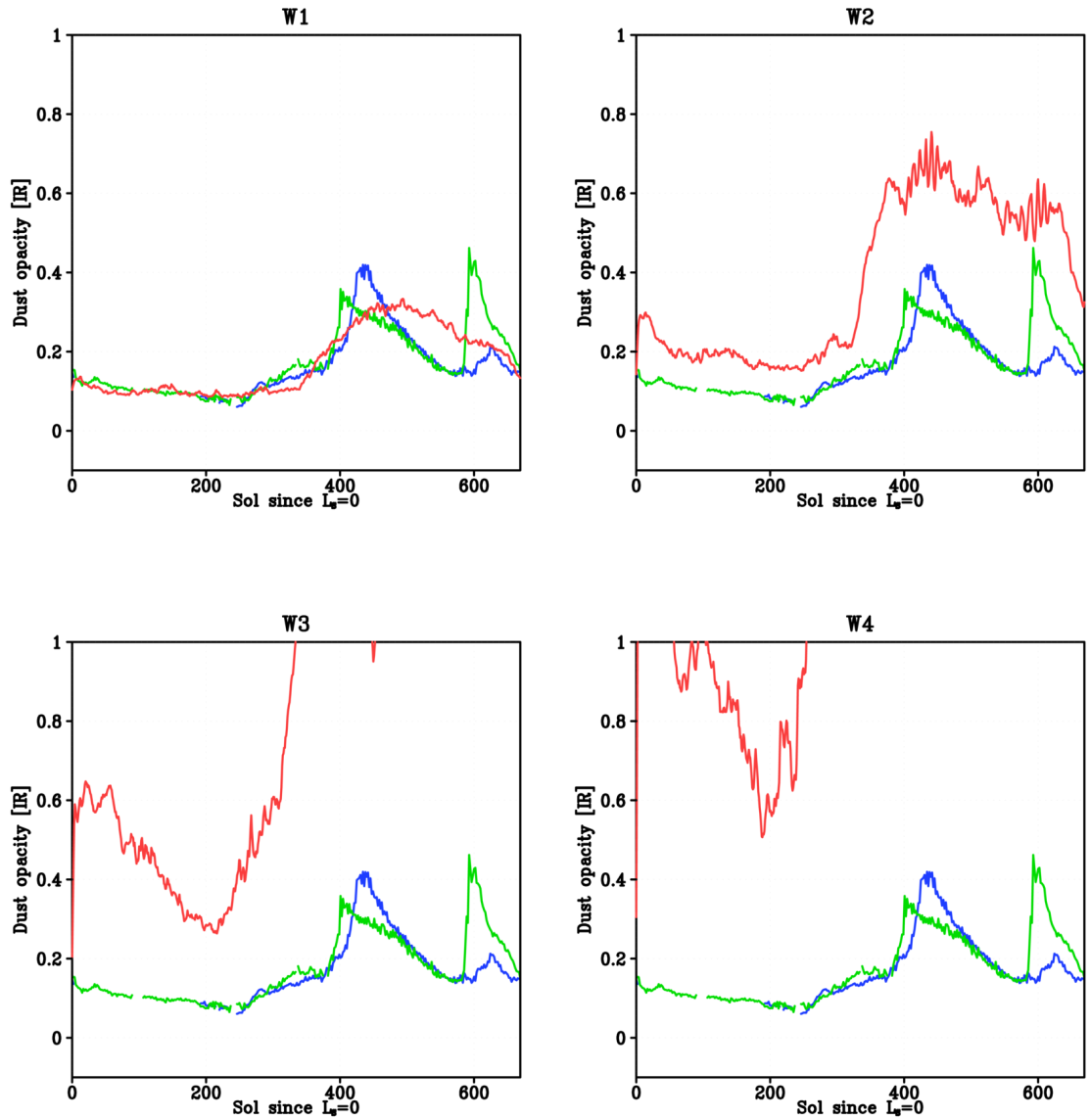


Figure 3.1: Time series of globally averaged dust opacity. The red line is the simulated dust opacity and the threshold near-surface wind stress is 0.015 Pa. Dust injection rates in the near-surface wind stress scheme are 2×10^{-6} (W1), 5×10^{-6} (W2), 1×10^{-5} (W3), and 2×10^{-5} (W4). TES-derived opacity from MY24 (green) and MY26 (blue) is also shown. Opacities are scaled to the 6.1 hPa pressure level. Note that W3 and W4 were computationally terminated at 483 Sol ($L_S = 249.3^\circ$) and 505 Sol ($L_S = 263.6^\circ$) in each experiment because they supplied extreme quantities of dust to the atmosphere.

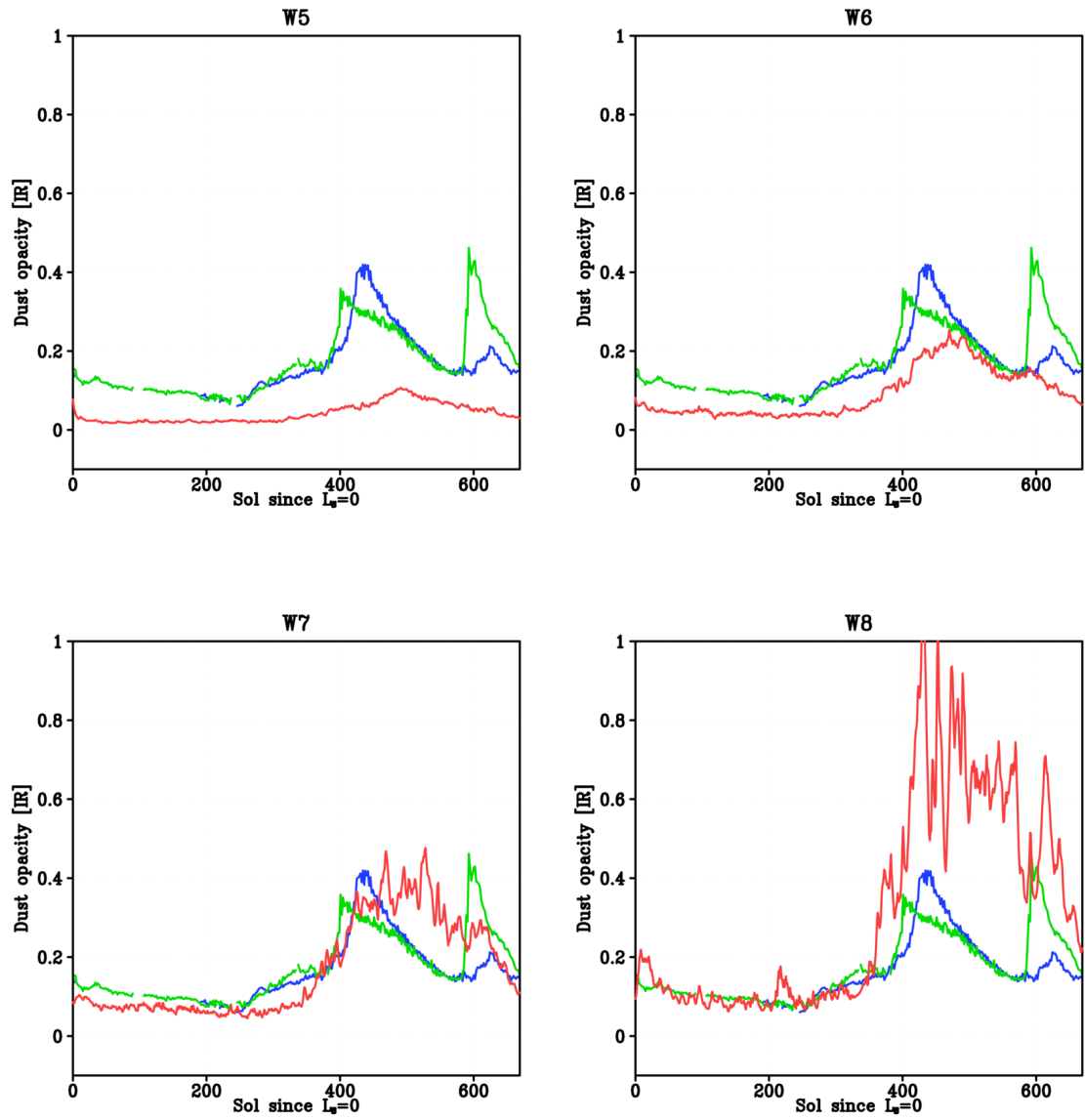


Figure 3.2: Same as Figure 3.1, but threshold near-surface wind stress is 0.030 Pa. Dust injection rates in the near-surface wind stress scheme are 2×10^{-6} (W5), 5×10^{-6} (W6), 1×10^{-5} (W7) and 2×10^{-5} (W8).

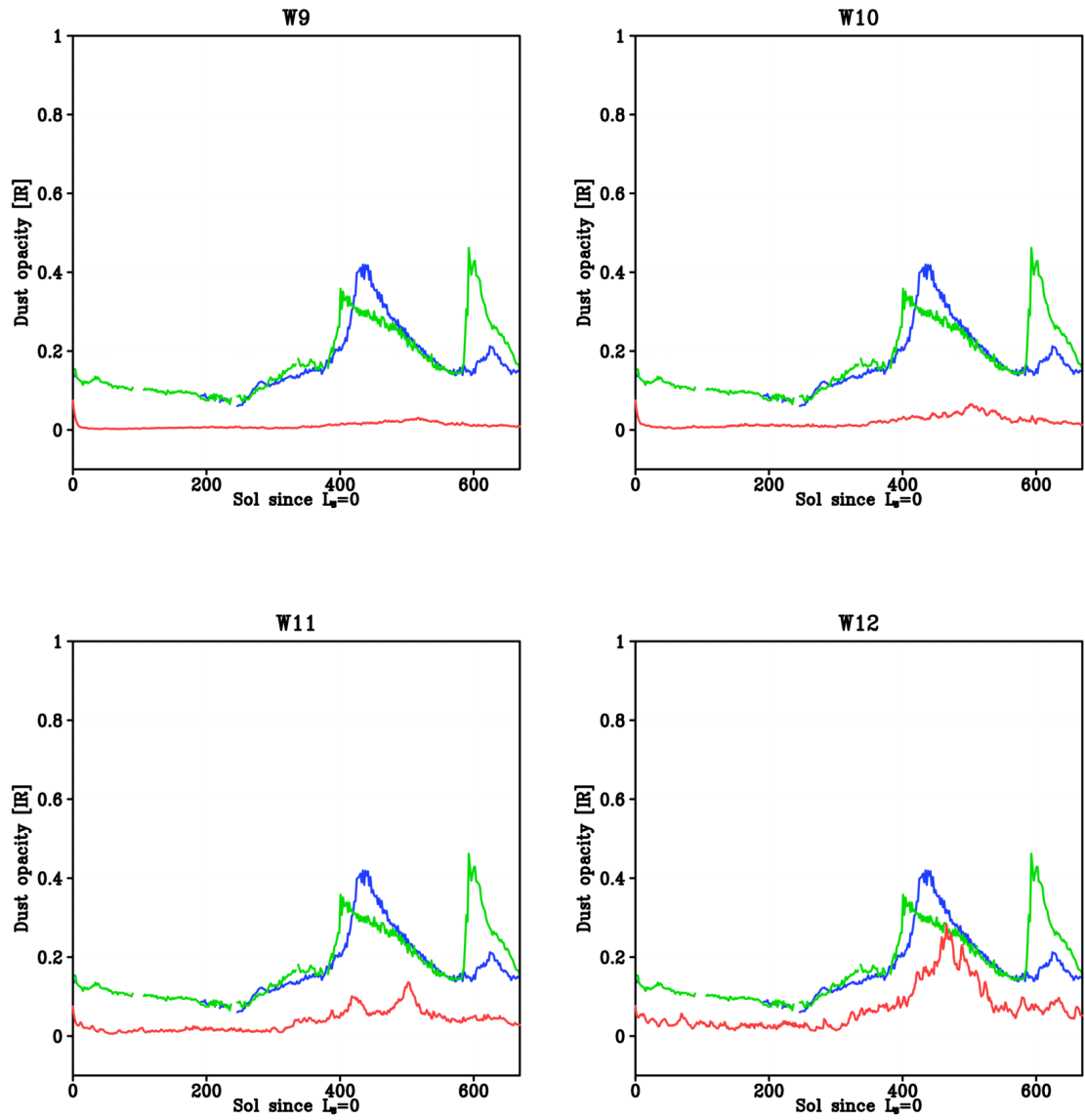


Figure 3.3: Same as Figure 3.1, but threshold near-surface wind stress is 0.045 Pa. Dust injection rates in the near-surface wind stress scheme are 2×10^{-6} (W9), 5×10^{-6} (W10), 1×10^{-5} (W11) and 2×10^{-5} (W12).

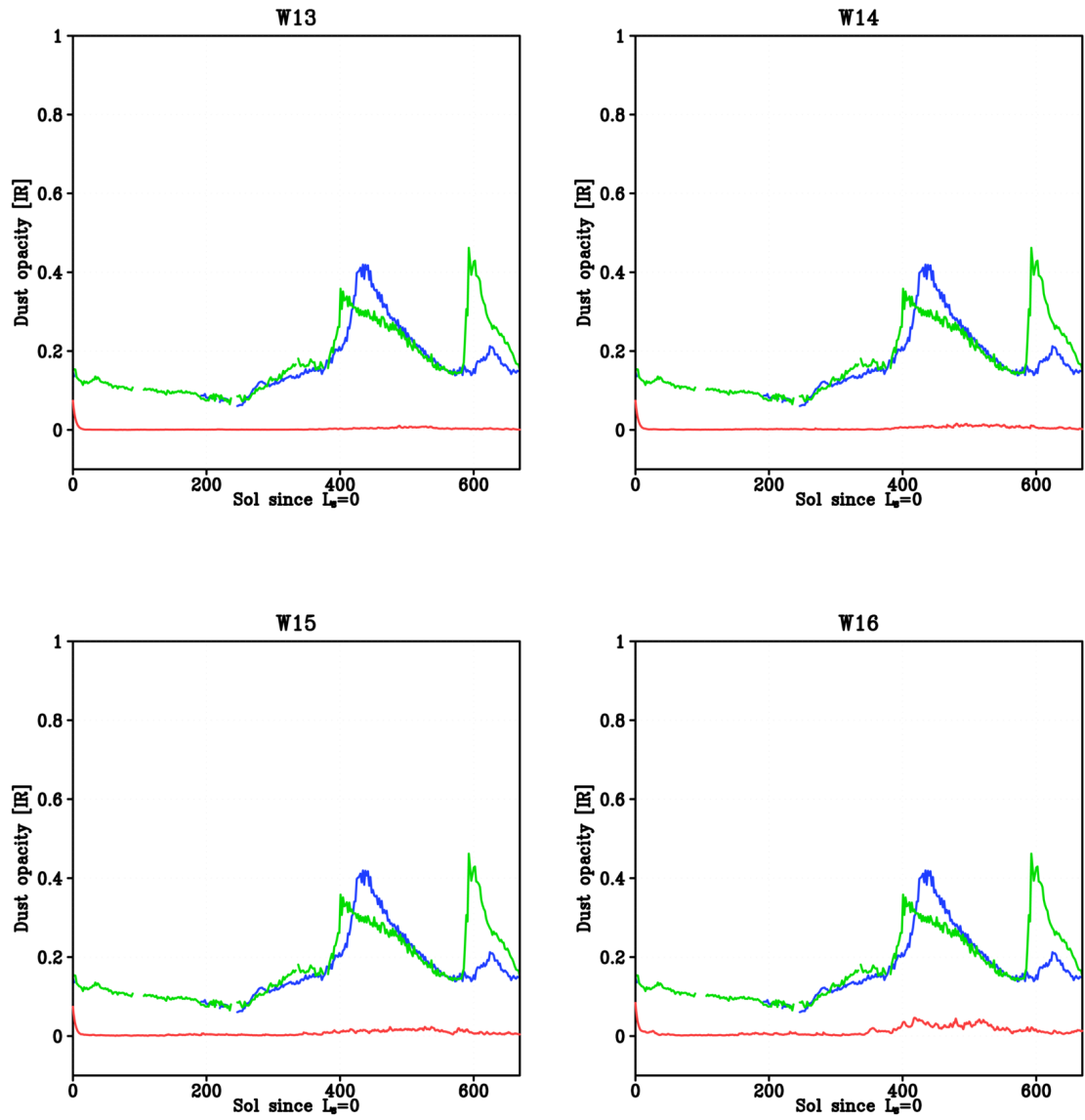


Figure 3.4: Same as Figure 3.1, but threshold near-surface wind stress is 0.060 Pa. Dust injection rates in the near-surface wind stress scheme are 2×10^{-6} (W13), 5×10^{-6} (W14), 1×10^{-5} (W15) and 2×10^{-5} (W16).

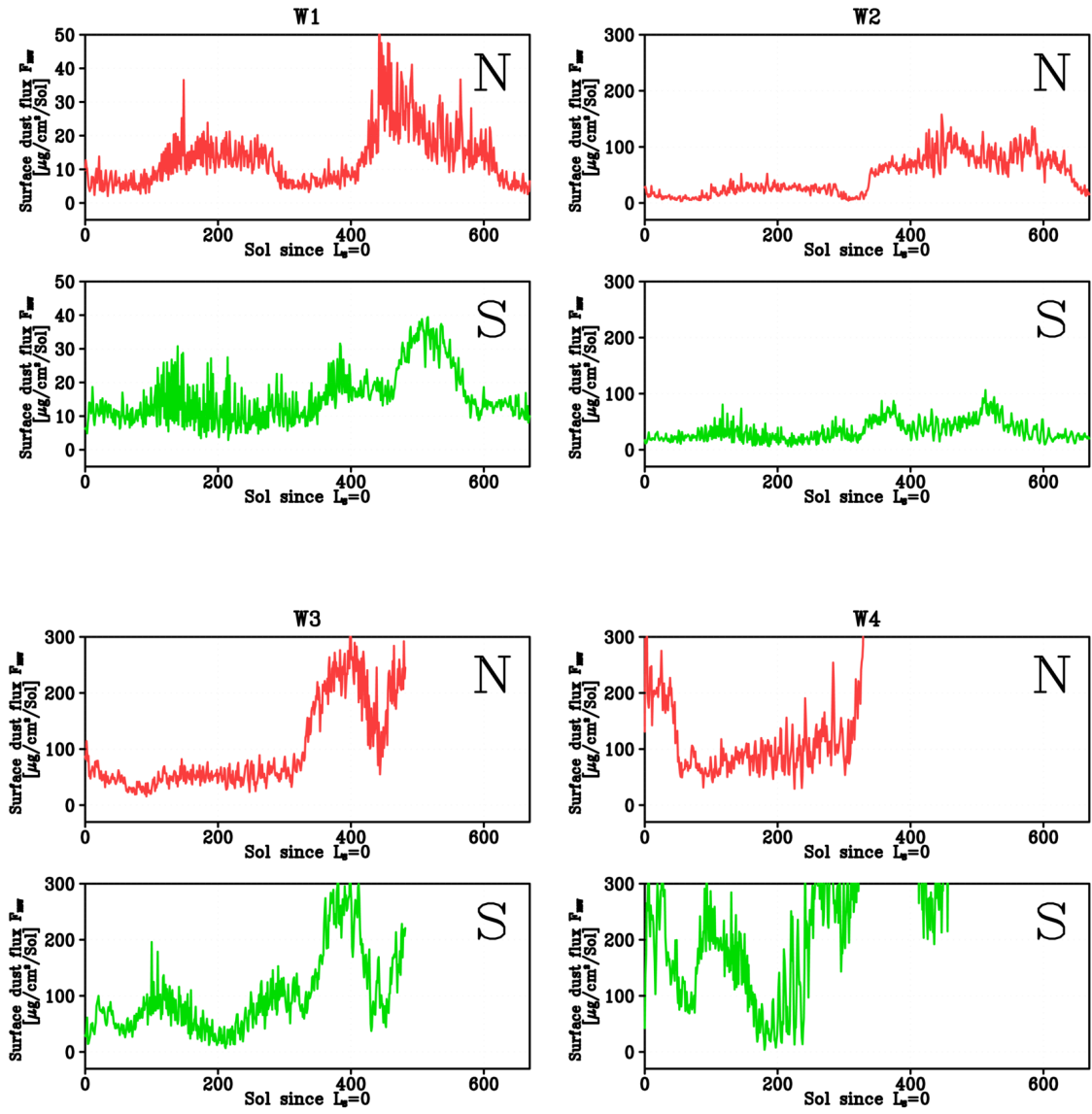


Figure 3.5: Time series of simulated upward surface dust flux $[\mu\text{g cm}^{-2} \text{Sol}^{-1}]$ averaged for each hemisphere. Threshold near-surface wind stress and dust injection rates are provided in the caption of Figure 3.1.

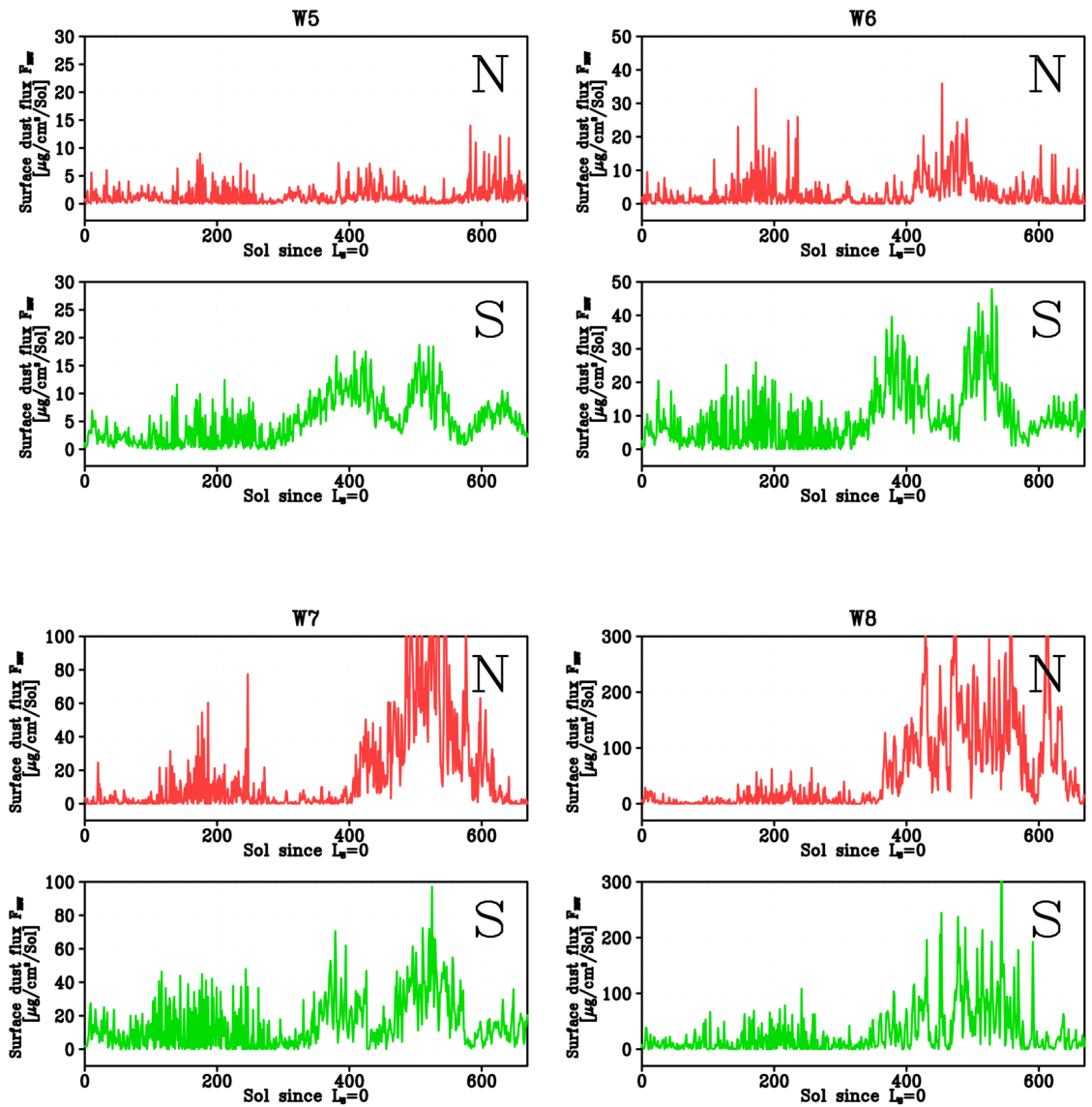


Figure 3.6: Same as Figure 3.5, but threshold near surface wind stress and dust injection rates are same as Figure 3.2.

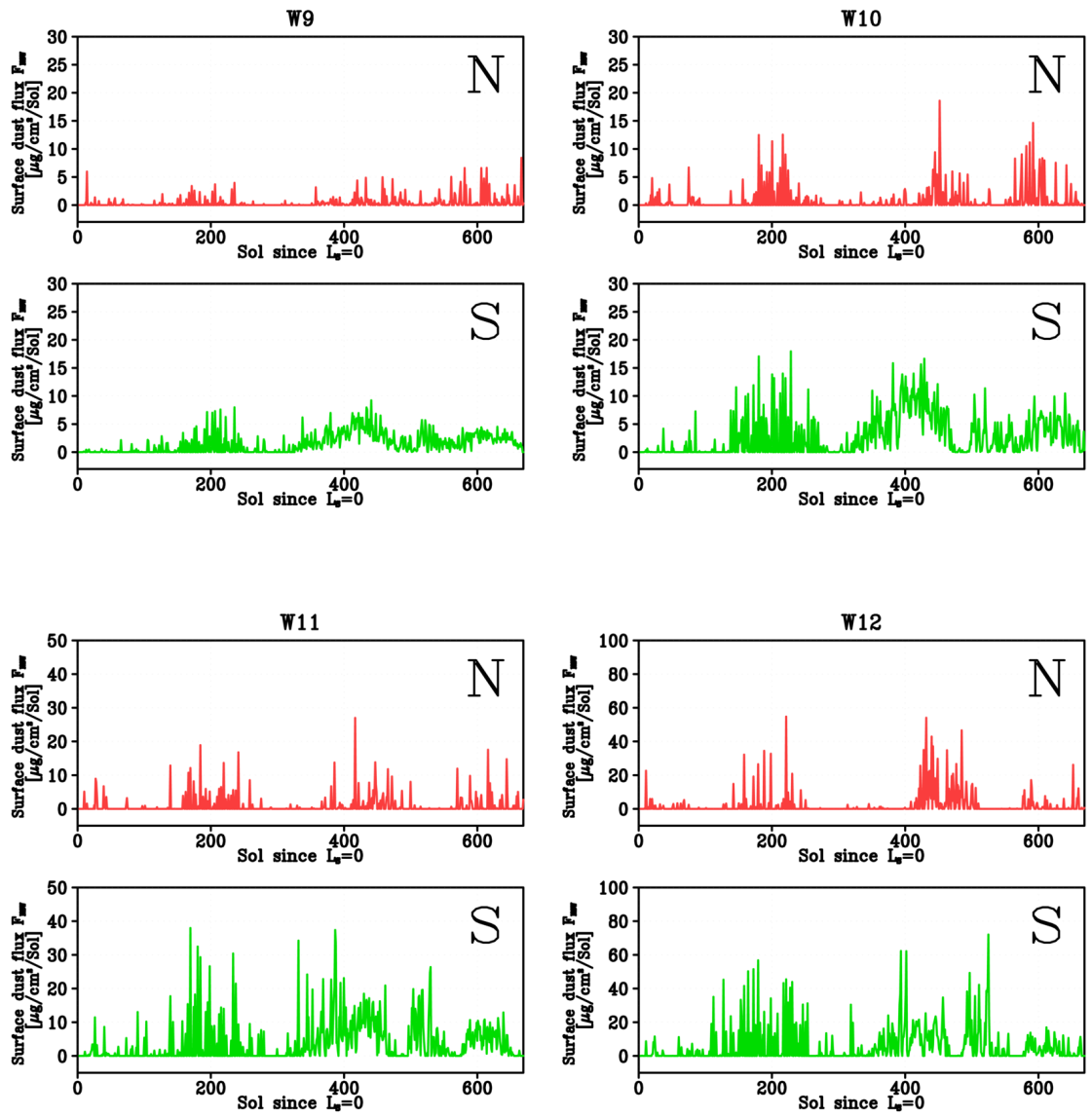


Figure 3.7: Same as Figure 3.5, but threshold near surface wind stress and dust injection rates are same as Figure 3.3.

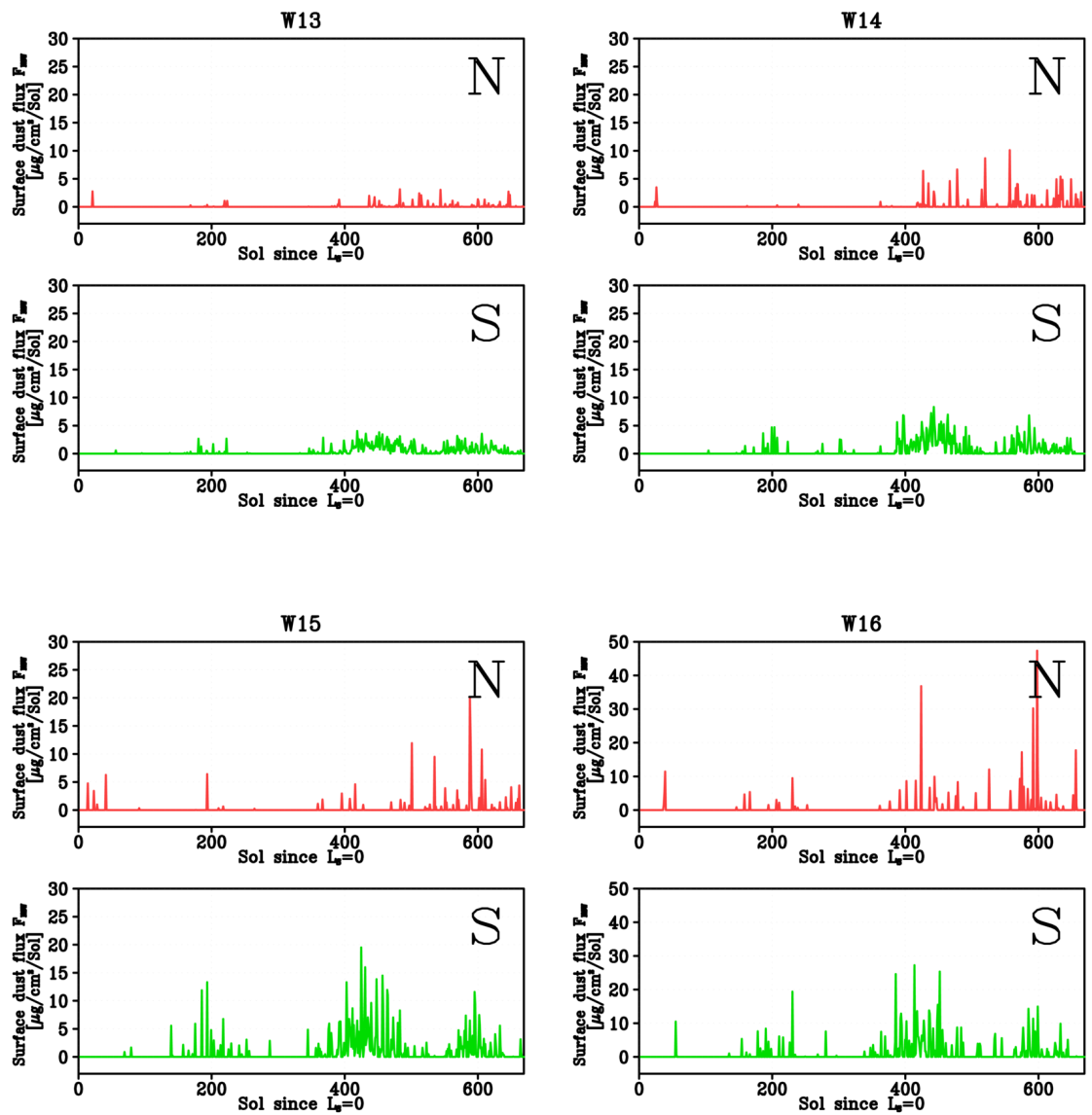


Figure 3.8: Same as Figure 3.5, but threshold near surface wind stress and dust injection rates are same as Figure 3.4.

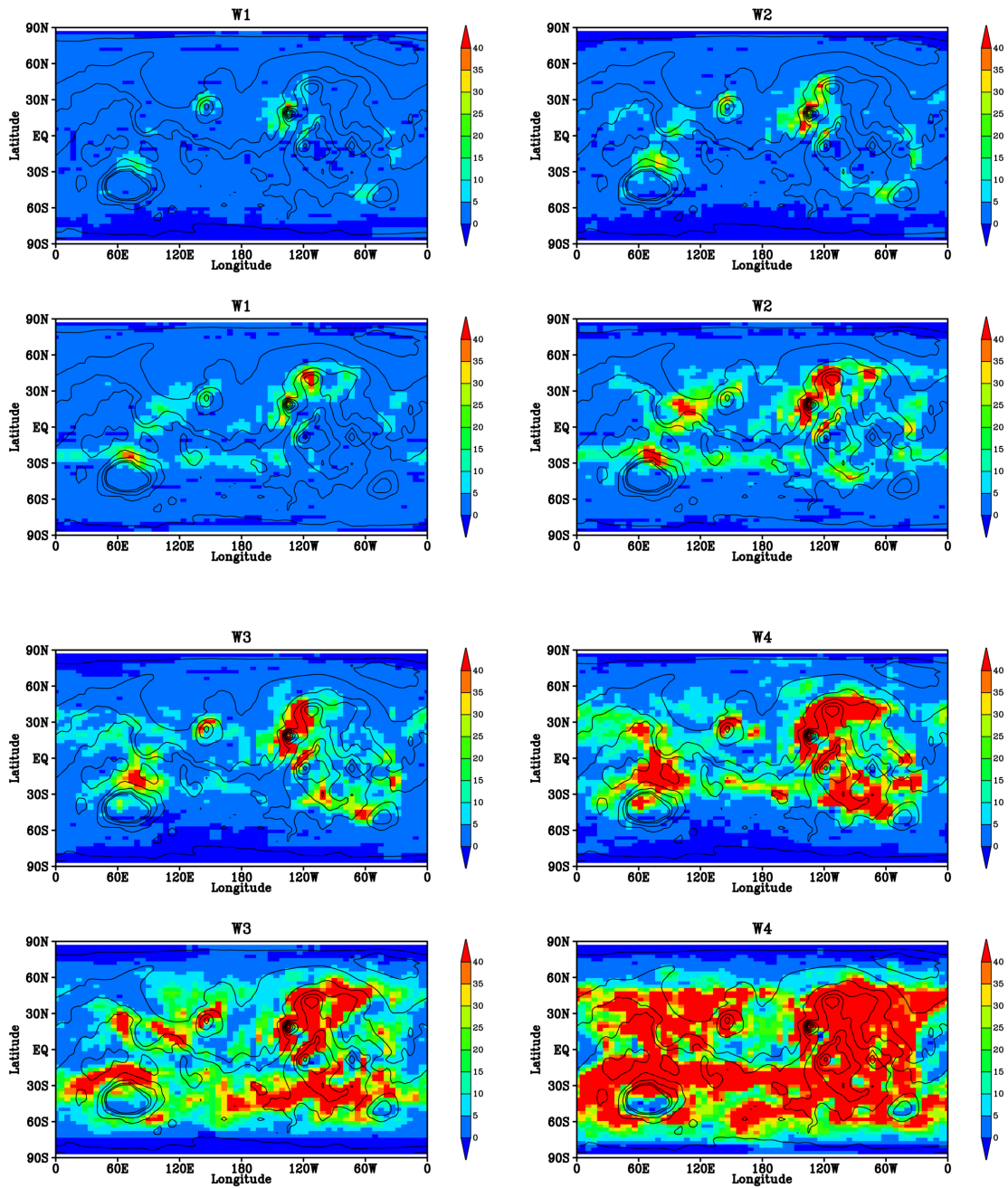


Figure 3.9: Latitude-longitude distribution of upward surface dust flux [$\mu\text{g cm}^{-2} \text{Sol}^{-1}$] averaged between $L_S = 0^\circ$ and 180° (top) and between $L_S = 180^\circ$ and 360° (bottom). Threshold near-surface wind stress and dust injection rates are provided in the caption of Figure 3.1. Note that W3 (bottom) and W4 (bottom) are averaged between $L_S = 180^\circ$ and 249.3° and between $L_S = 180^\circ$ and 263.6° .

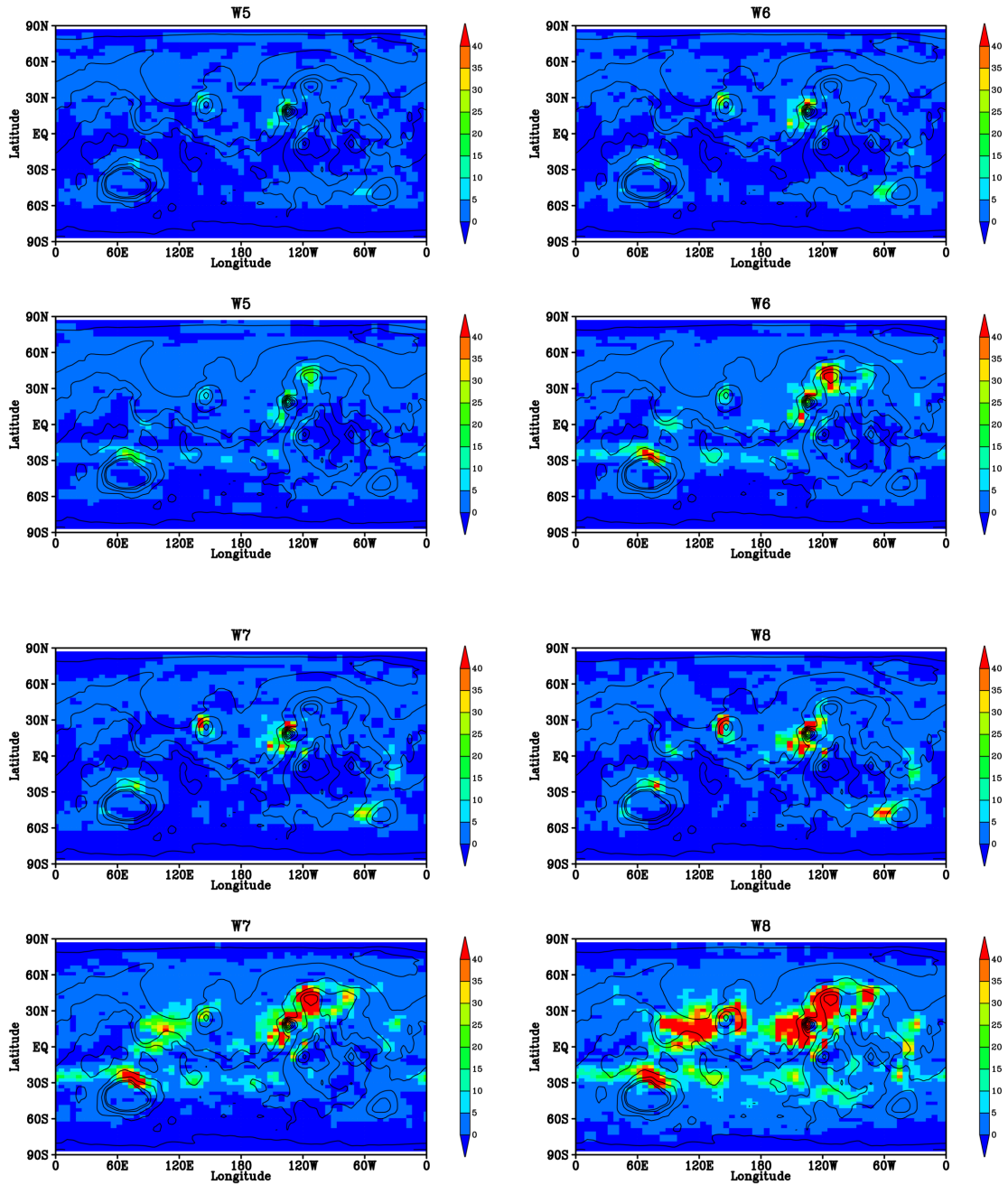


Figure 3.10: Same as Figure 3.9, but threshold near surface wind stress and dust injection rates are same as Figure 3.2.

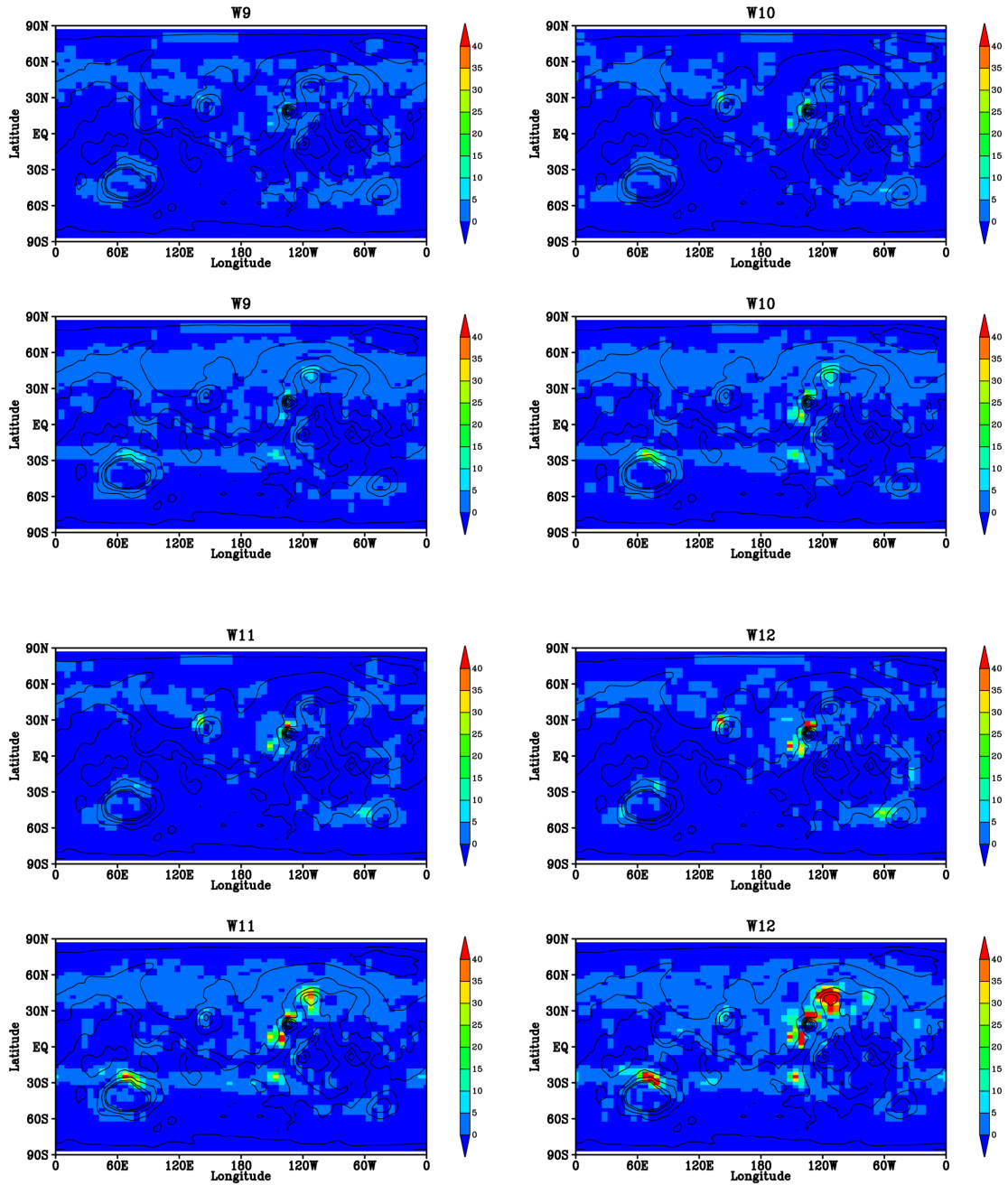


Figure 3.11: Same as Figure 3.9, but threshold near surface wind stress and dust injection rates are same as Figure 3.3.

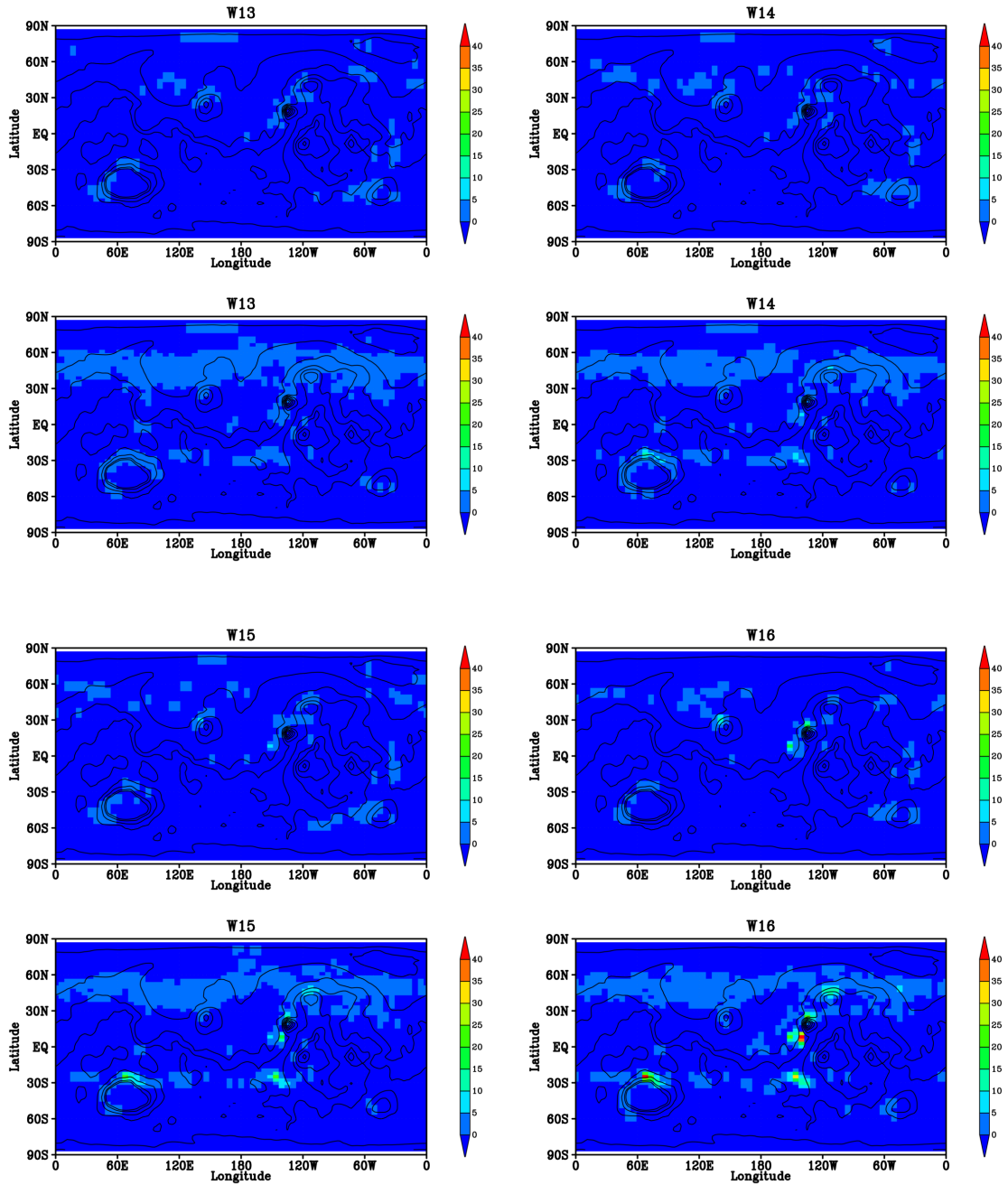


Figure 3.12: Same as Figure 3.9, but threshold near-surface wind stress and dust injection rates are same as Figure 3.4.

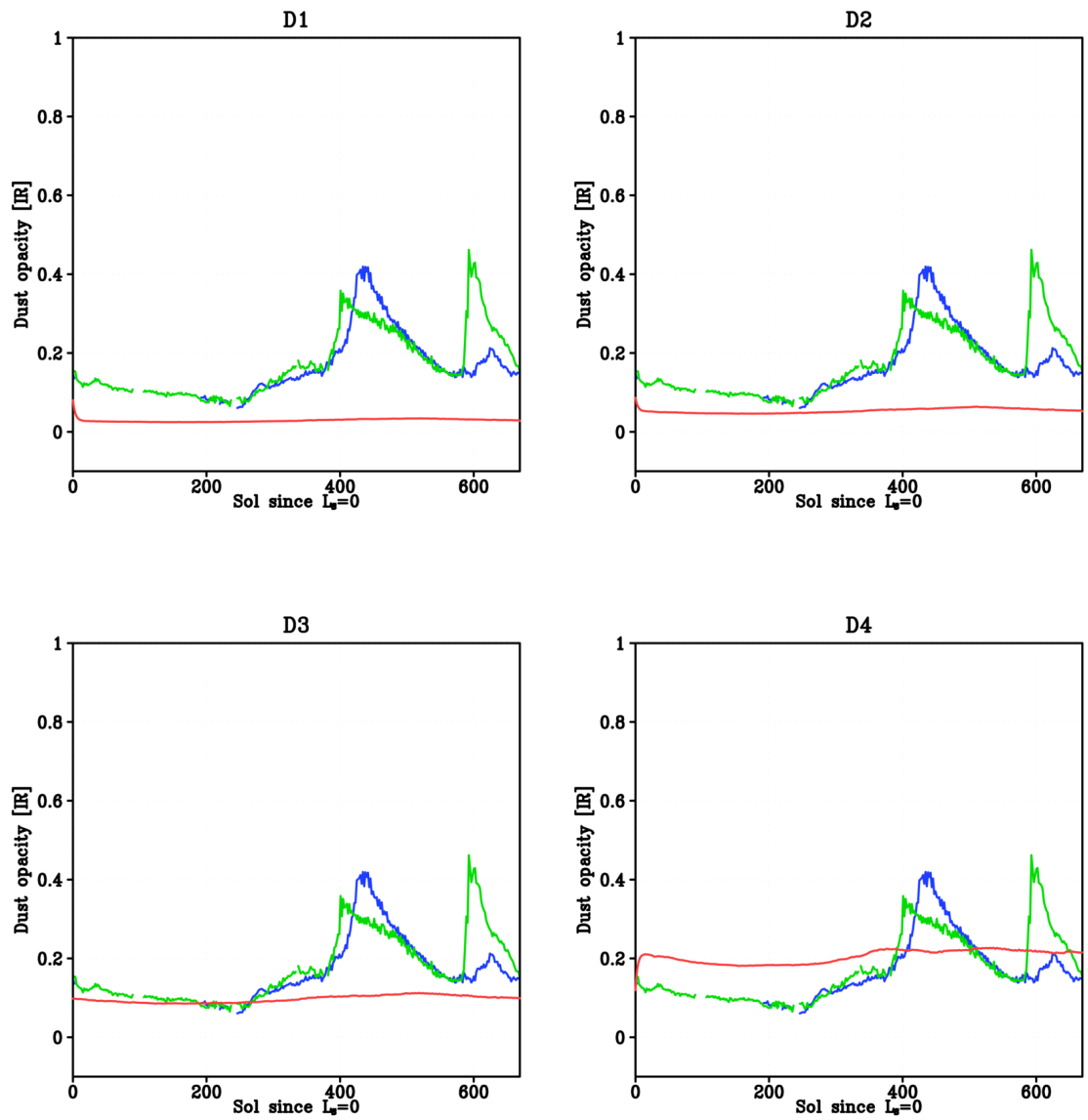


Figure 3.13: Same as Figure 3.1, but dust injection rates in the dust devil scheme are 2×10^{-10} (D1), 5×10^{-10} (D2), 1×10^{-9} (D3) and 2×10^{-9} (D4).

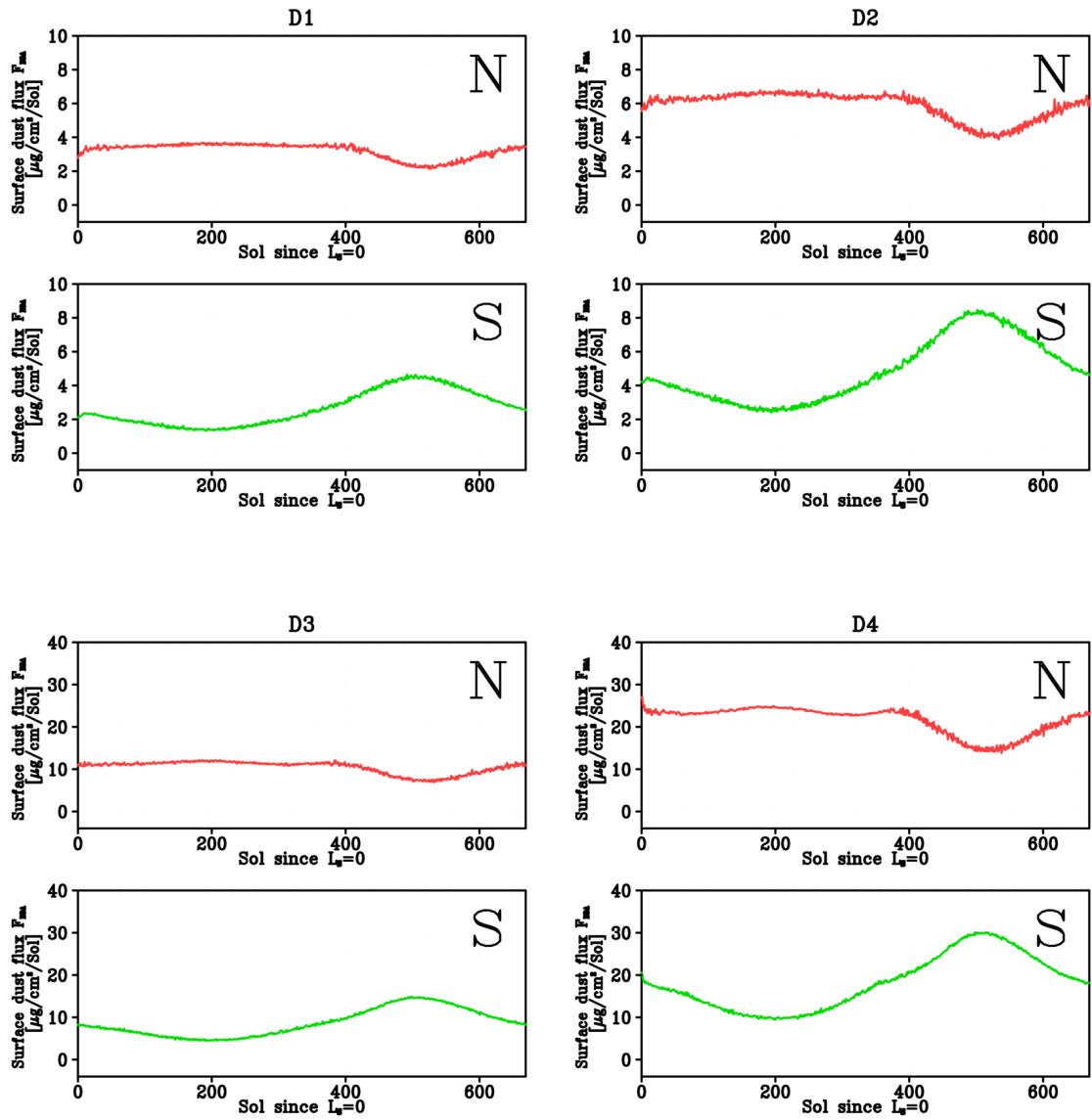


Figure 3.14: Same as Figure 3.5, but dust injection rates are same as Figure 3.13.

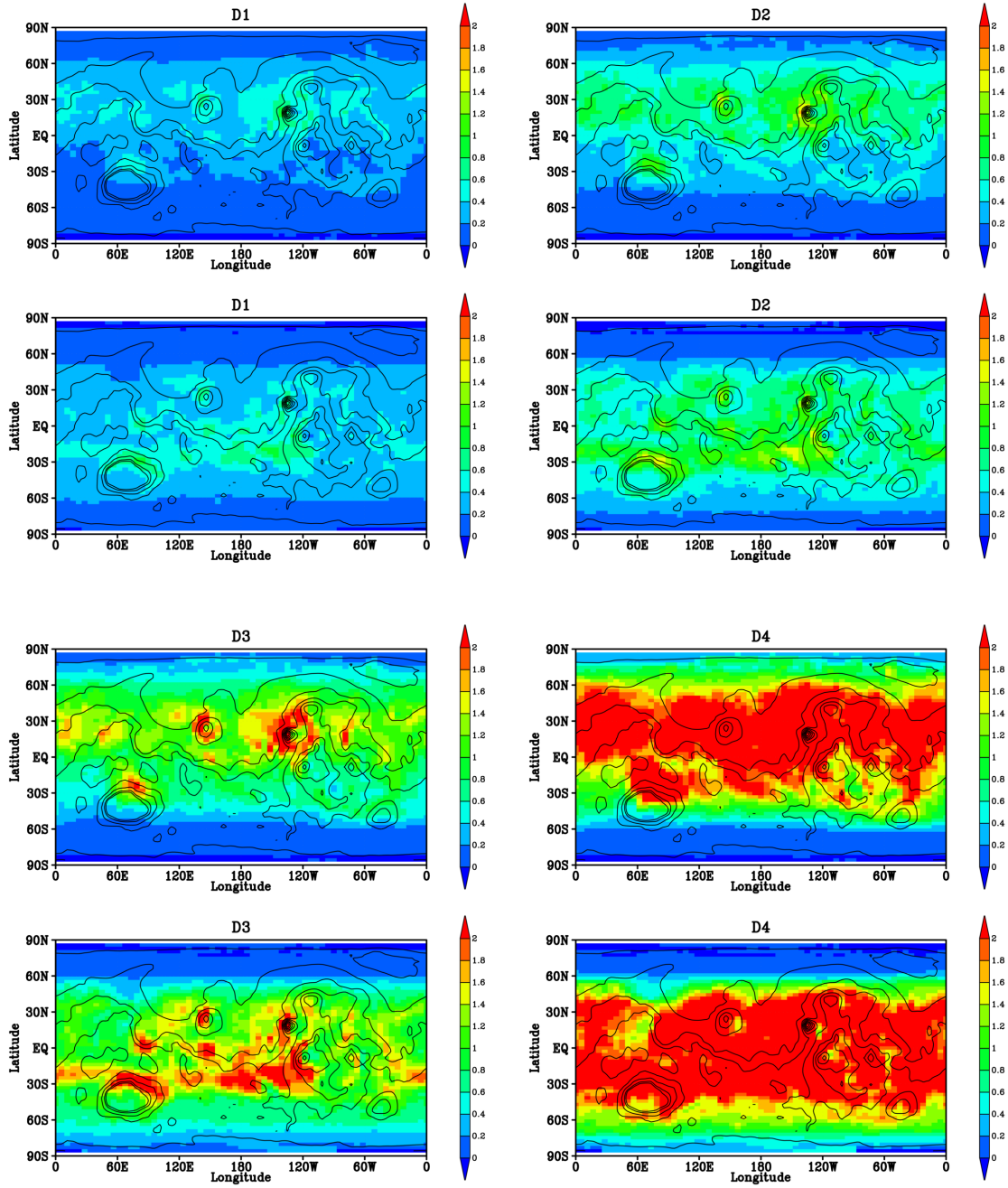


Figure 3.15: Same as Figure 3.9, but dust injection rates are same as Figure 3.13.

3.2.3 Response of dust opacity for couple of two lifting schemes

The sensitivities and features of the two schemes (near-surface wind stress and dust devil) were presented in the previous section. Initially, each dust lifting scheme was independently adopted in our model. According to the experimental evaluations of the individual dust lifting schemes, sensitivity tests were conducted on simulated annual dust opacity. In this section, we incorporate both schemes into our model to realistically simulate dust cycling in the Martian atmosphere. The dust lifting schemes introduced into our MGCM require three free parameters, τ^* , α_{wsl} , and α_{dda} , which collectively govern the seasonal atmospheric dust cycle. Figure 3.16 summarizes the wind stress scheme examined at various seasonal dust opacities. In all experiments, the best-fit dust devil parameter α_{dda} was assumed, while the wind stress parameters τ^* and α_{wsl} were varied. On the basis of the seasonal dust opacity, the results are broadly divisible into three categories. If the threshold of surface wind stress is low, dust lifting occurs every season, and the dust opacity dramatically rises during the northern hemisphere summer. These results are inconsistent with observation. On the other hand, high thresholds preclude realistic seasonal dust opacities because most of the simulated surface wind stresses are then below 0.040 Pa. Although high wind stresses (exceeding 0.040 Pa) were simulated in the model, these were transient and highly localized. Therefore, to properly simulate atmospheric dust cycling, the threshold was ranged from 0.030 ~ 0.040 Pa, and an appropriate injection rate was identified. The given range of stress thresholds is consistent with laboratory estimated thresholds. Note that if the above parameterization was adopted in a different GCM, the same parameters would yield different results, because the predicted near-surface wind stress varies among models. Therefore, tunable parameters by which the model can match observations and results of laboratory experiments are advantageous features. *Kahre et al.* [2006] used the same dust lifting schemes. The lifting efficiency α_{wsl} for the best-fit seasonal opacity was 9×10^{-6} for $\tau^* = 0.0225$ Pa. These parameters are close to those of our study. *Basu et al.* [2004], [2006] simulated seasonal variability of

the temperature which consistent to the past observation, then α_{wsl} was 0.030 ~ 0.060 Pa. In comparison with this study, the range of the threshold is wider due to the different surface dust flux function. They estimated the sub-grid scale wind velocity by using Weibull distribution. This estimation enables that dust lifting occurs even though the surface stress is smaller than the threshold values. This distribution is often employed to evaluate the incidence of wind, however our model does not adopt this distribution. Because some observational unknown parameters are required.

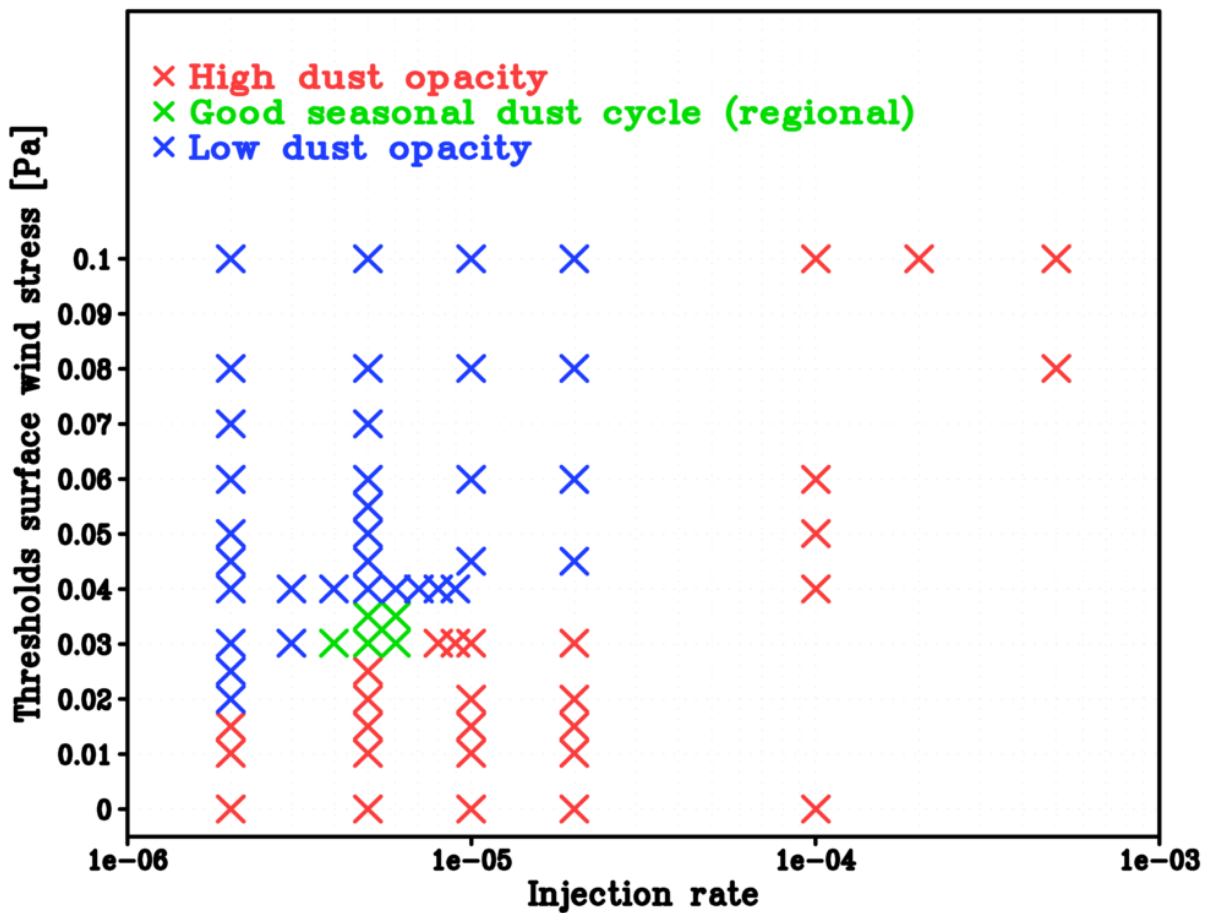


Figure 3.16: A summary of the wind stress scheme examined for various storm behaviors. The dust devil parameter $\alpha_{dda} = 1 \times 10^{-9}$ is used for all experiments.

Chapter 4

Regional dust storm

4.1 Dust opacity modeled by MGCM with both lifting schemes

In the previous chapter, it is shown that the seasonal variation of the simulated dust opacity during southern hemisphere summer is consistent with the observation. In particular, the dust opacity around middle latitude in northern hemisphere is well simulated. Furthermore, the horizontal and temporal development of the dust opacities are similar to the observation. In this chapter, the mechanism of the dust lifting in northern hemisphere during southern hemisphere summer is discussed. Note that the initial conditions and spin-up are same as the sensitivity experiments. We report the results of simulations simultaneously employing both schemes to realize realistic dust cycling in the Martian atmosphere. The following parameters yielded the best-fit simulations of regional dust storms: $\alpha_{wsl} = 5 \times 10^{-6}$, $\tau^* = 0.030$ Pa, and $\alpha_{dda} = 1 \times 10^{-9}$.

4.1.1 Annual dust opacity and temperature structure

Figure 4.1 shows the time series of the simulated dust opacity, along with the TES-derived dust opacity for comparison. During the northern hemisphere summer ($L_S = 0^\circ \sim 180^\circ$), the observed seasonal variations in dust opacity were below 0.2, consistent with the results of our model. In contrast, the MGS-TES data for the southern hemisphere summer ($L_S = 180^\circ \sim 360^\circ$) exhibit two large peaks generated by regional dust storms in MY24 (green) and MY26 (blue). Our model accurately reproduces the seasonal changes in dust opacity caused by dust events. For instance, the model reproduces the observed peak outbreaks in the northern hemisphere, the intensity of dust opacity, and the increasing (or decaying) rate of regional dust storms. The dust is less opaque at the equator than in the northern hemisphere. The dust opacity around 440 Sol ($L_S = 221.4^\circ$) is close to that in MY24, and the peak timing is consistent with the observation. In the late southern summer season around 600 Sol ($L_S = 322.3^\circ$), the model underestimates the dust opacity observed in MY24 and MY26, yielding an opacity below 0.2. In the southern hemisphere, the simulated dust opacity peaks around 500 Sol ($L_S = 260.3^\circ$), whereas the TES-derived dust opacity peaks two times in the same period.

Figure 4.2 plots the seasonal variations in the zonal-mean temperature at 2 hPa. The model properly simulates the temperature profile in the northern hemisphere. In the southern hemisphere, the simulated temperature is underestimated because the predicted dust lifting is smaller than actual dust lifting in the MY24 and MY26 storms. Figure 4.3 shows the zonal-mean temperature in the early southern summer ($L_S = 215^\circ$). The temperature is consistent with the recorded temperature, except in the upper atmosphere, where the assumed dust levels are less than the observed ones. The temperature amplitude, defined as the difference between night and day temperatures, is plotted in Figure 4.4. In the northern hemisphere, the maximum simulated amplitude exceeds 8 K at 0.5 hPa, slightly higher than the observed magnitude (approximately 6 K), although the simulated and observed profiles are similar. In the southern hemisphere, the temperature amplitude is 4 K

in the lower atmosphere (approximately 1 hPa). In this hemisphere, both the simulated amplitude and profile are largely consistent with observation, indicating that our model can evaluate the thermal tide contributions to Martian dust storms.

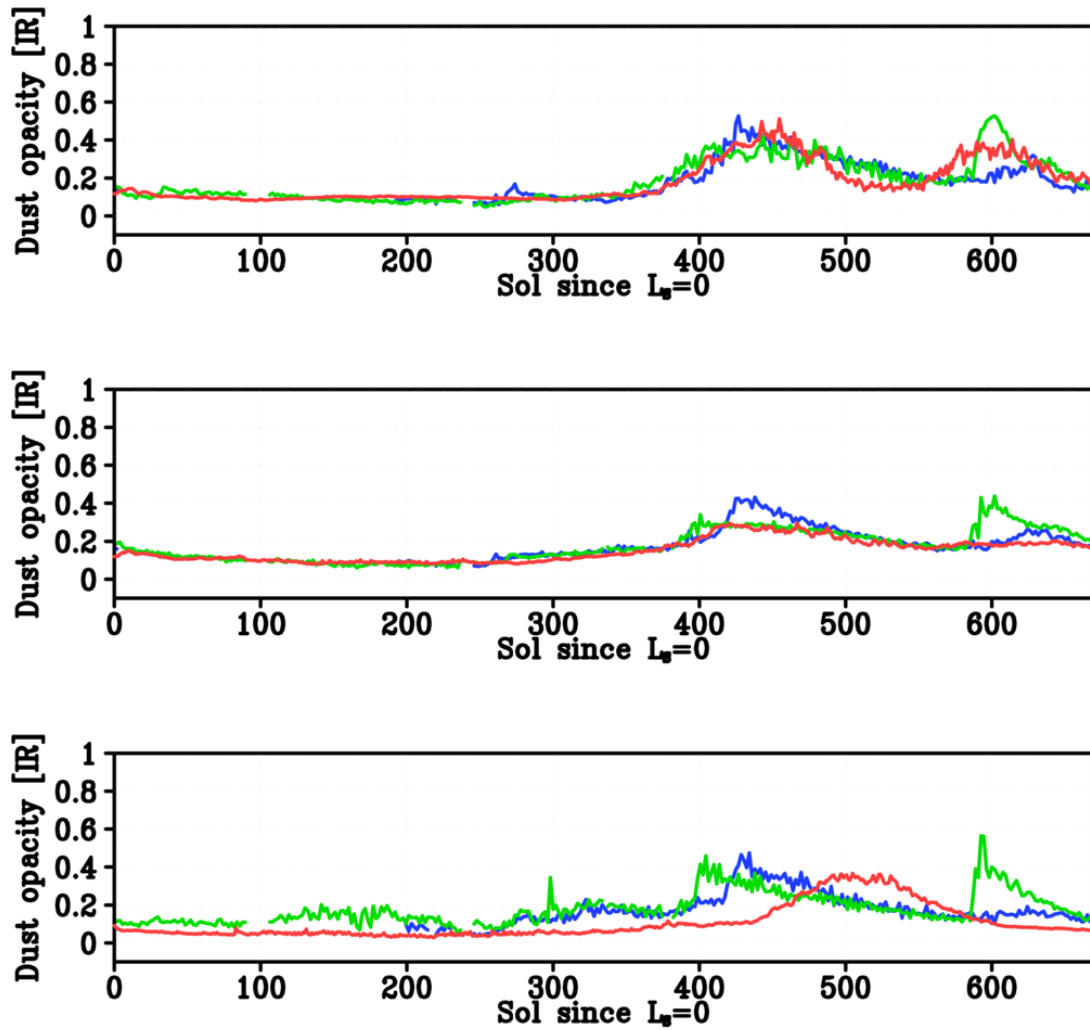


Figure 4.1: Top: Time series of zonal-mean dust opacities adjusted to the 6.1 hPa pressure level for simulation (red), TES-derived from MY24 (green) and MY26 (blue) at 35°N . Middle: Same as Top but equator. Bottom: Same as Top but 35°S .

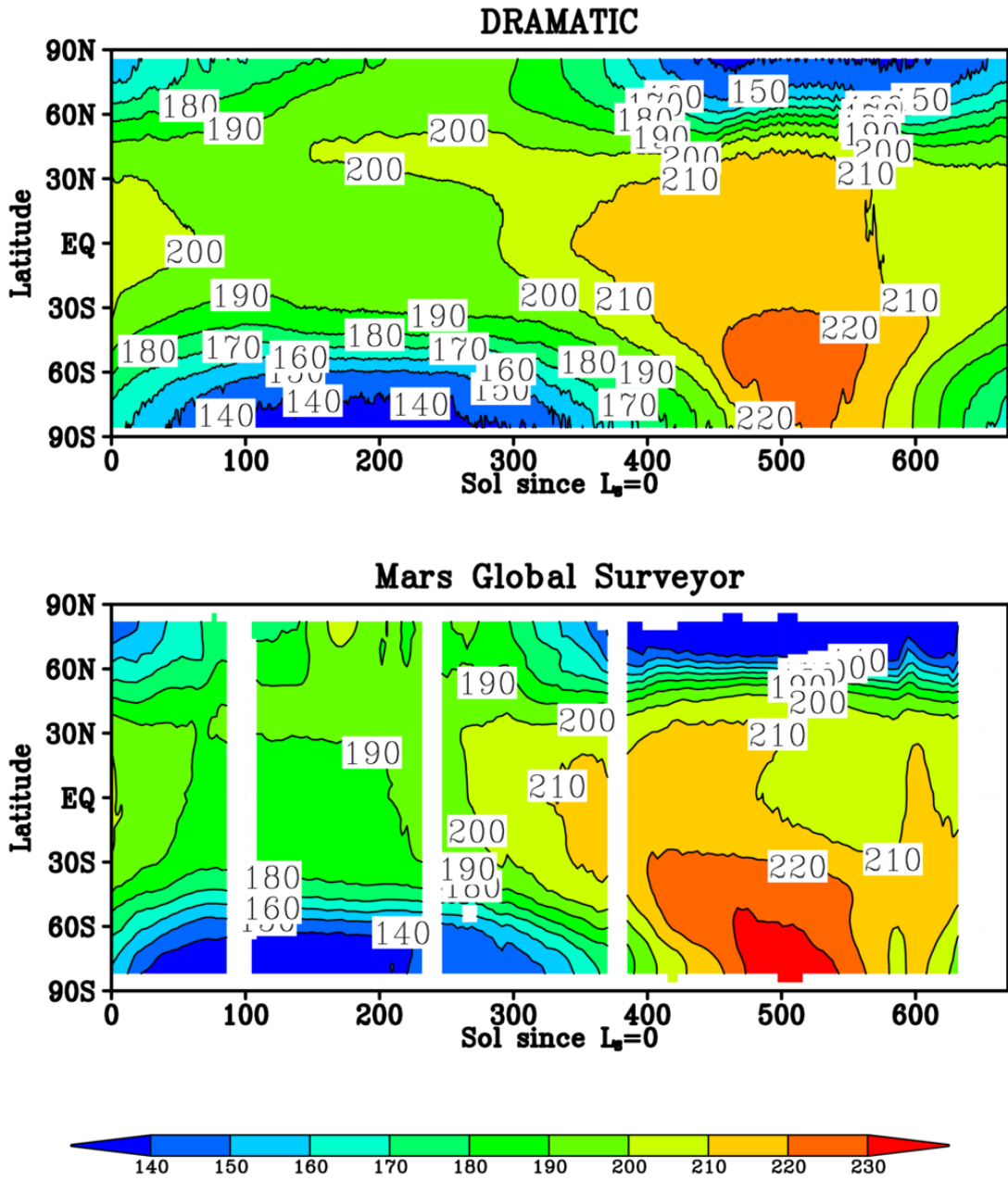


Figure 4.2: Top: Time series of zonal-mean temperature [K] for simulation at 2 hPa. Bottom: Same as Top but TES-derived from MY24.

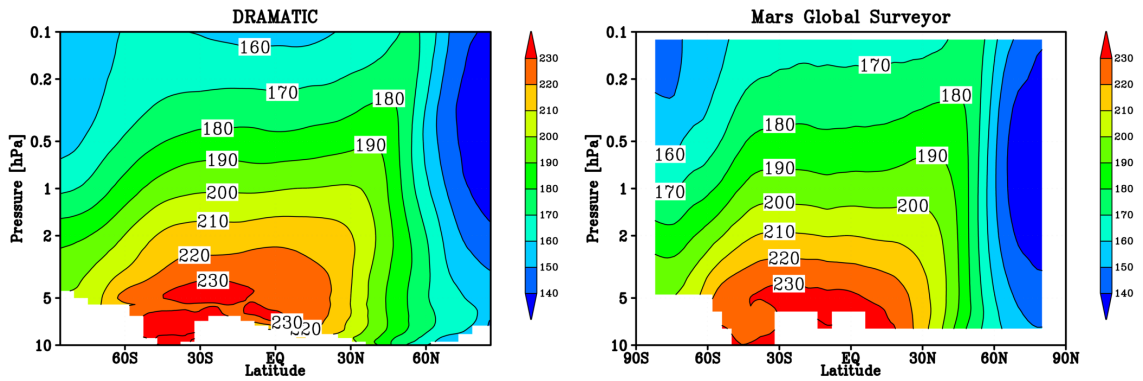


Figure 4.3: Left: Zonal-mean temperature [K] for simulation at $L_S = 215.3^\circ$. Right: TES-derived from MY24 at $L_S = 208^\circ$.

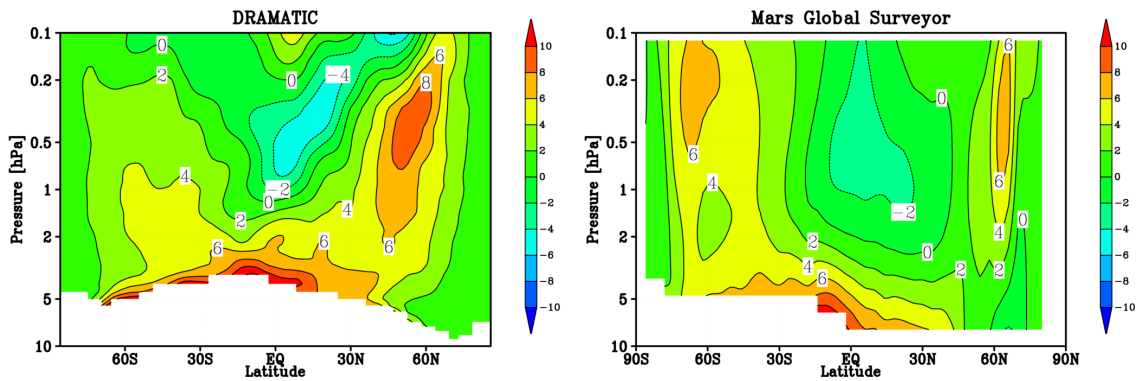


Figure 4.4: Left: Amplitude of day-night temperature [K] for simulation at $L_S = 215.3^\circ$. Right: TES-derived from MY24 at $L_S = 208^\circ$.

4.1.2 Seasonal dust lifting

Figure 4.5 shows the simulated zonal-mean surface dust fluxes throughout one Martian year. Dust lifting chiefly occurs during the southern hemisphere summer, and the two dust lifting parametrizations introduced into the model yield characteristic results. The near-surface wind stress injects dust into the atmosphere between the equator and southern mid-latitudes. In the simulations, dust is raised along the edge of the CO_2 ice covers at

30°S. This result is consistent with past observations, which have revealed the edge of the CO₂ ice cap as a frequent source of dust storms [Cantor *et al.*, 2001]. The northern part of the Hellas basin (located at 30°S) initiated the encircling dust storm of MY25. Strong dust lifting occurs in the same region in this numerical experiment, beginning in the early summer at approximately 350 Sol ($L_S = 167.3^\circ$) and peaking at 500 Sol ($L_S = 260.3^\circ$). This time series is identical to the time series of dust opacity in the southern hemisphere (see bottom of Figure 4.1). Therefore, it appears that the seasonal variation in the dust opacity in the southern hemisphere is chiefly affected by dust lifting events in the Hellas basin. Compared to the near-surface wind, the dust devil scheme exerts a lesser effect on intensity and seasonal variability of dust storms, but plays an important role in supplying background dust.

Figure 4.6 shows the temporal development of the simulated dust opacity. Atmospheric dust is mainly sourced from the mountainous region around 90°W. During the southern summer, the high dust opacity is transported east in an arc-like fashion by the eastward wind. This horizontal path is very similar to the observed path in regional dust storms occurring in the southern summer (see Figure 1.3).

4.2 Simulated dust lifting and near-surface wind

4.2.1 Effects of topography on dust lifting

Figure 4.7 shows the time series of the near-surface wind velocity and the upward dust lifting flux at 50°N. Strong winds (velocity 25 m s^{-1}) are concentrated in the spreading mountainous regions between 60°W and 120°W. Strong lifting occurs between 60°W and 120°W along the northward slopes of the mountainous area. Dust is also sourced from the gentle northward slope between 60°E and 180°E. The strong dust lifting begins around 430 Sol ($L_S = 215.1^\circ$) and suddenly decreases around 480 Sol ($L_S = 247.3^\circ$). This sudden drop is accompanied by a weakening of the near-surface wind. Around 540 Sol ($L_S =$

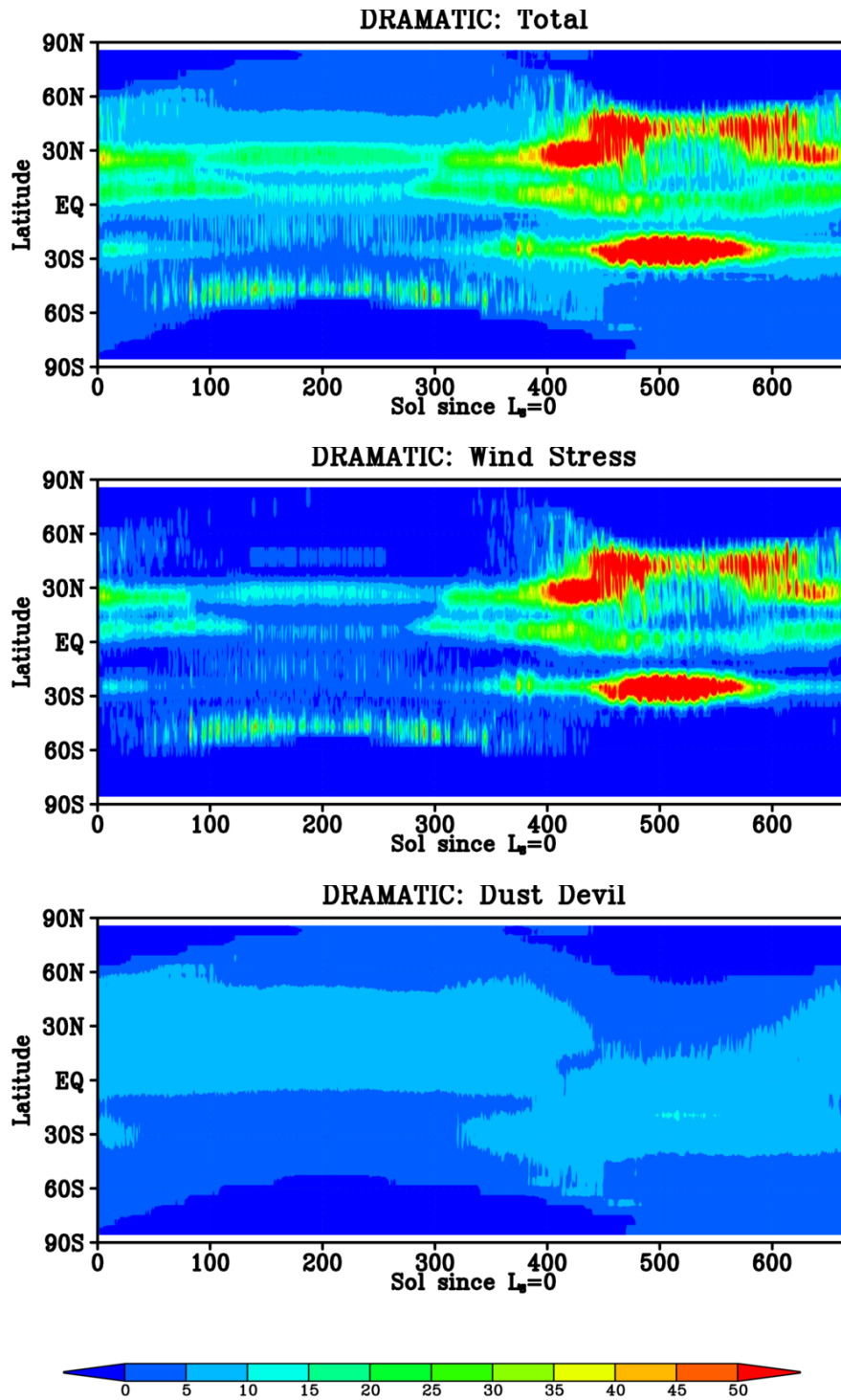


Figure 4.5: Top: Time series of simulated total surface dust flux [$\mu\text{g cm}^{-2} \text{Sol}^{-1}$] averaged zonally. Center: Same as Top but simulated in the wind stress scheme. Bottom: Same as Top but simulated in the dust devil scheme.

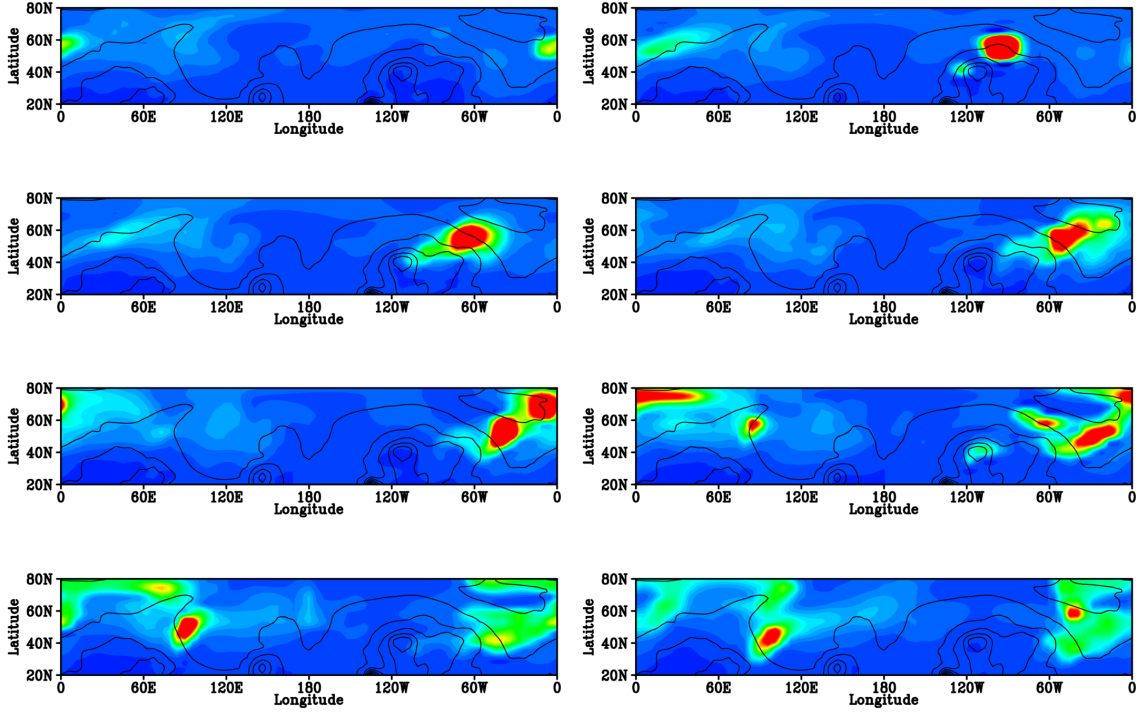


Figure 4.6: Simulated dust opacity during the northern hemisphere winter ($L_S = 215.1^\circ \sim$). The time interval is 6 h. The temporal progression is top to bottom and left to right.

286.0°), the wind velocity is restored to 25 m s^{-1} and dust lifting again strengthens. To investigate the differences between strong and weak dust lifting, the season is divided into three periods: 445 ~ 454 Sol ($L_S = 224.6^\circ \sim 230.4^\circ$), 511 ~ 530 Sol ($L_S = 267.5^\circ \sim 279.7^\circ$), and 585 ~ 604 Sol ($L_S = 313.6^\circ \sim 324.6^\circ$).

Figures 4.9 plots the daytime (local time = 12:00) meridional wind and temperature at 90°E during each period. The near-surface wind exceeds 10 m s^{-1} along the northward downslope. In numerical experiments on flat topography, the near-surface wind was weaker than that on a realistic topography. This trend is consolidated in the strong dust lifting, indicating that dust lifting is strongly enhanced by ascending and descending flows along sloping ground.

4.2.2 Effective wind for dust lifting

Figure 4.10 shows the time series of surface dust flux. These fluxes are averaged from 60°W to 120°W , the latitudes of strongest dust lifting. The time series is plotted at three hourly intervals, and the latitude is that of Figure 4.7. The dust flux suddenly increases around 430 Sol ($L_S = 215.1^{\circ}$). Following its excitation, the dust lifting decreases from 500 Sol ($L_S = 260.3^{\circ}$), and strengthens again around 550 Sol ($L_S = 292.3^{\circ}$).

Figure 4.11 shows the time series of the near-surface wind velocity averaged from 60°W to 120°W . The time interval and latitude are those of Figure 4.10. To estimate the contributions of thermal tides, baroclinic waves, and seasonal variation in dust emission, the total wind velocity was divided into three phases: 1 Sol and fewer (contributed by thermal tides), 5 ~ 7 Sols (contributed by baroclinic waves), and 10 Sols running mean (contributed by seasonal variation). The thermal tide and seasonal variation were both maximized at approximately 11 m s^{-1} . Baroclinic waves exerted a weaker effect, with typical amplitudes below 4 m s^{-1} .

4.3 Thermal tides in the Martian atmosphere

4.3.1 Amplitude of diurnal and semi-diurnal tides

The activity of thermal tide was found to be strongly correlated with the surface dust flux. To investigate the relationship between the surface wind and thermal tide, the amplitude of the thermal tide was estimated from the atmospheric temperature. Figure 4.12 shows the time series of the diurnal and semi-diurnal tide amplitudes. The running mean of the amplitude is 20 Sols. The diurnal tide is strongly excited between 420 Sol and 480 Sol ($L_S = 208.8^{\circ} \sim 247.3^{\circ}$) and between 580 Sol and 620 Sol ($L_S = 310.6^{\circ} \sim 333.6^{\circ}$), reaching 10 K at 0.5 hPa. These excitations are accompanied by stronger surface winds (see Figure 4.15). The semi-diurnal tide shows weaker seasonal variation than the diurnal

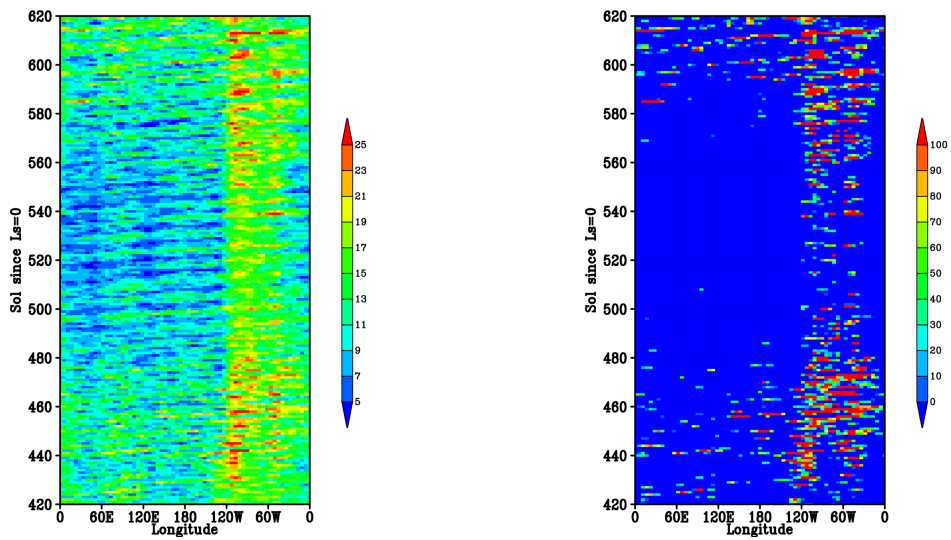


Figure 4.7: Left: Time series of near-surface wind velocity [m s^{-1}] at 50°N . Shown is the daily maximum wind velocity of 10 m above the ground. Right: Time series of upward surface dust flux [$\mu\text{g cm}^{-2} \text{Sol}^{-1}$] at 50°N .

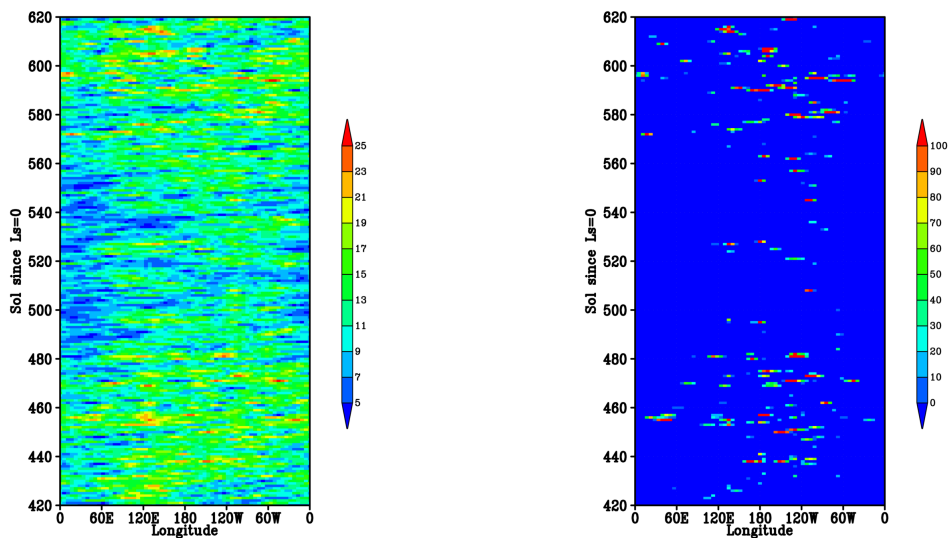


Figure 4.8: Same as Figure 4.7 but height of topography is decrease to 10 % of the original.

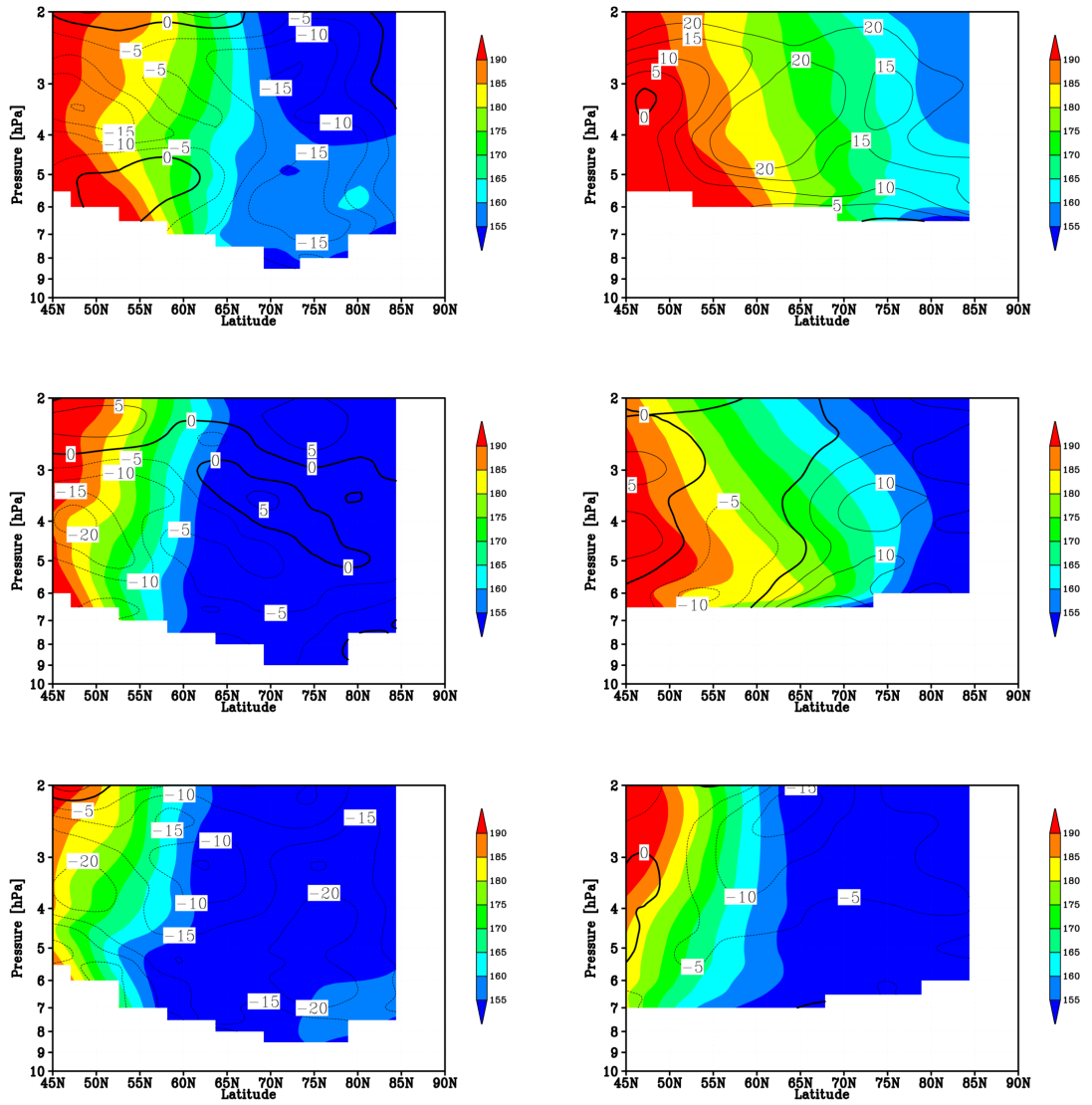


Figure 4.9: Top-Left: Height-latitude sections during the daytime (local time = 12:00) meridional wind [m s^{-1}] (contours) and temperature [K] (shaded) at 90°W , averaged between 445 Sol and 454 Sol ($L_S = 224.6^\circ \sim 230.4^\circ$). Northward (southward) winds are depicted as positive (negative). Top-Right: Same as Top-Left but evaluated on a topography compressed by 10 %. Middle-Left: Same as Top-Left but averaged between 511 Sol and 530 Sol ($L_S = 267.5^\circ \sim 279.7^\circ$). Middle-Right: Same as Top-Right but averaged between 511 Sol and 530 Sol ($L_S = 267.5^\circ \sim 279.7^\circ$). Bottom-Left Same as Top-Left but averaged between 585 Sol and 604 Sol ($L_S = 313.6^\circ \sim 324.6^\circ$). Bottom-Right Same as Top-Right but averaged between 585 Sol and 604 Sol ($L_S = 313.6^\circ \sim 324.6^\circ$).

one, and its amplitude is below 4 K. This result suggests that the diurnal tide adds sufficient strength to the surface wind to enable dust lifting from the ground.

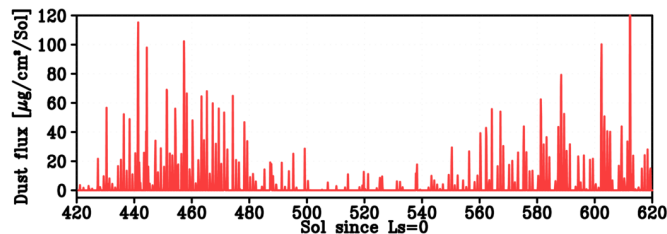


Figure 4.10: Time series of upward surface dust flux [$\mu\text{g cm}^{-2} \text{Sol}^{-1}$] at 50°N . The flux is averaged between 60°W and 120°W .

4.3.2 Heating source of tides

Thermal tides must be maintained by a source. To clarify the wave activity, the atmospheric heating rates averaged over each day are plotted in Figure 4.13. On Mars, the floating dust and CO_2 atmosphere are directly heated by the solar radiation, and impart their heat to the atmosphere. During periods of strong diurnal tide, the rate of dust heating (up to 10 K Sol^{-1}) exceeds the rate of CO_2 heating. Therefore, the thermal tide is chiefly driven by the airborne dust heated by the solar radiation. The profiles of the diurnal and semi-diurnal tides are plotted in Figures 4.14. Between 445 Sol and 454 Sol ($L_S = 224.6^\circ \sim 230.4^\circ$), the amplitude of the diurnal tide is maximized at 8 K around 50°N . Between 511 Sol and 530 Sol ($L_S = 267.5^\circ \sim 279.7^\circ$), the diurnal tide is not clearly evaluated in the northern hemisphere. Between 585 Sol and 604 Sol ($L_S = 313.6^\circ \sim 324.6^\circ$), the maximum amplitude (7 K) again occurs around 50°N . This result shows that, during periods of strong diurnal tide excitation, the tide is amplified at latitudes of strong dust lifting.

Figure 4.15, 4.16 and 4.17 show the phase of the diurnal and semi-diurnal tides. The

vertical wavelength of semi-diurnal tide is estimated more than 75 km. The vertical wavelength of diurnal tide can not be estimated and the wavelength is shorter than the semi-diurnal tide. The vertical heating rate reaches to 8 K Sol^{-1} but the rate is less than 2 K Sol^{-1} when the dust lifting is weak between 511 Sol and 530 Sol ($L_S = 267.5^\circ \sim 279.7^\circ$).

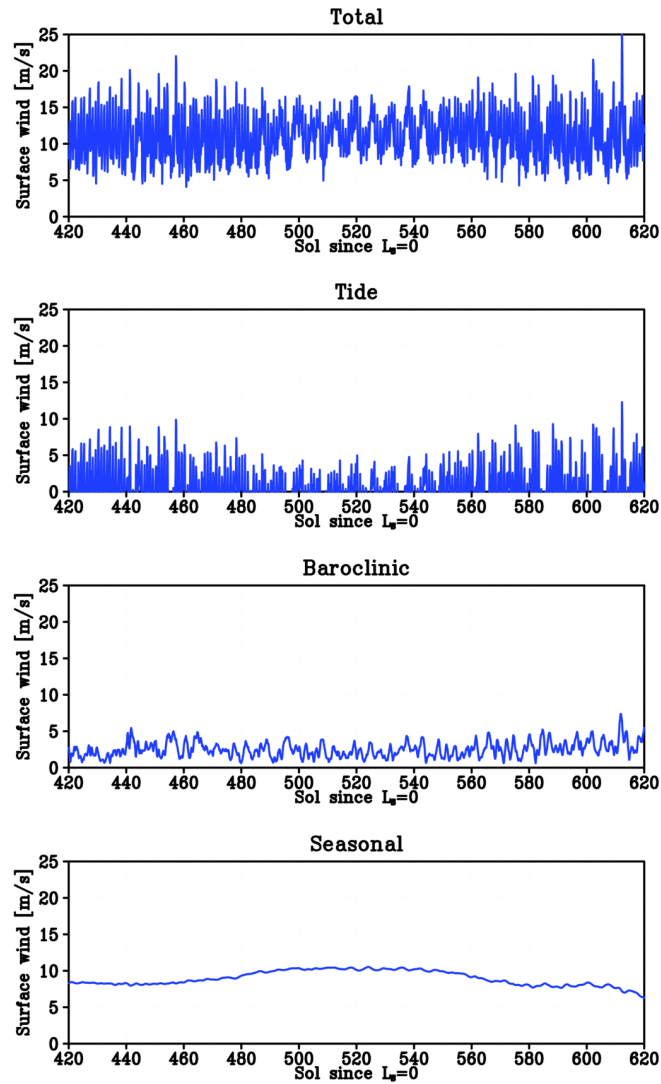


Figure 4.11: Top: Time series of near-surface wind velocity [m s^{-1}]. Each figure shows the amplitude of total wind velocity, thermal tide ($\sim 1 \text{ Sol}$), baroclinic wave ($5\sim 7 \text{ Sols}$), and seasonal variation (10 Sols running mean).

4.4 Reduction of surface dust lifting between 480 Sol and 550 Sol

The dust lifted from the surface is heated by solar radiation, and the warmed up atmosphere drives the thermal tide. In the previous section, the tides were found to effectively accelerate the surface wind. This interaction among the dust, near-surface wind, and thermal tide suggests a positive feedback effect for dust lifting. However, according to Figure 4.10, dust lifting suddenly decreases between 480 Sol and 550 Sol ($L_S = 247.3^\circ \sim 292.3^\circ$). This section discusses the cause of this reduction.

4.4.1 Gravitational sedimentation of dust

Since the sedimentation velocity depends on the air temperature, it is suggested to show seasonal variability. If the sedimentation velocity dramatically fluctuates during the northern hemisphere winter, it presumably weakens (or strengthens) the thermal tide maintained by dust heating. The sedimentation velocity of the dust in the atmosphere is shown in Figure 4.18. We find that the seasonal variation is relatively small. The time scale of the dust sedimentation was evaluated from the velocity and is shown in Figure 4.19. Dust sedimentation occurs over longer time scales than the daily heating time scale. This implies that the removal of the floating dust from the atmosphere by gravitational sedimentation does not significantly affect the seasonal variation in the tides. Therefore, the decrement of tidal activity caused by gravitational sedimentation of the floating dust cannot entirely account for the reduction of dust lifting between 480 Sol and 550 Sol.

4.4.2 Ground covered with CO₂ ice

Figure 4.20 shows how the density of the CO₂ ice cap located at 50°N changes over time. The density is averaged from 60°W to 120°W, the regions of strong dust lifting in

the northern hemisphere winter. The CO₂ ice cap begins to form at 476 Sol ($L_S = 244.7^\circ$) and completely disappears at 596 Sol ($L_S = 320.0^\circ$). This temporal progress of the CO₂ ice cap is consistent with the variation in surface dust lifting (see Figure 4.10). Therefore, it appears that dust lifting activity is reduced by ground coverage with the CO₂ ice cap.

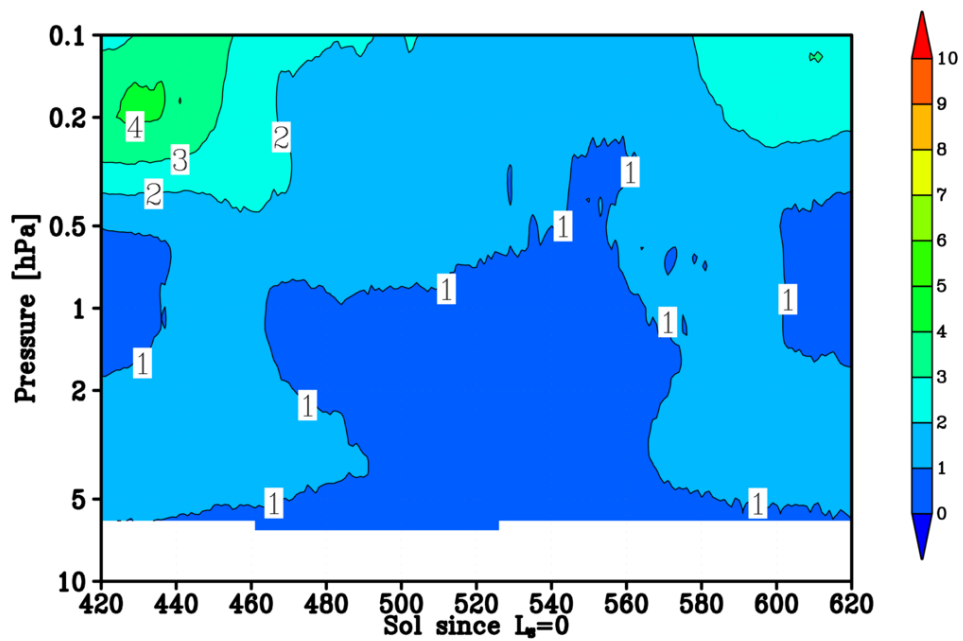
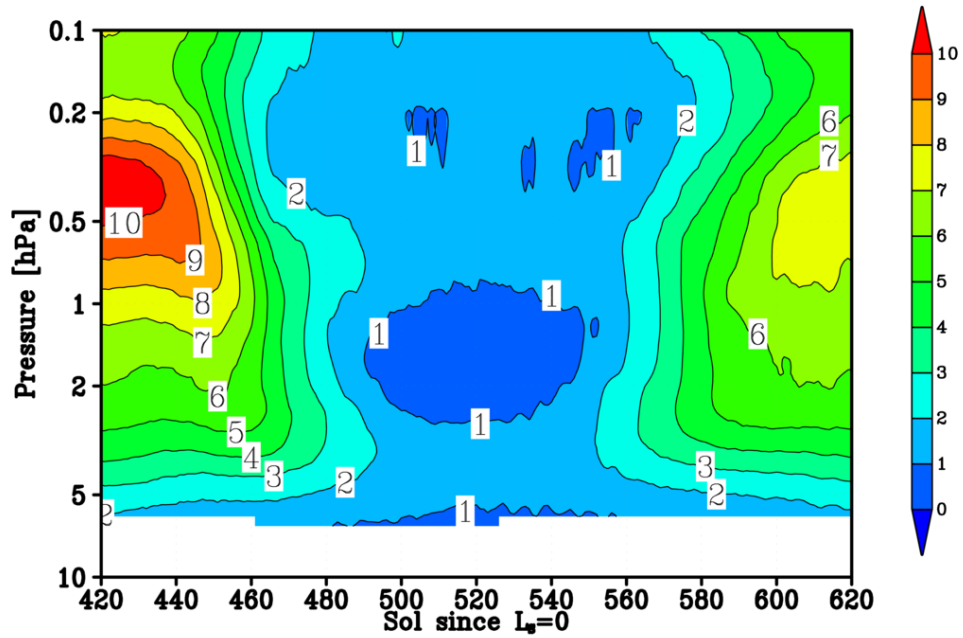


Figure 4.12: Top: Time series of diurnal tidal amplitude [K] calculated from the atmospheric temperature. The tide is calculated every 20 Sols. Bottom: Same as Top but showing the semi-diurnal tidal amplitude.

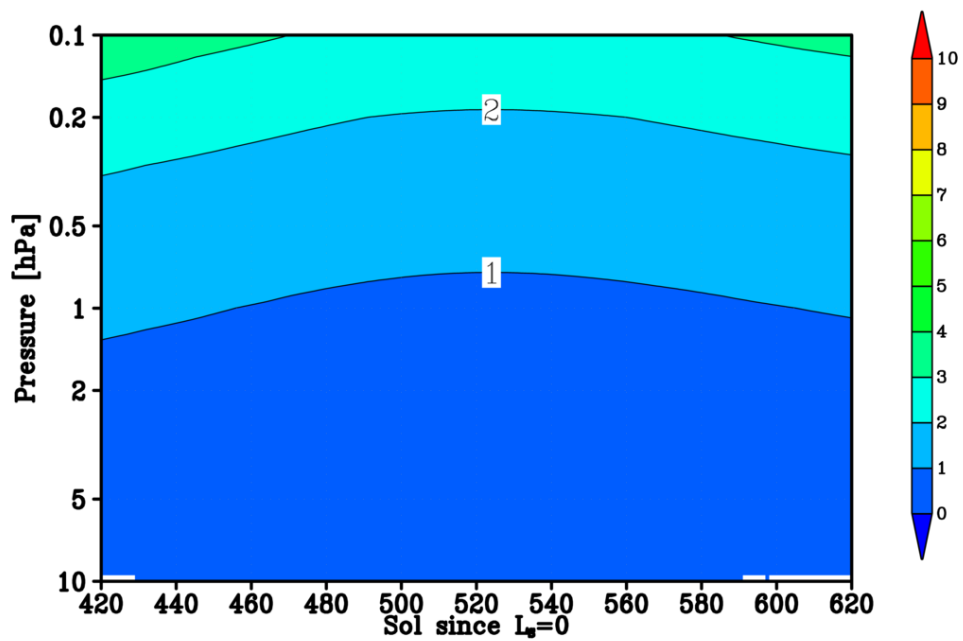
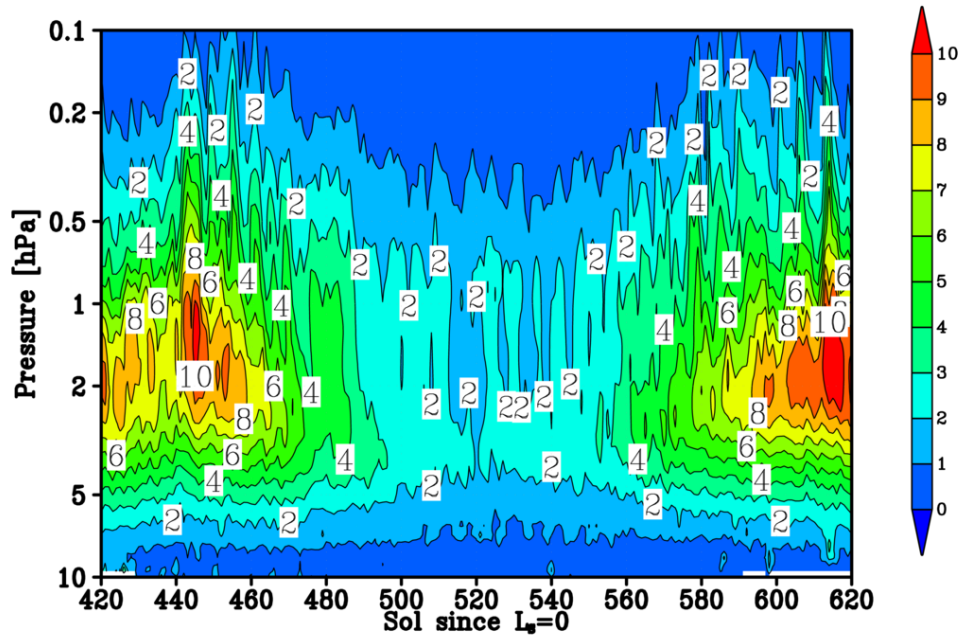


Figure 4.13: Top: Time series of heating rate [K Sol⁻¹] due to dust absorbing at solar wavelengths. Shown are the average daily heating rates. Bottom: Same as Top but due to heating of atmospheric CO₂.

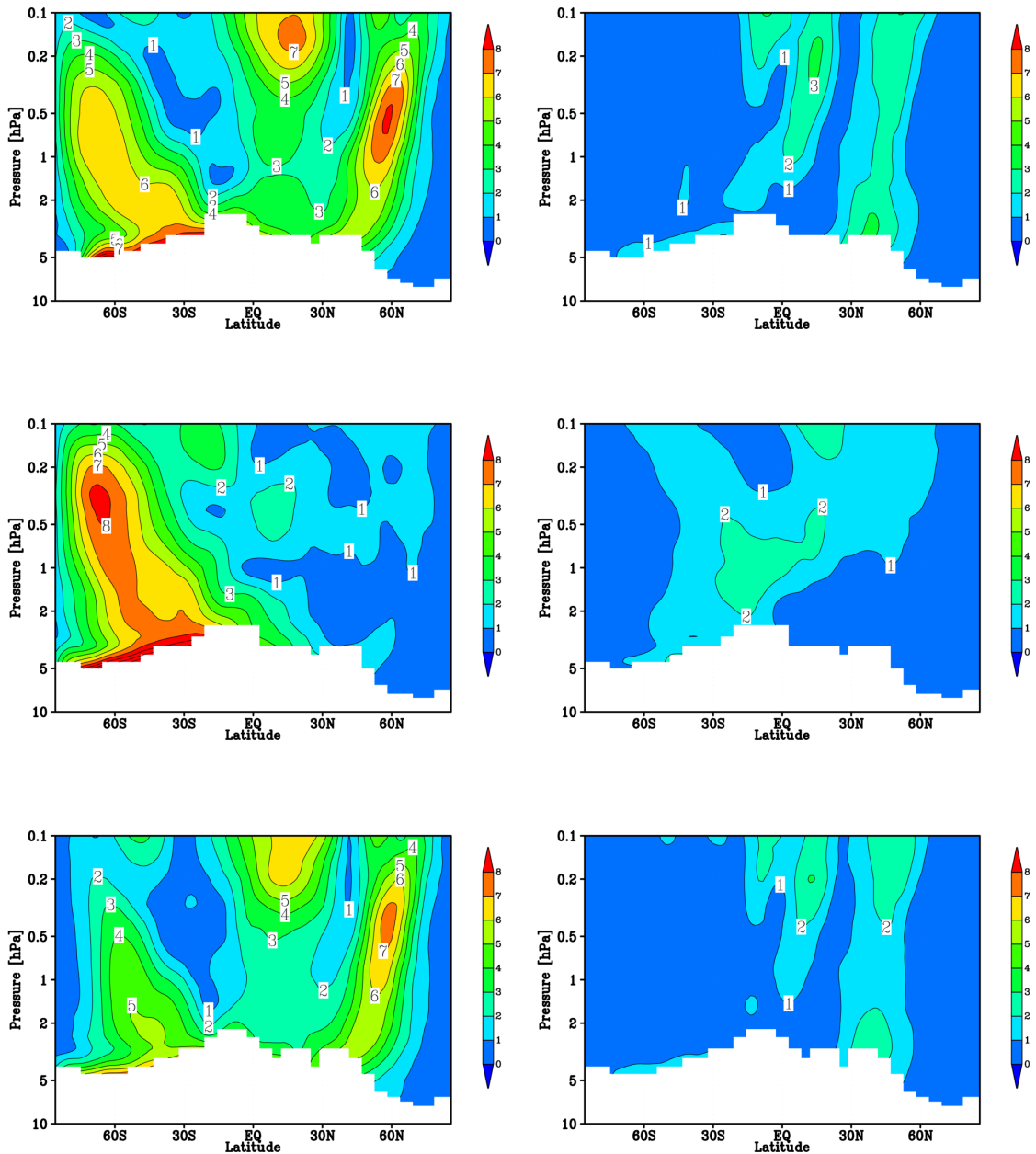


Figure 4.14: Top-Left: Height-latitude sections of diurnal tidal amplitude [K]. The amplitude is calculated from temperatures recorded between 445 Sol and 454 Sol ($L_S = 224.6^\circ \sim 230.4^\circ$). Top-Right: Same as Top but showing the semi-diurnal tidal amplitude. Middle-Left: Same as Top-Left but calculated from temperatures recorded between 511 Sol and 530 Sol ($L_S = 267.5^\circ \sim 279.7^\circ$). Middle-Right: Same as Top-Right but calculated from temperatures recorded between 511 Sol and 530 Sol ($L_S = 267.5^\circ \sim 279.7^\circ$). Bottom-Left: Same as Top-Left but calculated from temperatures recorded between 585 Sol and 604 Sol ($L_S = 313.6^\circ \sim 324.6^\circ$). Bottom-Right: Same as Top-Right but calculated from temperatures recorded between 585 Sol and 604 Sol ($L_S = 313.6^\circ \sim 324.6^\circ$).

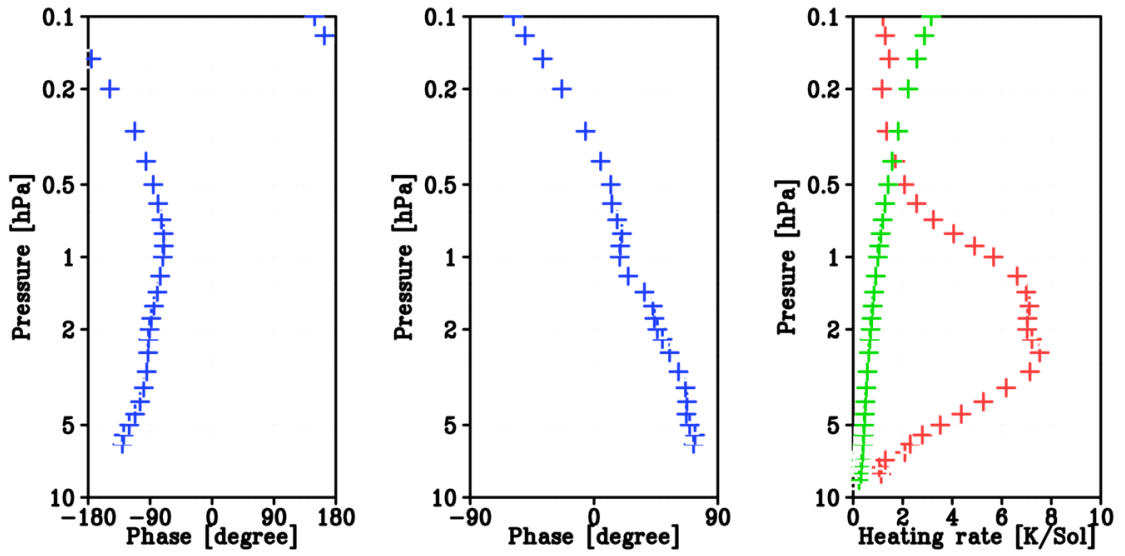


Figure 4.15: Left: Phase angle of diurnal tide at latitude 50°N. The phase is calculated at temperatures recorded during the period of Figure 4.9(Top). Center: Same as Left but showing phase angles of the semi-diurnal tide. Right: Heating rate [K Sol⁻¹]. Rates of dust and CO₂ heating are indicated in red and green, respectively, during the period of Figure 4.9(Top).

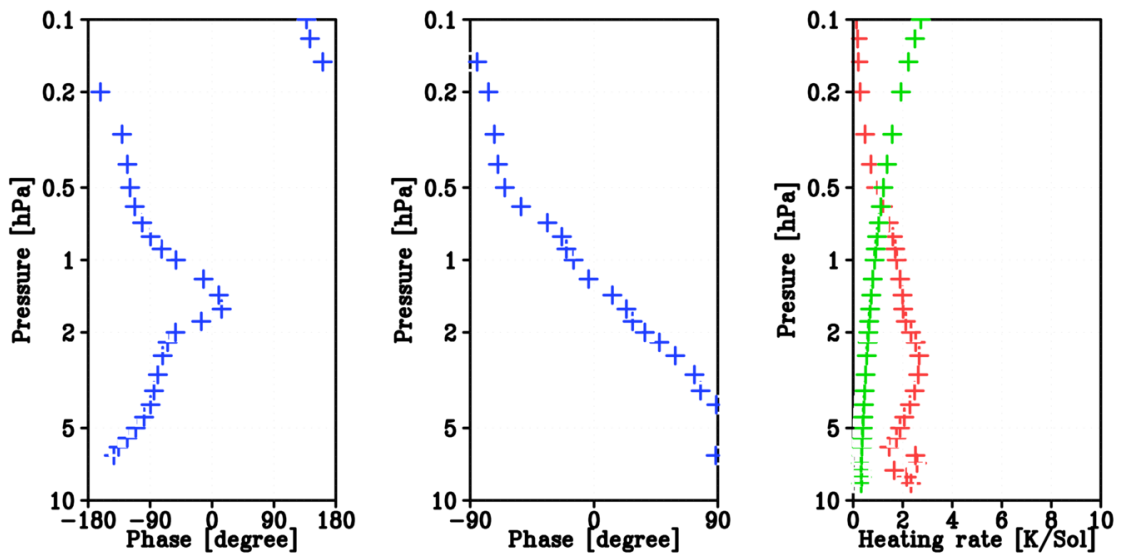


Figure 4.16: Same as Figure 4.19 but calculated with the same period of Figure 4.9(Middle).

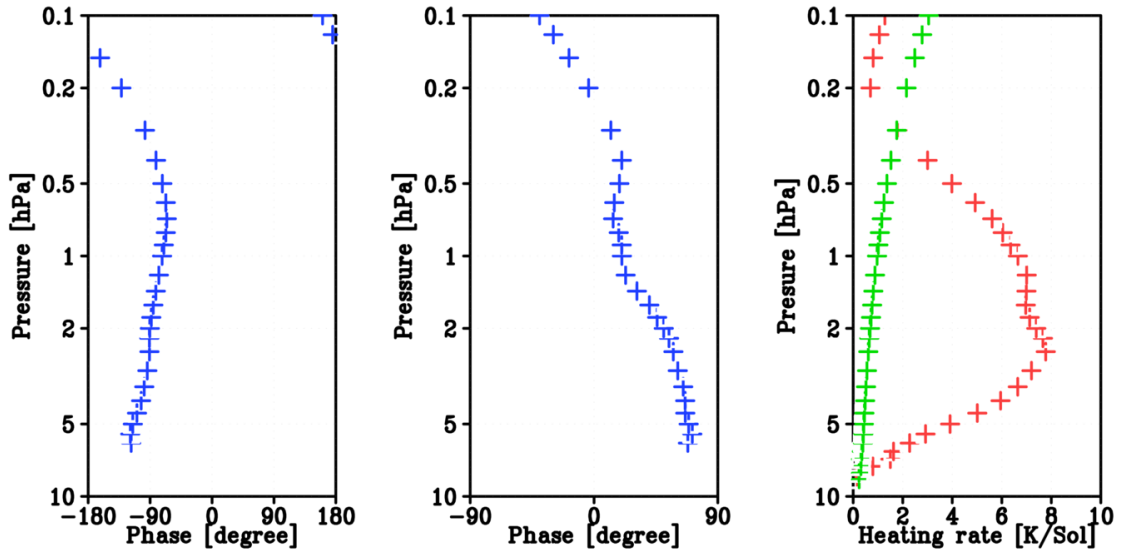


Figure 4.17: Same as Figure 4.19 but calculated with the same period of Figure 4.9(Bottom).

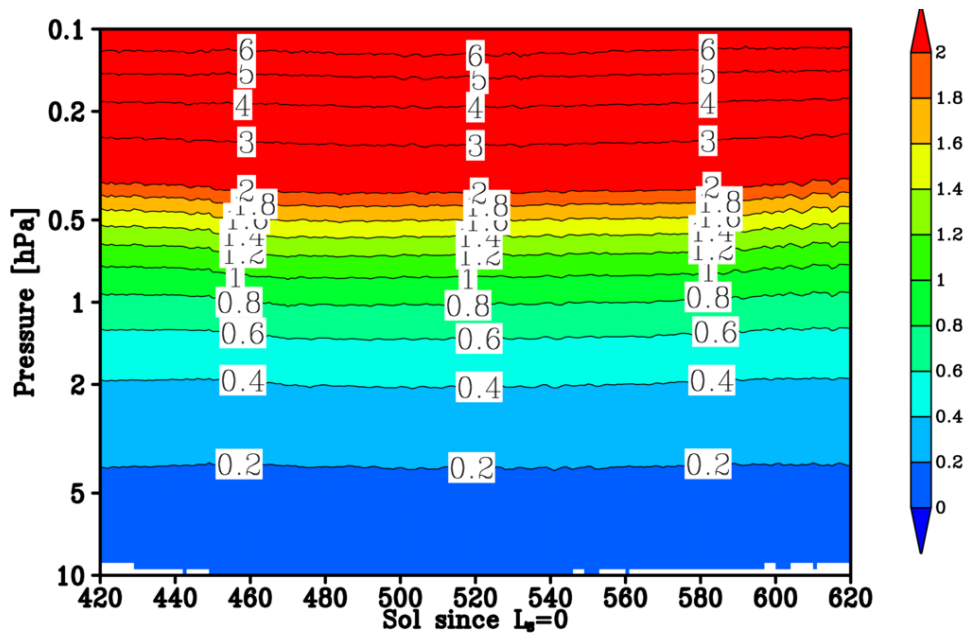


Figure 4.18: Time series of zonal-mean velocity [cm s^{-1}] at 50°N for gravity sedimentation of dust particles.

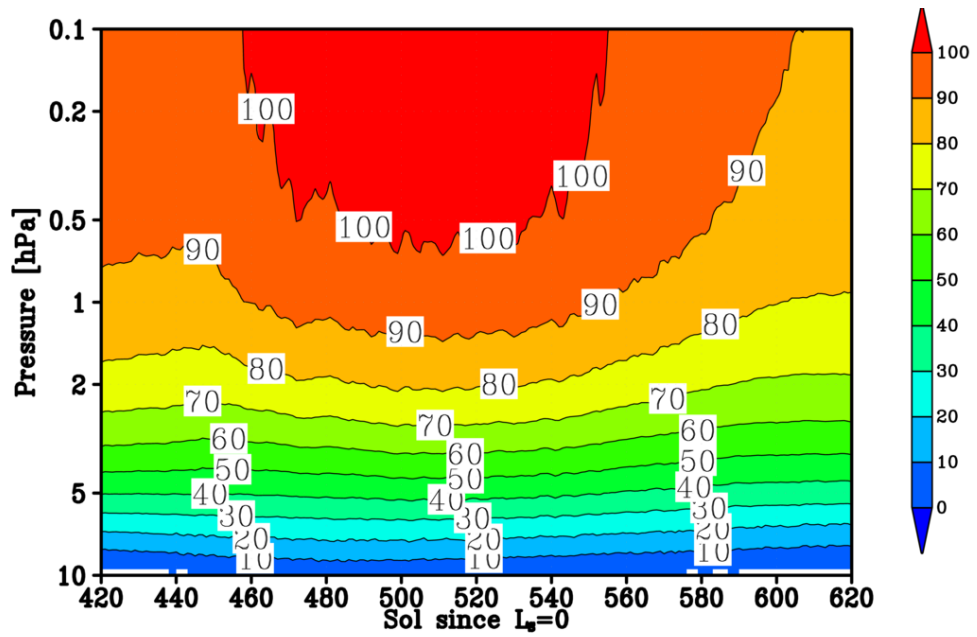


Figure 4.19: Time series of zonal-mean time scale [Sol] at 50°N for gravity sedimentation of dust particles. The time scale is calculated by using the velocity in Figure 4.22, assuming that the velocity does not change seasonally.

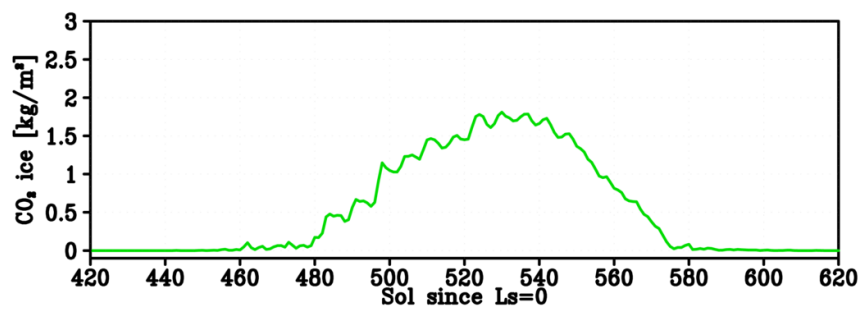


Figure 4.20: Time series of CO_2 [kg m^{-2}] averaged between 60°W and 120°W in 50°N.

Chapter 5

Global dust storms

This chapter discusses the temporal development of the global dust storm. The environments that induce global dust storms are clarified in an encircling dust storm experiment. The results are compared with those of the regional dust storm study analyzed in Chapter 4.

5.1 Experimental design for global dust storm

The global dust storm of MY25 was joined by multiple synoptic-scale dust storms that interfered with each other [Smith *et al.*, 2001]. We suggest that encircling dust storms are generated when several dust storms erupt in quick succession; that is, if a certain dust storm incites the birth of another dust storm, the initial dust storm is assumed as the trigger of the global dust storm. On the basis of this assumption, we designed an experiment for global dust storms.

In evaluating the above idea, we introduced an additional upward dust flux on the Martian surface, specifically, in the northern part of the Hellas basin (see Figure 5.1), where the global dust storm originated in MY25. On the basis of this event, the period of the additional dust injection was determined as $L_S = 188.0^\circ$ to $L_S = 191.0^\circ$ (see Figure 5.2).

The flux is given by

$$F_{fcg} = \begin{cases} F_{fcg0} \times \cos [\pi (L_s - 188.0) / 6] & 188.0 \leq L_s \leq 191.0, \\ 0 & 0 \leq L_s < 188.0, 191.0 < L_s < 360.0, \end{cases} \quad (5.1)$$

where $F_{fcg0} = 2.26 \times 10^{-7}$ [$\text{kg m}^{-2} \text{s}^{-1}$]. This value was estimated from the mass transported during regional dust storms [Cantor *et al.*, 2001]. The total upward surface dust flux is calculated as

$$F_{dust} = F_{wsl} + F_{dda} + F_{fcg}. \quad (5.2)$$

The parameters for the near-surface wind stress and the dust devil schemes were those used in the regional dust storm experiment discussed in chapter 4.

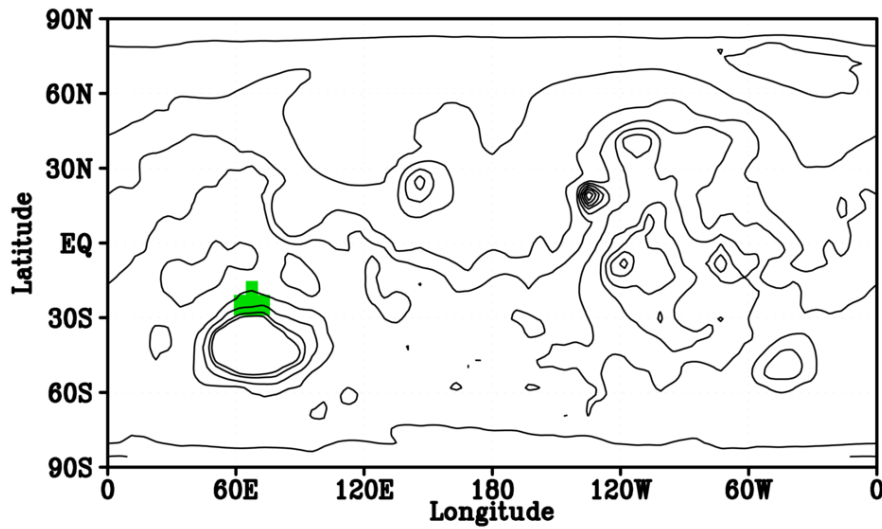


Figure 5.1: Latitude-longitude distribution of additional surface dust flux [$\text{kg m}^{-2} \text{s}^{-1}$]. The flux is indicated as green shade and given uniformly.

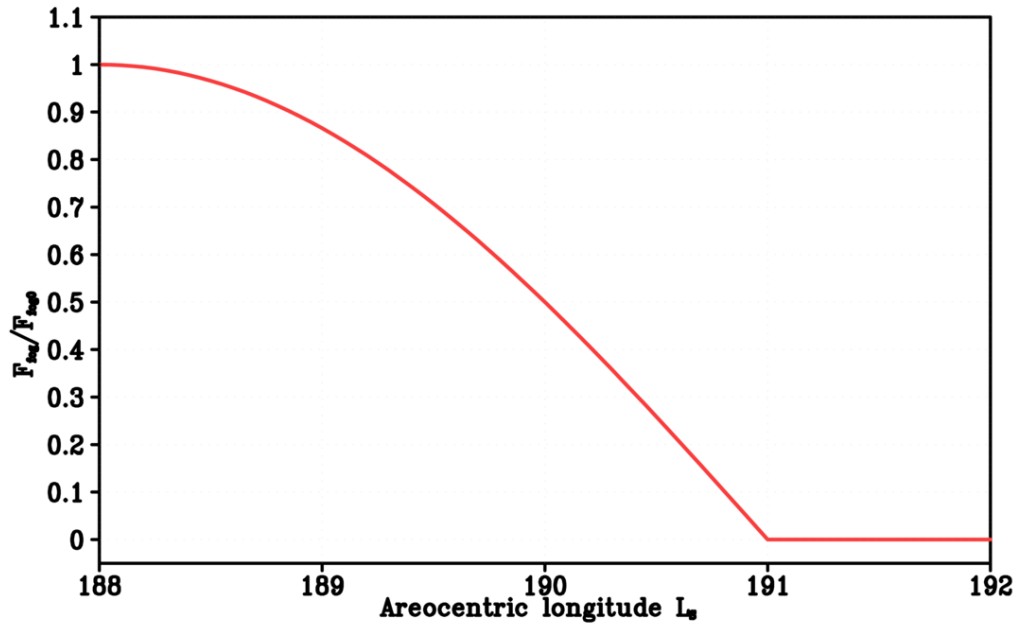


Figure 5.2: Time series of upward surface dust flux forced around the northern part of the Hellas basin. The value is calculated as F_{dust} / F_{dust0} .

5.2 Simulated global dust storm

5.2.1 Temporal development of dust opacity

The temporal development of the simulated dust opacity yielded by this experiment is shown in Figure 5.3. When the surface dust flux around the northern Hellas basin was forced upward, the dust opacity was increased around the mountainous area in the northern hemisphere. These areas of high dust opacity spread across the Hellas basin region and into the mountainous area around 120°W in the northern hemisphere. Later, the two areas of high dust opacity zonally expanded and united.

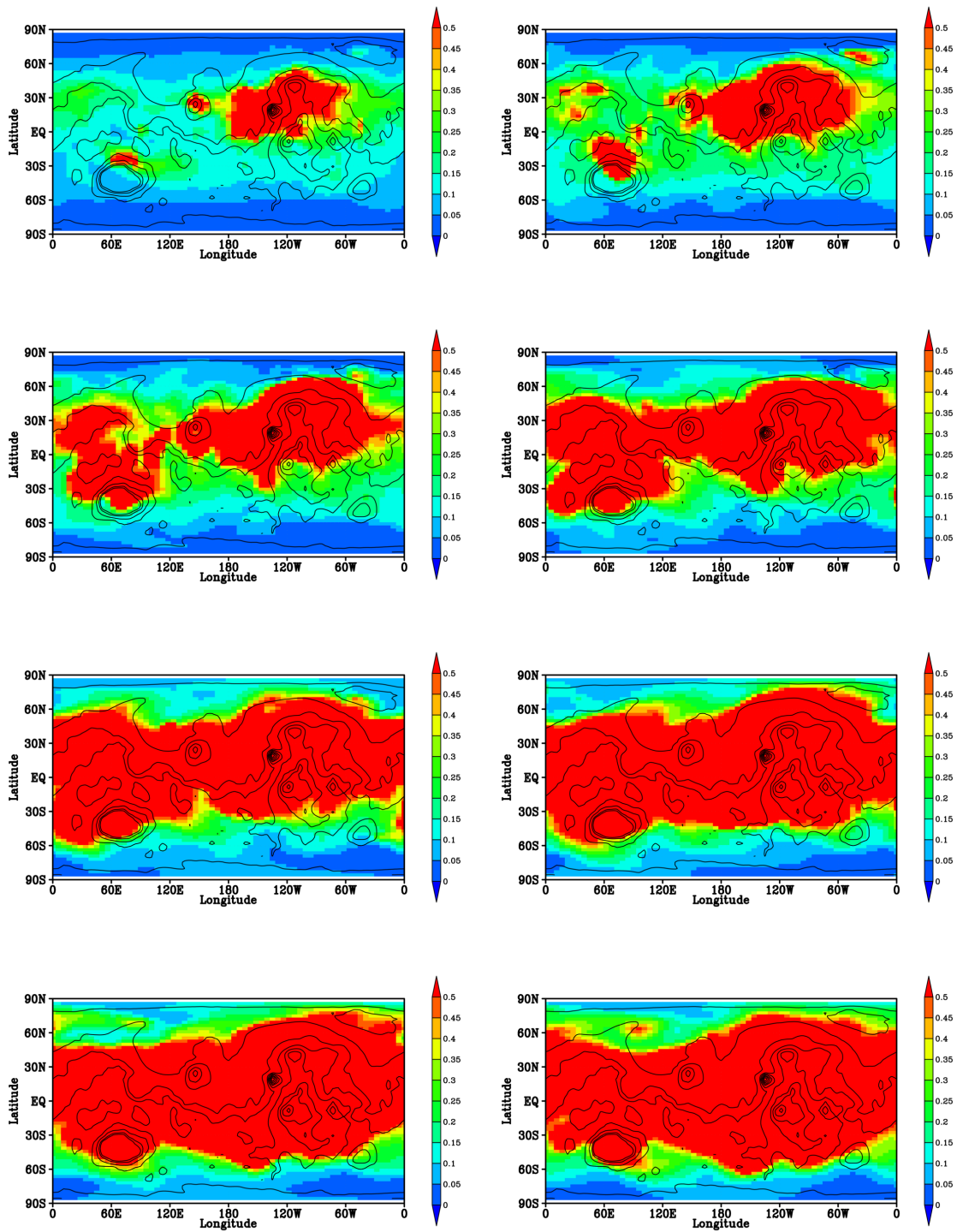


Figure 5.3: Latitude-longitude distribution of simulated dust opacity in the global dust storm experiment. The solid lines indicate the topography. The season is $L_S = 190.4^\circ \sim 194.6^\circ$.

5.2.2 Dust lifting

Figure 5.4 shows the distributions of upward surface dust flux. In the near-surface wind stress scheme, dust lifting is increased in specific regions, including the northwest Hellas basin, where dust lifting was absent in the regional dust storm experiment. High dust activity occurs at 30°N where the strong dust lifting spreads across zones. According to the sensitivity experiments, the mountainous region around 150°W is a frequent source of atmospheric dust in our model. The dust injections around this region are stronger in the global than in the regional dust storm experiment. On the other hand, the flux contributed by the dust devil scheme is less spatially variable than in the regional dust storm experiment (not shown in Figure 5.4).

The surface pressure time series for a wave number of 1 (hereafter denoted as WN1) are shown in Figures 5.5. In the global dust storm experiment, the amplitude of WN1 surface pressure reaches 0.3 hPa, larger than in the regional dust storm. Whereas the phase moved westward in the regional experiment, it moves longitudinally in the global experiment. The relationship between the surface pressure and surface wind is plotted in Figures 5.6. The wind velocity is strengthened in regions of overlap between the trough of the WN1 surface pressure and the slope around the mountainous areas. The wind velocity reaches 35 m s^{-1} around 120°W, much higher than in the regional dust storm experiment (25 m s^{-1}). The WN1 surface pressure moves westward and its period is one Martian day. These results suggest that the diurnal tide accelerates the surface wind, as observed in the regional dust storm experiment.

5.2.3 Temperature and tides

Figure 5.7 shows the zonal-mean temperature at the beginning of global dust storm. The temperature is consistent with the observation as excepting for the polar region where it is assumed that the dust more than the observation is transported to the polar region.

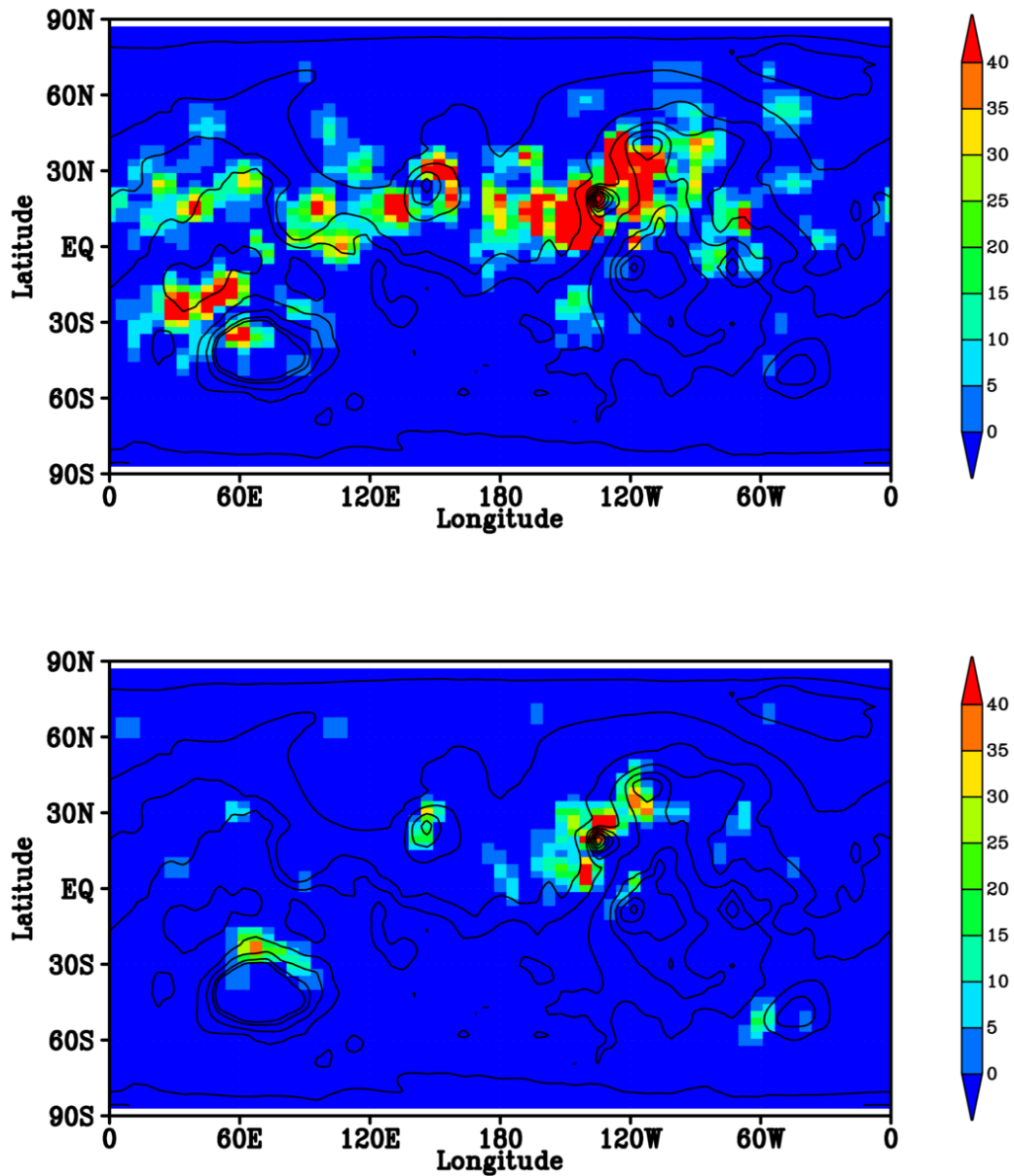


Figure 5.4: Top: Latitude-longitude distribution of simulated upward surface dust flux [$\mu\text{g cm}^{-2} \text{Sol}^{-1}$] using the near-surface wind stress scheme at 393 Sol ($L_S = 192.2^\circ$). In the top panel, the near-surface wind stress scheme was combined with the dust devil scheme, and additional surface dust flux was applied around the Hellas basin. The solid lines indicate the topography. Bottom: Same as Top but showing the results of the regional dust storm experiment.

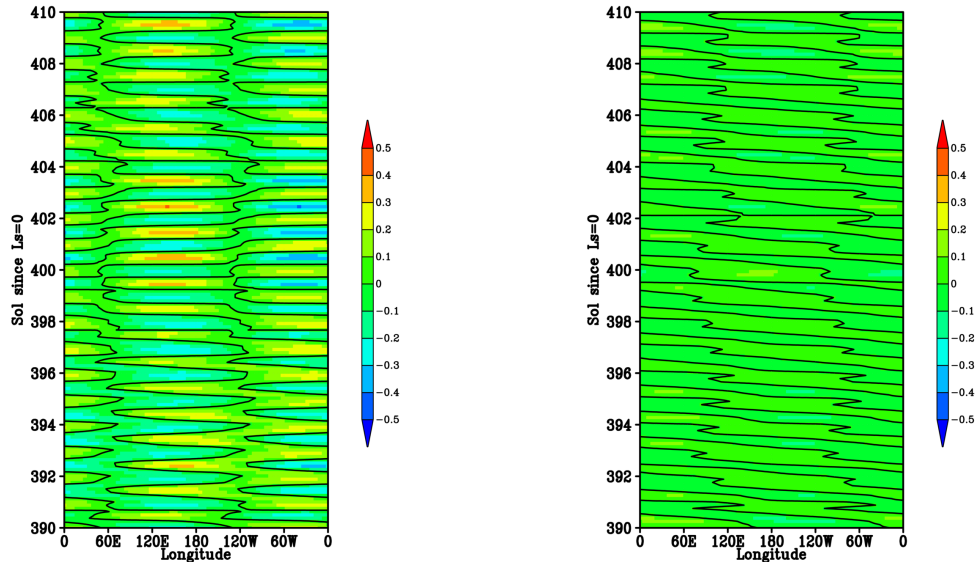


Figure 5.5: Left: Time series of WN1 surface pressure [hPa] (shaded) at 30°N. The solid lines indicate zero pressure. Right: Same as Left but regional dust storm experiment.

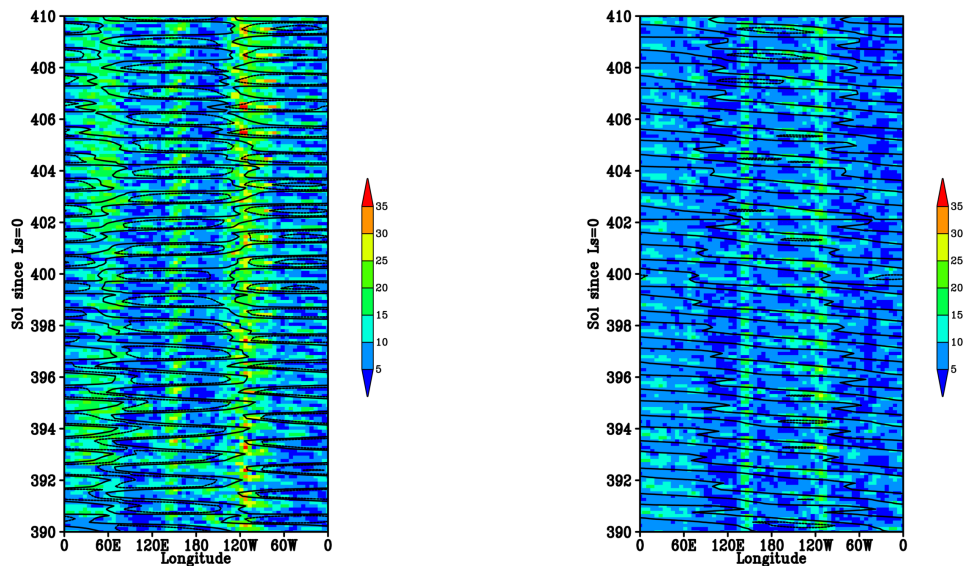


Figure 5.6: Left: Time series of surface wind [m s^{-1}] (shaded) and WN1 surface pressure [hPa] (contours) at 30°N. The solid and dotted lines indicate zero and ~ 0.3 pressure, respectively. Right: Same as Left but regional dust storm experiment.

The temperature between 60°S and 45°N increased from the lower atmosphere when the strong dust lifting started. This temporal development of temperature is close to the observation in MY25. Figure 5.8 shows the amplitude of the diurnal tide. The amplitudes are enhanced around 30°N and 40°S, where they reach up to 14 K. These latitudes are those of the Hellas basin, and dust lifting is much more active in mountainous areas than in other regions. The phase of the diurnal tide is shown in Figure 5.9. In regions of large amplitude, the phase remains constant below 1 hPa. The dust heating rate reaches 60 K Sol⁻¹ at 3 hPa. This heating rate is more than eight times as large as the best-fit regional dust storm experiment. The heating rate at surface is 20 K Sol⁻¹. The surface pressure amplitude is enhanced by the excited dust-heated tides; therefore, the near-surface wind is accelerated.

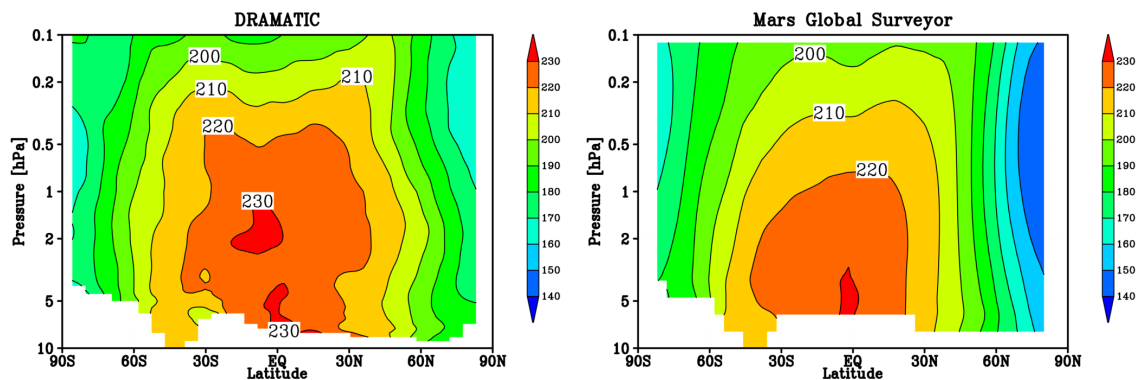


Figure 5.7: Left: Zonal-mean temperature [K] for simulation at $L_S = 192.2^\circ$. Right: TES-derived from MY25 at $L_S = 194.0^\circ$.

5.3 Response of additional surface dust flux for global dust storm

The realistic seasonal variations of dust opacity in the Martian atmosphere was obtained by using the couple of scheme, however it was difficult to simulate the encircling scale storm. In order to evaluate the interaction during global dust storm, the additional surface dust flux was adopted. We discuss how the parameters of flux function affect to the dust opacity. The given flux is function of the season, location, intensity F_{fcg0} and duration. The season and location were estimated by the observation; global dust storm 2001. Besides, the function also requires the parameters F_{fcg0} . In order to evaluate the impact for dust opacity, the sensitivity experiments were conducted. In case of the parameter F_{fcg0} is too small, high dust opacity did not expand globally, because the gravitational sedimentation for dust particle was larger than the lifting. This means that there was no positive feedback for the dust lifting. In contrast, if the extremely large value is given as F_{fcg0} , the global dust storm was reproduced in the model, however reasonable results have never simulated. One of the reasons is that the experiments suspended computationally. Furthermore, the dust opacity 5 ~ 10 times as large as observation is not credible. The other one is that the atmospheric stability increased suddenly by the very strong heating. The stable atmosphere makes the surface drag velocity small (see formula 2.2). These results show that the extremely small or large parameter F_{fcg0} is inappropriate for the global dust storm simulation by our MGCM. On the other hand, it is possible that if the appropriate parameter F_{fcg0} is set, the positive feedback may contributes to the generation of global dust storm. In case of our regional dust storm study, the polar caps prevented from the growth of feedback. In contrast, it is known that a global dust storm usually occurs in the lower and middle latitude where the ground is not covered with CO₂ ice (excepting for the top of high mountain). For the reason, it is suggested that the strong feedback can maintain some successive and strong lifting which produces a planetary scale dust storm.

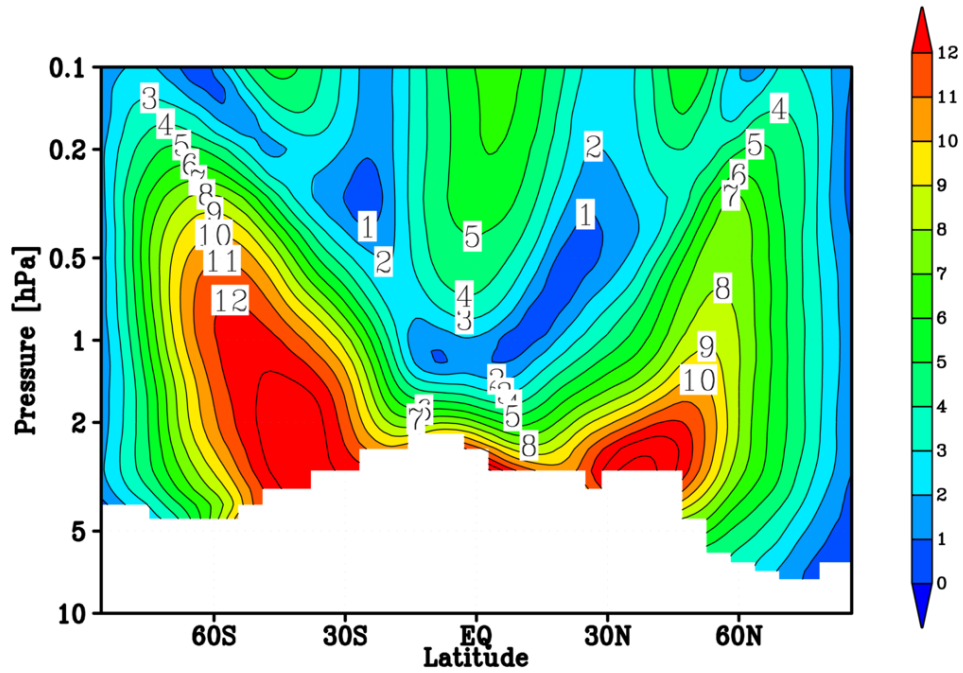


Figure 5.8: Height-latitude sections of diurnal tide amplitude [K]. The amplitude is calculated from temperatures recorded between 390 Sol and 410 Sol ($L_S = 190.4^\circ \sim 202.6^\circ$).

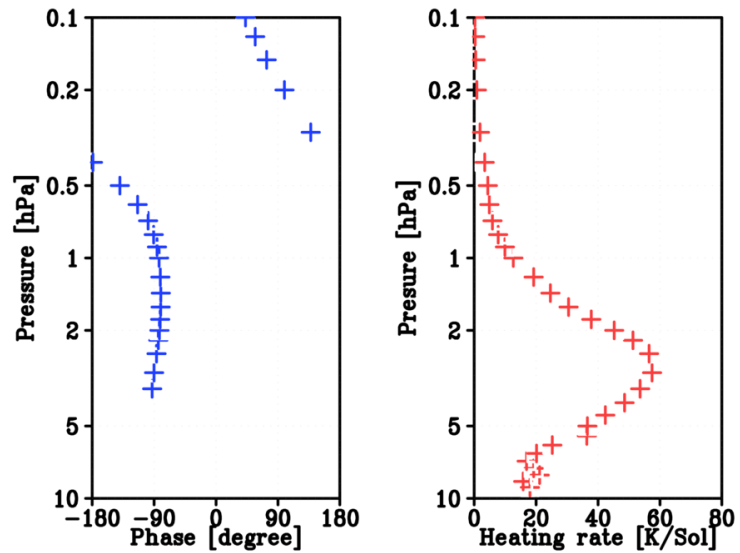


Figure 5.9: Left: Phase of diurnal tide at latitude 30°N . The phase angle is calculated from the temperatures recorded during the period of Figure 1.6. Right: Heating rate [K Sol^{-1}] over the same period.

5.4 Requirements for replicating global dust storms

Figure 5.10 shows the time series of daily maximum surface wind stress. The seasonal pattern of surface wind stress is consistent from year to year. However, strong surface wind stresses (exceeding 0.050 Pa) were simulated in the 2nd, 3rd, 4th, and 6th year. Although these high surface wind stresses may potentially trigger global dust storms, they did not in our study, because such effective lifting instantaneously triggers a global dust storm in observations. As mentioned in Chapter 3, when dust particles exist in the atmosphere, the tide caused by the airborne dust and solar radiation accelerates the surface wind. If the tides are to maintain such strong surface winds, dust must be retained in the atmosphere. Since atmospheric dust is removed by gravitational sedimentation, the altitude of dust injection is considered an important initial condition for global dust storm formation. In this study, the top altitude of dust supply was evaluated in the PBL, which is a function of the static stability (see Chapter 2.3.3). According to the PBL scheme, the model accurately simulates some regional dust events, then the altitude of PBL reaches to approximately 8 km. In contrast, to simulate global dust storms, we must reconsider the conditions under which the top altitude is defined. Because the altitude of additional upward dust injection is at most 21 km. This value is much higher than that of the PBL scheme. Similarly, the surface conditions are probably important for dust lifting. The surface wind stress is a function of the surface roughness height. Although the roughness map is given, the values are temporally fixed in our study. However, recent observations have shown that the Martian surface roughness height and albedo change annually [Szwast *at al.*, 2006]. By incorporating such temporal developments of the surface conditions in our model, we may be able to simulate the strong surface winds required for global dust storms.

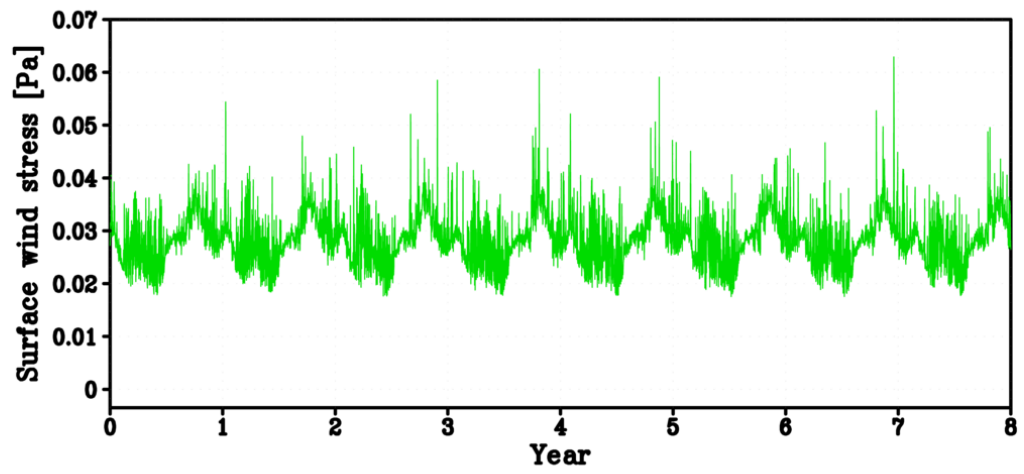


Figure 5.10: Time series of daily and global maximum for surface wind stress [Pa].

Chapter 6

Conclusions and future perspectives

This study aims to clarify the triggering environment and temporal development of dust storms in the Martian atmosphere. Idealized numerical experiments and previous observations suggest that near-surface winds are sufficiently accelerated by thermal tides to uplift dust from the ground. The thermal tides are maintained by heating atmospheric dust. To quantitatively evaluate the interaction among the dust injection, wave excitation, near-surface winds, and radiative effects of dust, a general circulation model (GCM) named DRAMATIC was developed. In this GCM, dust supply from the ground was explicitly forecast by two dust lifting schemes. The first scheme assumes that dust is lifted by near-surface wind stresses; the second whirls dust into the air by convective motions called dust devils. Both GCM lifting schemes were formulated by *Newman et al.* [2002a], and the details were improved as the GCM was developed. After determining suitable parameter values in plural sensitivity experiments, the thermal structure of the atmosphere, seasonal variation of dust opacity, and the occurrence of regional dust storms were well simulated, and consistent with observational results. In the northern hemisphere, dust lifting was strengthened between the equator and mid latitude, along the edges of the CO₂ ice cap. In the southern hemisphere summer, dust activity was heightened at 30°S. Here we focused on the mountainous area at 50° N, extending from 60°W to 120°W, which is a

major source of atmospheric dust. In this region, dust is lifted by winds forced along the northward mountain slopes.

The seasonal dust lifting in the northern hemisphere winter becomes clear. Strong lifting began around 430 Sol, starting at $L_S = 215.1^\circ$ and the surface winds exceeded 18 m s^{-1} . Following the period of dust lifting (which lasted for 50 Sols), the dust lifting and surface wind velocity suddenly dropped at around 480 Sol ($L_S = 247.3^\circ$), but increased again at around 540 Sol ($L_S = 286.0^\circ$). To evaluate the tidal contribution to the wind variation, a period covering less than 1 Sol was extracted from the near-surface wind. The thermal tide reached up to 11 m s^{-1} , and its temporal progression was synchronized with variations in the near-surface wind. The Martian atmosphere appears to be characterized by strong diurnal and semi-diurnal tides. Comparing the diurnal tide, semi-diurnal tide and atmospheric heating, a strong relationship was identified between the diurnal tidal activity and dust heating in the atmosphere. Between 480 Sol and 540 Sol ($L_S = 247.3^\circ \sim 286.0^\circ$), the surface wind was reduced by CO_2 ice forming on the ground. In our model, dust could not be lifted from this frozen surface. Floating atmospheric dust is removed by gravitational sedimentation, weakening tidal activity, and consequently reducing the near-surface wind velocity. This negative feedback is likely responsible for temporary reduction of dust lifting. Once the polar cap has receded, the dust is uplifted again, and the near-surface wind velocity is increased by the thermal tides driven by airborne dust.

The environments conducive to dust lifting were evaluated by driving an upward surface dust flux around the northern Hellas basin. The additional dust supply strengthened the dust lifting. Lifting was observed near the Hellas basin and the mountainous area centered on 30°N and 120°W , where the near-surface winds reached 35 m s^{-1} . The near-surface wind was strong at the trough of the WN1 surface pressure. In the global dust storm experiment, the amplitude of the WN1 surface pressure was enhanced to 0.3 hPa, three times larger than in the regional dust storm experiment. The sensitivity experiments also revealed the importance of ground topography for near-surface winds. Sufficiently

strong dust lifting to trigger planetary-scale dust storms occurred where the slope and the trough overlapped. The diurnal tidal amplitude was large in regions of strong dust uplift (around 30°N and 40°S). At 30°N, the tidal amplitude below 1 hPa was 15 K, and the dust heating rate reached 60 K Sol⁻¹. These results indicate that tides are maintained by heating dust in the Martian atmosphere. Consequently, the wind is accelerated at latitudes where dust heating maintains strong tidal activity. As the near-surface wind is accelerated on sloped regions, it becomes sufficiently strong to project massive quantities of dust into the atmosphere. Therefore, we can suggest that when dust lifting is strengthened in a certain region, plural dust lifting can immediately occur in another region.

This study has revealed the probable mechanism and the environmental conditions of dust storms in the Martian atmosphere. However, several problems remain. Our Mars general circulation model simulated the observed seasonal variation in dust opacity, but could not reproduce the annual variation which includes global dust storms. At present, no numerical model of dust cycling in the Martian atmosphere can capture this yearly variability, because the near-surface atmosphere during a dust injection event is not understood sufficiently. In chapter 5, the global dust storm is simulated by using the additional surface dust flux. In comparison with the dust injection altitude, global dust storm reached up to 21 km. On the other hand, the regional one is about 8 km. The differences between two altitudes may affect to the scale of dust storm. The surface parameters are extremely important in dust storm simulations. In developing our Mars general circulation model, the topography, roughness height, thermal inertia and surface albedo are implemented as surface boundary conditions, but are assumed temporally fixed (except for the surface albedo). Observations have indicated that both the albedo and roughness height change over time [Szwast *et al.*, 2006]. Time-varying surface parameters would affect the near-surface wind stress and the intensity of convective motions such as dust devils. Rendering these parameters dynamic rather than fixed would alter the dust lifting schemes implemented in the model. This development might be necessary to simulate

simultaneous regional and global dust storms, as observed in actual Martian dust cycling. Such developments will be considered in future work.

Reference

- [1] Basu. S., M. I. Richardson and Wilson, R. J, Simulation on the Martian dust cycle with the GFDL Mars GCM, *J. Geophys. Res.*, **109**, E11, 2004
- [2] Basu, S., J. Wilson, M. Richardson, and A. Ingersoll, Simulation of spontaneous and variable global dust storms with the GFDL Mars GCM, *J. Geophys. Res.*, **111**, 2006.
- [3] Banfield, D., B. Conrath, J. C. Pearl, M. D. Smith, and P. Christensen, Thermal tides and stationary waves on Mars as revealed by Mars Global Surveyor thermal emission spectrometer, *J. Geophys. Res.*, **105**, 9521-9537, 2000.
- [4] Banfield, D., et al. (2003), Forced waves in the Martian atmosphere from MGS TES nadir data, *Icarus.*, **161**, 319-345.
- [5] Cantor, B. A., M. J. Wolff, P. B. James, and E. Higgs, Recession of the Martian north polar cap: 1990-1997 Hubble Space Telescope observations, *Icarus*, **136**, 175-191, 1998.
- [6] Cantor, B. A., P. B. James, M. Caplinger, and M. J. Wolff, Martian dust storms: 1999 Mars Orbiter Camera observations, *J. Geophys. Res.*, **106**, 23,653-23,687, 2001.
- [7] Cantor, B. A., M. Malin, and K. S. Edgett (2002), Multiyear Mars Orbiter Camera

- (MOC) observations of repeated Martian weather phenomena during the northern summer season, *J. Geophys. Res.*, **107**, 5014,
- [8] Cantor, B. A., K. M. Kanak, and K. S. Edgett (2006), Mars Orbiter Camera observations of Martian dust devils and their tracks (September 1997 to January 2006) and evaluation of theoretical vortex models, *J. Geophys. Res.*, **111**, 2002.
- [9] Conrath, B. J., J. C. Pearl, M. D. Smith, W. C. Maguire, P. R. Christensen, S. Dason and M. S. Kaelberer, Mars Global Surveyor Thermal Emission Spectrometer (TES) observations: Atmospheric temperatures during aerobraking and science phasing, *J. Geophys. Res.*, **105**, E4, 9509-9519, 2000.
- [10] Christensen, P. R., D. L. Anderson, S. C. Chase, R. T. Clancy, R. N. Clark, J. Conrath, H. H. Kieffer, R. O. Kuzmin, M. C. Malin, J. C. Pearl, T. L. Roush and M. D. Smith, Results from the Mars Global Surveyor Thermal Emission Spectrometer, *Science*, **279**, 1692-1697, 1998.
- [11] Clancy, R. T., M. J. Wolff, and P. R. Christensen (2003), Mars aerosol studies with the MGS TES emission phase function observations: Optical depths, particle sizes, and ice cloud types versus latitude and solar longitude, *J. Geophys. Res.*, **108**, 2003.
- [12] Fenton, L. K., J. C. Pearl and T. Z. Martin, Mapping Mariner 9 Dust Opacities, *Icarus*, **130.**, 115-124, 1997.
- [13] Fisher, J. A., M. I. Richardson, C. E. Newman, M. A. Szwast, C. Graf, S. Basu, S. P. Ewald, A. D. Toigo, and R. J. Wilson, A survey of Martian dust devil activity using Mars Global Surveyor Mars Orbiter Camera images, *J. Geophys. Res.*, **110**, 2005.
- [14] Forbes, J. M., A. F. C. Bridger, S. W. Bougher, M. E. Hagan, J. L. Hollingsworth, G. M. Keating, and J. Murphy, Nonmigrating tides in the thermosphere of Mars, *J. Geophys. Res.*, **107**, 5113, 2002.

- [15] Forget. Francois., F, Hourdin, R.Fournier, C.Hourdin and O. Talagrand, CO₂ Snow-fall on Mars: Simulation with a General Circulation Model, *Icarus.*, **131**, 202-316, 1998.
- [16] Forget. Francois., F, Hourdin, R, Fournier, C. Hourdin, O. Talagrand, M. Collins, S, R. Lewis, P, L. Read and J, P. Huot, Improved general circulation models of the Martian atmosphere from the surface to above 80km, *J. Geophys. Res.*, **104**, 24,155-24,175, 1999.
- [17] Forget. Francois., Yann, Wanherdrick and S, R. Lewis, 2001: Validation of the Mars General Circulation Model and Climate Database with new spacecraft observations, *European Space Agency Technical Report*, 22p.
- [18] Greeley. R, J, D. Iverson, Wins as a geological process on Earth, Mars, Venus and Titan, CAMBRIDGE UNIVERSITY PRESS.
- [19] Greeley, R., N. Lancaster, S. Lee, and P. Thomas, Martian aeolian processes, sediments, and features, in Mars, edited by H. H. Kieffer et al., chap. 22, pp. 730-766, Univ. of Ariz. Press, Tucson, 1992.
- [20] Greeley. R., M, R. Balme, J, D. Iversen, S. Metzger, R. Mickelson, J, Phoreman and B. White, Martian dust devils: Laboratory simulations of particle threshold, *J. Geophys. Res.*, **108**, 5041-5051, 2003.
- [21] 橋本尚久. 火星 GCM を用いた極冠形成シミュレーション 東京大学大学院理学系研究科地球惑星科学専攻 平成 13 年度修士論文.
- [22] Robert M. Haberle, Manoj M. Joshi, James R. Murphy, Jeffrey R. Barnes, John T. Schofield Greg Wilson, Miguel Lopez-Valverde, Jeffery L. Hollingsworth, Alison F. C. Bridger, and James Schaeffe, General circulation model simulations of the Mars Pathfinder atmospheric structure investigation/meteorology data, *J. Geophys. Res.*, **104**, 8957-8974, 1999.

- [23] Heavens, N. G., J. L. Benson, D. M. Kass, A. Kleinbohl, W. A. Abdou, D. J. McCleese, M. I. Richardson, J. T. Schofield, J. H. Shirley, and P. M. Wolkenberg, Water ice clouds over the Martian tropics during northern summer, *Geophys. Res. Lett.*, **37**, 2010.
- [24] D.P. Hinson, M. Patzold, S. Tellmann, B. Hausler and G.L. Tyler, The depth of the convective boundary layer on Mars, *Icarus.*, **198**, 57-66, 2008.
- [25] Hollingsworth, J. L., R. M. Haberle, J. R. Barnes, Alison, F. C. Bridger, J. B. Polack, H. Lee and J. Schaeffer, *Nature.*, **380**, 413-416, 1996.
- [26] James. P. B., J. L. Hollingsworth, M. J. Wolff and S. W. Lee, North Polar Dust Storm in Early Spring on Mars: *Icarus.*, **138**, 64-73, 1999.
- [27] Kahre, M. A., J. R. Murphy, R. M. Haberle, F. Montmessin, and J. Schaeffer, Simulating the Martian dust cycle with a finite surface dust reservoir, *Geophys. Res. Lett.*, **32**, 2005.
- [28] Kahre, M. A., J. R. Murphy, and R. M. Haberle, Modeling the Martian dust cycle and surface dust reservoirs with the NASA Ames general circulation model, *J. Geophys. Res.*, **111**, 2006.
- [29] Kahre, M. A., J. L. Hollingsworth, R. M. Haberle, and J. R. Murphy, Investigations of the variability of dust particle sizes in the Martian atmosphere using the NASA Ames General Circulation Model, *Icarus*, **195**, 576-597, 2008.
- [30] Kasten. F, Falling speed of aerosol particles, *J. Appl. Meterol.*, **7**, 944-947, 1968.
- [31] 黒田剛史. CCSR/NIES AGCM を用いた火星大気シミュレーション, 東京大学大学院理学系研究科地球惑星科学専攻 平成 12 年度修士論文.
- [32] Kuroda, T., N. Hashimoto, D. Sakai and M. Takahashi, Simulation of the Martian Atmosphere Using a CCSR/NIES AGCM, *J. Meteor. Soc.*, **83**, 1-19, 2005.

- [33] Leovy. C, B., R, W. Zurek and J, B. Pollack, Mechanisms for Mars Dust Storms, *J. Atmos. Sci.*, **30**, 749-762, 1973.
- [34] Lorenz. R, D., J. I. Lunine, J. A. Grier, and M. A. Fisher. Prediction of aeolian features on planets: Application to Titan paleoclimatology, *J. Geophys. Res.*, **100**, 26,377-26,386, 2000.
- [35] Magalhaes, A. J., R, E. Young, Downslope Windstorms in the Lee of Ridges on Mars, *Icarus.*, **113**, 277-294, 1995.
- [36] Navarro, T, Madeleine, J,-B, , F. Forget, A. Spiga, E. Millour, F. Montmessin, and A. Maattanen, Global climate modeling of the Martian water cycle with improved microphysics and radiatively active water ice clouds, *J. Geophys. Res.*, **119**, E7, 1479-1495, 2014.
- [37] McCleese, D. J., J. T. Schofield, F. W. Taylor, S. B. Calcutt, M. C. Foote, D. M. Kass, C. B. Leovy, D. A. Paige, P. L. Read, and R. W. Zurek, Mars Climate Sounder: An investigation of thermal and water vapor structure, dust and condensate distributions in the atmosphere, and energy balance of the polar regions, *J. Geophys. Res.*, **112**, 2007.
- [38] Moriyama, S, The Dynamical Effects of Real Mars Orography upon the Large-Scale Air Flow and Some Meteorological Phenomena of Mars, *J. Meteor. Soc.*, **51**, 73-84, 1973.
- [39] Newman. C, E., S, R. Lewis, P, L. Read and F. Forget, Modeling the martian dust cycle 1.Representations of dust transport processes, *J. Geophys. Res.*, **107**, E12, 5123-5140, 2002a.
- [40] Newman. C, E., S, R. Lewis, P, L. Read and F. Forget, Modeling the martian dust cycle 2.Multiannual radiatively active dust transport simulations, *J. Geophys. Res.*, **107**, E12, 5124-5138, 2002b.

- [41] Renno. N, O., A, A. Nash, J, Lunine and J, Murphy, Martian and terrestrial dust devils: Test of a scaling theory using Pathfinder data, *J. Geophys. Res.*, **105**, 1859-1865, 2000.
- [42] Renno. N, O., A, P. Ingersoll, Natural Convection as a Heat Engine: A Theory for CAPE, *J. Atmos. Sci.*, **53**, 1996.
- [43] Renno. N, O., M, L. Burkett and M, P. Larkin, A simple Thermodynamical Theory for Dust Devils, *J. Atmos. Sci.*, **55**, 3224-3252, 1998.
- [44] 酒井大輔. GCM を用いた火星ダスト, ドライアイス雲, 水収支過程に関する研究, 東京大学大学院理学系研究科地球惑星科学専攻 平成 15 年度修士論文.
- [45] Seiff. A., POST-VIKING MODELS OF THE STRUCTURE OF THE SUMMER ATMOSPHERE OF MARS, *Adv. Space. Res.*, **2**, 3-17, 1982.
- [46] Seguro. J, V., T, W. Lambert, Modern estimation of the parameters of the Weibull wind speed distribution for wind energy analysis, *J. Wind. Eng. Indust. Aerodyn.*, **85**, 75-84, 2000.
- [47] Siili. T., R, M. Haberle and J. R, Murphy, SENSITIVITY OF MARTIAN SOUTHERN POLAR CAP EDGE WINDS AND AURFACE STRESSES TO THE LARGE-SCALE SUBLIMATION FLOW, *Adv. Space. Res.*, **19**, 1241-1244, 1997.
- [48] Siili. T., R, M. Haberle, J. R, Murphy and H. Savijarvi, Modelling of the combine late-winter ice cap edge and slope winds in Mars' Hellas and Argyre regions, *Plan. Spac. Sci.*, **47**, 951-970, 1999.
- [49] Smith, D. E., et al. (1999), The global topography of Mars and implications for surface evolution, *Science*, **284**, 1495-1503.
- [50] Smith, D. E., M, T. Zuber and G, A. Neumann, Seasonal Variations of Snow Depth on Mars, *Science.*, **294**, 2001.

- [51] Smith, M. D., B, J. Conrath, J, C. pearl and P, R. Christensen, Thermal Emission Spectrometer Observations of Martian Planet-Encircling Dust Storm 2001A, *Icarus.*, **157**, 259-263, 2002.
- [52] Smith, M. D., B, J. Conrath, J, C. pearl and P, R. Christensen, Thermal Emission Spectrometer results: Mars atmospheric thermal structure and aerosol distribution, *J. Geophys. Res.*, **106.**, 23,929-23,945, 2001.
- [53] Smith, M. D., Interannual variability in TES atmospheric observations of Mars during 1999-2003, *Icarus*, **167**, 148-165, 2004.
- [54] Smith, M.D., J.C. Pearl, B.J. Conrath, and P.R. Christensen (2000). Mars Global Surveyor Thermal Emission Spectrometer (TES) observations of dust opacity during aerobraking and science phasing, *J. Geophys. Res.*, 105, 9539-9572.
- [55] Strausberg, M. J., H. Wang, M, I. Richardson, S, P. Ewald and A, D. toigo, Observations of the initiation and evolution of the 2001 mars global duststorm, *J. Geophys. Res.*, **110**, 2005.
- [56] Szwast, M. A., M, I. Richardson and A, R. Vasavada, Surface dust redistribution on Mars as observed by the Mars Global Surveyor and Viking orbiters, *J. Geophys. Res.*, **111**, 2006.
- [57] 田中亮. Dust Devil の発生環境と構造に関する数値的研究, 東京大学大学院理学系研究科地球惑星科学専攻 平成 16 年度修士論文.
- [58] Toigo, A. D., M, I. Richardson, S, P. Ewald and P, J. Gierasch, Numerical simulation of Martian dust devils, *J. Geophys. Res.*, **108**, E6, 5047-5060, 2003.
- [59] Toigo, A. D., M, I. Richardson, R. J. Wilson, H. W and A, P. Ingersoll, A first lool at dust lifting and dust storms near the south pole of Mars with a mesoscale model, *J. Geophys. Res.*, **107**, E7, 2002.

- [60] Wang. H., M. I. Richardson, R. J. Wilson, A. P. Ingersoll, A. D. Toigo and R. W. Zurek, Cyclons, tides and the origin of a cross-equatorial dust storm on Mars, *Geophys. Res. Lett.*, **30**, 1488-1491, 2003.
- [61] Wilson, R. J., Evidence for nonmigrating thermal tides in the Mars upper atmosphere from the Mars Global Surveyor Accelerometer Experiment, *Geophys. Res. Lett.*, **29**, 1120, 2002.
- [62] White. B, R., Soil Transport by Winds on Mars, *J. Geophys. Res.*, **84**, 4643-4651, 1979.
- [63] Zurek. R, W., Conway B. Leovy, Thermal tides and Martian dust storms: Direct evidence for coupling, *J. Geophys. Res.*, **84**, B6, 1979.
- [64] Zurek. R, W., Martian Great Dust Storm: An Update, *Icarus.*, **50**, 288-311, 1982.
- [65] Zurek. R, W., Interannual variability of planet-encircling dust storms on Mars, *J. Geophys. Res.*, **98**, 3247-3259, 1993.

Acknowledgments

This doctoral study was done under the supervision of Prof. Masaaki Takahashi (Atmosphere and Ocean Research, AORI) since April 2004. He always gave me good suggestions for my research. I would like to thank to his passionate guidances.

I appreciate examiners, Prof Takeshi Imamura (Institute of Space and Astronautical Science / Japan Aerospace Exploration Agency, ISAS/JAXA), Prof. Yoshihisa Matsuda (Tokyo Gakugei University), Prof. Keita Iga (Atmosphere and Ocean Research, AORI) and Prof. Yasuko Kasai (National Institute of Information and Communications Technology, NICT, Tokyo Institute of Technology). They gave me many advices for my thesis.

Dr. Takeshi Kuroda (Tohoku University) advised me how to develop a numerical model and discussed about my work deeply in many times. I also would like to thank to all members of Takahashi Lab. Dr. Paul Hartogh (Max Planck Institute for Solar System Research) gave me nice opportunity to study at Max Planck Institute (MPS) in Germany for two years. On staying at Max Planck Institute, Dr. Alexander S. Medvedev gave many advices to develop the numerical model and had many discussions. Dr. Hideo Sagawa (National Institute of Information and Communications Technology, NICT) and Dr. Manabu Yamada (Institute of Space and Astronautical Science / Japan Aerospace Exploration Agency, ISAS/JAXA) also discussed in Max Planck Institute. Dr. Hideharu Akiyoshi (National Institute for Environmental Studies) employed me in his laboratory since May 2011.